University of Nottingham
UK | CHINA | MALAYSIA

Anisotropic Thermal Conductive Composite Constructed by Carbon Fiber for Thermal Management in Electronic Package

Maohua Li

Thesis submitted to University of Nottingham for the degree of Doctor of Philosophy

10 August 2022

Contents

This page is intentionally blank

Acknowledgement

I want to thank my supervisors, Jim C. Greer, Nan Jiang, Hainam Do and Jinhong Yu, for their guidance, support and patience throughout my PhD. I will never forget the happy talks with Prof. Jim, Prof. Hainam and Prof. Nan, all of whom are outstanding scientists and supervisors. It is my honor to study with them. When they talk about quantum physics, molecular simulation or engineering, their inspiriting expression seems like they are talking about their family. Their love for science and technology cannot be pretended. I always respect them from my heart.

I want to thank Prof. Jinhong especially. I am not a hardworking student. he urged me to read more research papers, from which I learned a lot. I really appreciate it from the inside. whenever I discussed my new idea with him, he would encourage me to have a try and I could feel his happiness when I showed him the test result proving the idea. He teaches me how to organize a research paper and research. Thank you!

I would thank my friends. When I came to CNITECH first time, it was Yapeng Chen and Xiao Hou who introduced the laboratory to me and taught me the operation of instruments. We studied together and hung around. Guichen Song, Linhong Li, Yunxiang Lu and all my friends, whom I cannot list their names one by one, helped me a lot when I faced the setback in research. With them, I have precious memories.

I want to thank my girlfriend, Xueying Liu. We met during the outbreak of COVID-19 when my study did not go well. I dare not imagine the circumstance without her. She is an English teacher, so I always

consulted her when I got confused about grammar. Some of my manuscripts were finished with her help. Xueying, hope you know how much I love you.

I would thank my family for their support in my PhD. During the four years, a lot of things happened in my family. They shouldered it by themselves and never told me in case disturbing my schedule. Every time we talked, my mom asked about the progress of my research, although it was difficult for her to figure out what I told her. Hope you are all healthy and happy.

In the end, I want to appreciate UNNC and CNITECH. It is the cooperation program that gave me the opportunity to study and realize my thought here. It is a precious and happy memory for me.

This page is intentionally blank

Abstract

Because of the high-power density of chips, thermal management material has become a key node of electronic system development. Thermal management material with high thermal conductivity can dissipate the waste heat on time to avoid heat damage to system stability and arithmetic speed. However, polymer as traditional packaging material used in electronic system by virtue of low processing temperature and good mechanical properties can hardly satisfy the demand for high thermal conductivity. So, scientist tend to endow the polymers with high thermal conductivity by mixing them with fillers which can enhance the heat transport.

However, how to construct such composites which possess high thermal conductivity and meanwhile can satisfy the requirement of a specific application is still a challenge facing engineers and scientists.

In the rest of this thesis, carbon fiber, a thermal conductive filler with anisotropic thermal conductivity, was applied to construct a thermal conductive composite with the assistance of a mechanical force field. To make full use of the anisotropic thermal conductivity of carbon fiber to obtain directional high thermal conductivity composites, carbon fiber was supposed to be aligned along a specific direction. By compressing the carbon fiber powder, an orientated thermal conductive network was fabricated to transport heat efficiently, which resulted in a 32 $W\ m^{-1}\ K^{-1}$ thermal conductivity.

Compared with compressing, stretching is a more efficient method to

achieve the alignment of carbon fiber in a single direction. However, the difficulty of applying the tensile force on carbon fiber powder blocked the realization of the strategy. Here, a novel strategy was proposed. A medium was introduced to control the movement of carbon fiber powder by transferring the mechanical force applied on it to the carbon fiber. Then the medium was graphitized into sheets of carbon crystal enhancing the heat exchange between carbon fibers. The thermal transport speed in different carbon structure and the alignment of carbon fiber during the stressing process were calculated with molecular dynamics and mathematics. As a result, with the novel strategy, metal-level thermal conductive but lighter composite was constructed.

Besides thermal conductivity, in this thesis, a thermal management material with phase change function was constructed using phase change matrix which can suppress temperature fluctuation during the overloading of electronic equipment. The extra heat generated by the overloading would be stored as latent heat of matrix during the phase change process avoiding the rise of equipment temperature. As a result, the hurt of high temperature to equipment can be avoided. The resulted material has a 23 W m^{-1} K^{-1} thermal conductivity accompanied with 62 J g^{-1} K^{-1} latent heat.

In summary, different mechanical methods manufacturing directional thermal conductive materials were talked in the thesis. Accompanied with them, characterization of structure and thermal properties was done with experimental, simulative and mathematical methods. Various applications are given in the thesis to prove the materials' practicability. The materials manufactured with these methods were supposed to be

applied in different fields because of their promising properties. Meanwhile, it is possible for some different analysis methods used here to inspire the researchers and accelerate the development of the field.

List of Figures

List of Tables

List of Abbreviations

CF	Carbon Fiber
BN	Boron Nitride
PEG	Polyethylene Glycol
PAA	Polyacrylic Acid
BAC	N,N′-Methylenebis (Acrylamide)
ATCS	Active Thermal Control Systems
PTCS	Passive Thermal Control Systems
HEVs	Hybrid Electric Vehicles
IHS	Integrated Heat Sink
TIMs	Thermal Interface Materials
BGA	Ball Grid Array
PDOS	Phonon Density of States
BTE	Boltzmann Transport Equation
NEMD	Non-Equilibrium Molecular Simulation
EMD	Equilibrium Molecular Simulation
FDT	Fluctuation-Dissipation Theorem
LVMs	Localized Vibrational Modes
LCP	Liquid Crystal Polymers
LM	Liquid Metal
SiC	Silicon Carbide
IPCF	Isotropic Pitch-Based Carbon Fiber
MPCF	Mesophase Pitch-Based Carbon Fiber
NMR	Nuclear Magnetic Resonance
IR	Infrared Spectra
LFA	Laser Flash Apparatus
DSC	Differential Scanning Calorimetry
TRCMA	Thermal Resistance and Conductivity Measurement Apparatus
TGA,	Thermo Gravimetric Analysis
DMA	Thermal Dilatometer

SEM	Scanning Electron Microscope
micro-CT	Micro-Computed Tomography
XRD	X-Ray Diffraction
XPS	X-Ray Photoelectron Spectra
TCE	Thermal Conductivity Enhancement
CTE	Coefficient of Thermal Expansion
TDP	Thermal Distortion Parameter
PCM	Phase Change Material
RDG	Reduce Density Gradient
HDPE	High Density Polyethylene
ABS	Acrylonitrile Butadiene Styrene Copolymers
PC	Polycarbonate
PA	Polyamide
PP	polypropylene
PS	Polystyrene
PVC	Polyvinyl Chloride
TPI	Thermal Plastic Polyimide
PET	Polyethylene Terephthalate
PEEK	poly(ether-ether-ketone)
PI	Polyimide
PU	polyurethane
k	Thermal Conductivity
T	Temperature
Q	Heat flow
R	Thermal resistance
θ	Angle between 1D filler and a specific direction

This page is intentionally blank

Chapter 1. Introduction

1.1 Synopsis

This chapter will introduce the background of thermal management material to illustrate the significance of developing thermal conductive composites. Developed for decades, there are a lot of theories developed to analyze the heat transport in materials, including kinetatic theory and molecular dynamic methods. The basic theories will be introduced to understand what structure may possess good thermal transport property.

Then various strategies and the most important research to achieve high thermal conductivity experimentally will also be summarized, including the promotion of the intrinsic thermal conductivity of polymers and the manufacture of thermally conductive composites from fillers. Considering that the thesis will focus on the manufacture of thermal conductive composite, the property of general filler and processing method will be introduced in detail. In the end, the objectives and the outline of the thesis will be given briefly.

1.2 Background

Heat is a kind of energy with a long history. The substance of heat is the vibration of atoms. How to control heat transport has been a challenging generic problem facing humanity and raised a novel and attractive subject in the modern era: thermal management. Aerospace projects, electronic engineering, refrigeration, vehicle design, energy storage and

related subjects require the understanding and application of thermal management.

In aerospace projects, thermal management is applied to the construction of the housing for transmitter and receiver modules to protect them from the environment with wild fluctuation temperature, heat pipes for power system radiators and radiators for spacecraft. The challenges and opportunities for thermal management on aircraft and satellites have been previously discussed.[1-3] The temperature difference between the dayside and nightside of the satellite can easily display a range over 200 ^{o}C within our solar system. Research reveals that the deformations of solar arrays caused by thermal stress should be considered or it can lead to functional failure of the entire spacecraft system.[4-5] There are two design philosophies for thermal management systems, active thermal control systems (ATCS) and passive thermal control systems (PTCS). ATCS may be applied to a pumped loop system and heater to control the temperature of components within a designed temperature range. However, the limitation of power, mass and space is a challenge for ATCS. PTCS gives another low-weight and energy-efficient strategy by applying thermal management materials. Researchers also point out that with the increase of heat generated due to the increasing density of electronic equipment, more effective thermal management materials are required.[6]

In vehicle design, especially with the development of hybrid electric vehicles (HEVs), the influence of temperature on performance attracts significant attention and a cooling that system that takes into account fuel economy, cost and the limited packaging space into account is desired.

[7-9] Particularly, the high-voltage battery used as the power source in HEVs is a high-power density and long-life cycle device. According to research, the performance of the battery is highly dependent on its operating temperature. As a result, more effort is being focused on this field.[10-12]

Energy storage devices, particularly batteries, which are widely used in the grid, vehicle, communication and computer systems generate all generate significant heat during operation. Overheating may result in the acceleration of charge storage capacity degradation and thermal runaway. To avoid the damage from heat on devices, researchers devote effort to finding new solutions to overcome associated problems.[11, 13-15]

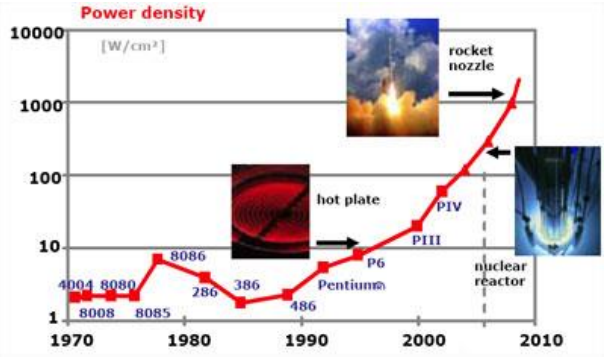

Figure 1.1. The power density of microchip processor in the past decades.

Another area where the importance of thermal management is recognized is the packaging of electronic elements, which are widely used in phones, telecommunication base stations, supercomputers and servers. Especially, the past years have witnessed the boost of fifth generation electronic communication technology where the miniaturization, and integration of high-power electronic elements is widely used. Heat accumulation leads to the significant degradation of device performance. There is an analysis reporting that approximately 55%

of electronic device failures are caused by high temperatures, and once the working temperature of the device increases by 10 ºC, its likelihood of failure will double. However, the power density of microchips has been growing at a high rate, as figure 1.1 shows. According to the data from Intel, the power densities of chips can be beyond that of the rocket nozzle, which reached a power density of 1000 W cm^{-2} before 2010. This huge amount of heat causes catastrophic damage to electron systems. To avoid the damage caused by high temperature, the dissipation of waste heat generated during the operation of an electronic component needs to be quickly removed. As described above, the major task of thermal management in electronic systems is to dissipate heat at a rate larger than its generation.

Of the three heat transport methods (heat convection, thermal conduction and thermal radiation), the first two are the most used strategies for thermal management in electronic devices. Heat convection is the basis for using forced heat transfer, including forced air cooling and water/air cooling. These cooling methods efficiently dissipate heat from a heat sink to an ambient environment. However, although forced heat transfer can partially mitigate the problem, the heat path from the chip to the heatsink cannot be bypassed. The structure of a general radiator is illustrated in figure 1.2. It can be noted that there are three critical parts when we construct the system, namely an integrated heat sink (IHS) and two thermal interface materials (TIMs).

The IHS packaging isolates the chip from the environment and is required to possess high intrinsic thermal conductivity. Simultaneously, applications demand that the mechanical property of an IHS needs to

match that of the chip and the heatsink, which are, in most cases, silicon and metal, respectively, to limit stresses at high temperatures. Much work has focused on explaining the importance and working principle of TIMs.[16-17] Between the chip, IHS and heatsink, interface mismatch shrinks the contact area, and much space between two surfaces is filled by air whose thermal conductivity is low. This causes the thermal contact resistance, TIM1 and TIM2 are used to fill the void and remove the air, as shown in Figure 1.3.

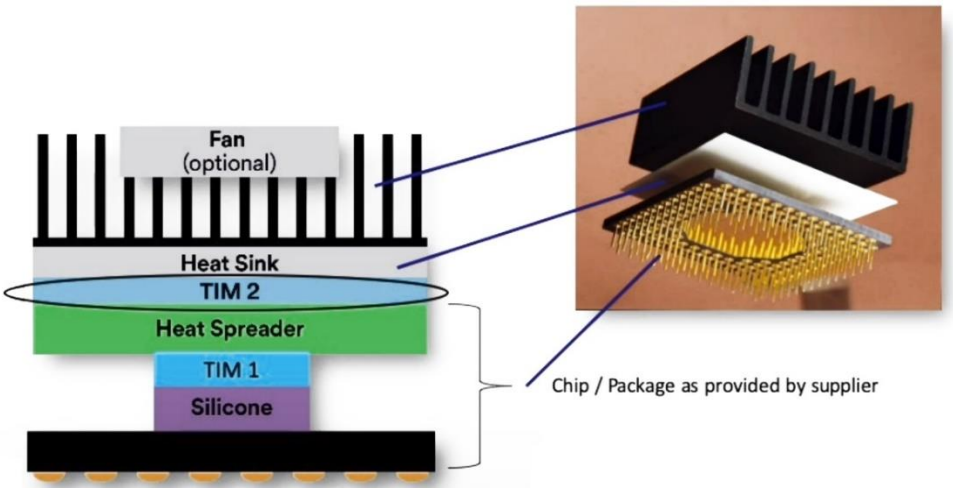

Figure 1.2. A typical ball grid array (BGA) electronics package with two TIMs. The heat is conducted through the backside of a BGA chip. There are TIMs between chip and IHS and between IHS and heatsink. The different TIM applications are called TIM1 and TIM2, respectively.

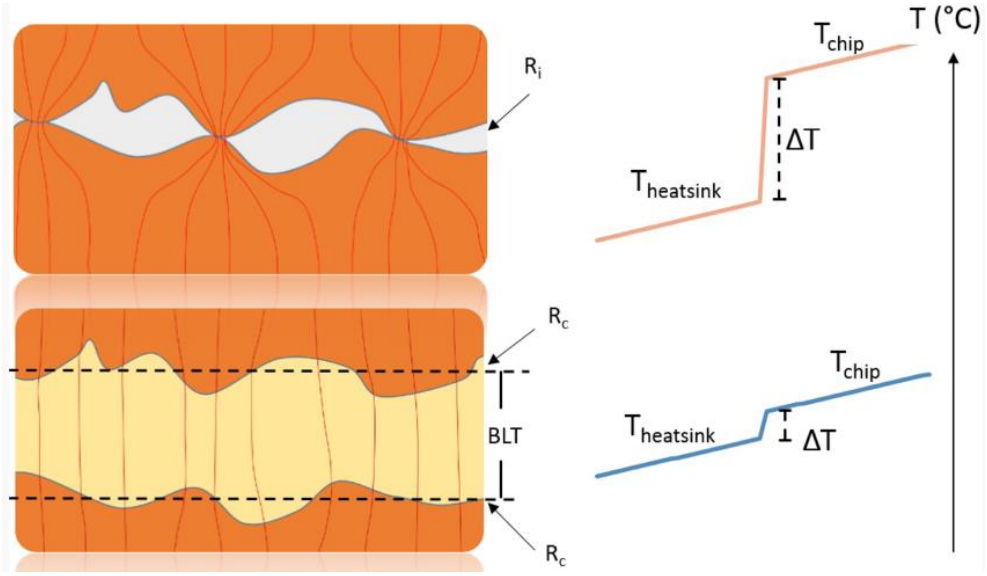

Figure 1.3. Schematic of the function of TIMs. The uneven of two surfaces causes the shrink of contact area and the infiltration of air. TIM fills out the voids and reduces the temperature drop over the interface.[16]

A thermal management materials' property can be evaluated by thermal conductivity or thermal resistance measurement. Thermal conductivity is defined through a nonequilibrium process. When heat flows through a unitary block, the thermal conductivity of the material is defined as

$$k = -\frac{\vec{Q}}{\vec{\nabla}T} \tag{1.1}$$

where $\vec{Q}$ is the heat flux (W m^{-2}) and $\vec{\nabla}T$ is the temperature gradient (K m^{-1}) in the direction of heat transport. This parameter is used to evaluate the ability of a material to propagate heat. Fourier's law expresses the process as

$$Q = -k\frac{dT}{dx} \tag{1.2}$$

where Q is the heat flux. Thermal resistance is defined as

$$R = -\frac{\vec{\nabla}T}{\vec{Q}} \tag{1.3}$$

Their relationship is in analogy with electrical conductivity and resistance. However, in the discussion of heat flow between interfaces, the thermal

resistance can be more efficient. The thermal resistance is introduced by the interface, including contact thermal resistance and interface thermal resistance. The former is caused by surface roughness, as already introduced in figure 1.3. The purpose of a TIM is to depress the influence of contact thermal resistance. However, even if the two surfaces are smooth at the atomic level, the mismatch of vibrational modes between two materials causes phonon scattering at the interface, resulting in an increase in surface thermal resistance compared to the ideal case. These considerations for electronic packaging and properties of thermal interface materials define the requirements for a high thermal conductivity to depress thermal resistance to allow for rapid heat dissipation.

1.3 The methods calculating thermal conductivity

To explain the thermal transport process, various theories have been used. They originate from different assumptions but agree with each other. They can be regarded as a different perspective on the same question. Simultaneously, they are important keys to explain the phenomenon of heat transport and related problems.

1.3.1 Classical kinetic theory

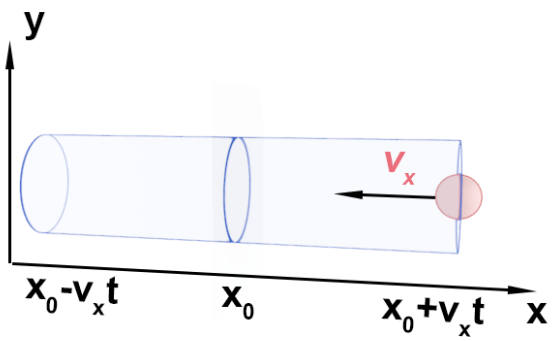

Figure 1.4. Schematic of heat flow

Heat conduction is energy flow carried by particles, including electrons and phonons. The transport can be under appropriate conditions described by classical kinetic theory. With this assumption, thermal transport is motivated by a temperature difference, as shown in figure 1.4. The heat flow through a surface q equals to

$$Q = Q^{+} - Q^{-} = \frac{1}{2}(nv_x E)_{x_0 - v_x\tau} - \frac{1}{2}(nv_x E)_{x_0 + v_x\tau} \tag{1.4}$$

where n, v_x, E and τ are the number of carriers in a unit volume, the velocity of carriers in the *x*-direction, average energy carried by the single particles, and the time to traverse a mean free path during which no collision occurs, respectively. This leads to the following relation.

$$\begin{aligned} Q &= -\frac{1}{2}(2v_x\tau)\frac{d(nv_x E)}{dx}|_{x=x_0} \\ &= -\frac{1}{3}nv\Lambda\frac{dE}{dx}|_{x=x_0} \\ &= -\frac{1}{3}nv\Lambda\frac{dE}{dT}\frac{dT}{dx}|_{x=x_0} \\ &= -\frac{1}{3}nmv\Lambda C_M\frac{dT}{dx}|_{x=x_0} \end{aligned} \tag{1.5}$$

The thermal conductivity can be defined as

$$k = -\frac{1}{3}v\Lambda C_v \tag{1.6}$$

$$C_V = C_M nm = C_M\rho \tag{1.7}$$

where ρ, Λ, C_M and C_V are the phonon density, mean free path, mass specific heat capacity and volumetric specific heat capacity, respectively.[18-19] For different thermal carriers, the formula is affected. For example, for phonons

$$k_{ph} = -\frac{1}{3}v_a\Lambda_{ph}C_V \tag{1.8}$$

where v_a and Λ_{ph} are velocity of phonon and average free path of phonon. Electron has

$$k_e = -\frac{1}{3}\rho v_F \Lambda_e C_{V,e} \quad (1.9)$$

where ρ, v_F, Λ_e and $C_{V,e}$ are mass of electrons in a unit volume, the Fermi velocity, electron mean free path, and $C_{v,e}$ is specific heat of electrons, respectively.[18] Then the thermal conductivity of conductor can be calculated as[20]

$$k = k_{ph} + k_e \quad (1.10)$$

Furthermore, k_{ph} and k_e can be discussed in detail.

1.3.1.1 Heat transfer carried by phonon

In physics, a phonon is defined as a collective excitation in a periodic, elastic arrangement of atoms or molecules in condensed matter. Heat transport in insulators, where most electrons are tightly localized about a nucleus, is primarily dominated by phonon-mediated heat transfer. Assuming a crystal contains N atoms, each of which contains 3 vibrational degrees of freedom, there are 3*N* vibrational modes:

$$3N = \sum_{\boldsymbol{k_x}} \sum_{\boldsymbol{k_y}} \sum_{\boldsymbol{k_z}} 1 \quad (1.11)$$

In unite volume we have

$$\frac{3N}{V} = \int_0^{w_D} D(w)dw \quad (1.12)$$

where w_D and $D(w)$ stand for Debye frequency and phonon density of states (PDOS). PDOS describes the number of states in unite volume and unite frequency. According to Debye model, w_D is the highest frequent of lattice vibration. It should be noted that not all states are occupied. The distribution of phonon on the states at w frequency obeys the Bose-Einstein distribution, which is described as

$$f_{BE}(w) = \frac{1}{e^{\frac{\hbar w}{k_B T}} - 1} \quad (1.13)$$

h and k_B is Planck constant (6.626 x 10^{-34} J s) and Boltzmann constant (1.381 x 10^{-23} J K^{-1}) respectively. According to the analysis, vibration

contribution to internal energy in the unite volume can be expressed as

$$E = \int_0^{w_D} hw f_{BE}(w)\, D(w) dw \tag{1.14}$$

here hw is the energy carried by single phonon on the specific energy level. Considering the relationship between E and C_V , thermal conductivity can be wrote as

$$k = \int_0^{w_D} v_{g,n}^2(w)\tau(w) hw \frac{df_{BE}(w)}{dT} D(w) dw \tag{1.15}$$

$$k = k_B \int_0^{w_D} v_{g,n}^2(w)\tau(w) (\frac{hw}{k_B T})^2 \frac{e^{\frac{hw}{k_B T}}}{(e^{\frac{hw}{k_B T}}+1)^2} hw D(w) dw \tag{1.16}$$

where $v_{g,n}$ is the group velocity of phonons on the direction along which thermal conductivity is calculated.

1.3.1.2 Heat transfer carried by electron

The thermal conductivity of electron is coming from Boltzmann transport equation (BTE). The general form of BTE is write as

$$\frac{df}{dt} = \left(\frac{\partial f}{\partial t}\right)_{force} + \left(\frac{\partial f}{\partial t}\right)_{diss} + \left(\frac{\partial f}{\partial t}\right)_{coll} \tag{1.17}$$

where the three terms on the right side represent the influence of the extra field, dissipation and collision. Here under the steady state approximation, local steady state approximation and relaxation time approximation

$$\frac{df}{dt} = 0 \tag{1.18}$$

$$\frac{df_0}{dt} = \frac{df}{dt} \tag{1.19}$$

$$\left(\frac{\partial f}{\partial t}\right)_{coll} = \frac{f_0 - f}{\tau} \tag{1.20}$$

where f_0 is the distribution function under the steady state, which is Fermi-Dirac distribution for electron, we have

$$f = \tau \left[\left(\frac{\partial f_{FD}}{\partial t}\right)_{force} + \left(\frac{\partial f_{FD}}{\partial t}\right)_{diss}\right] + f_{FD} \tag{1.21}$$

Now, assuming there is not extra field. BTE can be simplified to

$$f = \tau\left(\frac{\partial f_{FD}}{\partial t}\right)_{diss} + f_{FD} \quad (1.22)$$

$$f(\varepsilon, T) = \tau v_z \frac{\partial f_{FD}}{\partial t}\frac{\partial T}{\partial z} + f_{FD}(\varepsilon, T) \quad (1.23)$$

where v_z is the velocity along z direction. In an open system,

$$dU = \delta Q - \mu dN \quad (1.24)$$

Heat flux is expressed as

$$Q_z'' = J_E - \mu J_N = \int_0^\infty v_z(\varepsilon - \mu)\left(f_{FD}(\varepsilon, T) - \tau(\varepsilon, T) v_z \frac{\partial f_{FD}}{\partial t}\frac{\partial T}{\partial z}\right) D(\varepsilon) d\varepsilon \quad (1.25)$$

Where the replacement ${v_x}^2 = \frac{2\varepsilon}{3m_e}$ is performed under the assumption that the velocities are isotropic. The formula expresses the energy flow in one direction, for example, from point 1 to point 2. At the same time, energy also flows in the opposite direction, from point 2 to point 1. Considering the first term, $v_x(\varepsilon - \mu) f_{FD}(\varepsilon, T)\ D(\varepsilon)$, represent the heat transfer under a balanced state, the integration of the term should be 0. Thermal conductivity can be written as

$$k = \frac{2}{3m_e}\int_0^\infty (\varepsilon - \mu)\tau(\varepsilon, T)\varepsilon \frac{\partial f_{FD}}{\partial t} D(\varepsilon) d\varepsilon \quad (1.26)$$

1.3.2 Molecular Simulation

1.3.2.1 Non-equilibrium molecular simulation

Molecular simulation can deduce the movement of atoms driven by the interaction between atoms. Considering that the temperature of a material is a kind of vibration, this tool has been applied to predict the thermal conductivity of materials since the earliest days of computer simulations for physical systems.[21-29] There are two primary methods, non-equilibrium molecular simulation (NEMD) and equilibrium molecular simulation (EMD), to predict material thermal properties based on statistical mechanical theories under appropriate conditions.

Non-equilibrium molecular simulation is directly based on the definition of thermal conductivity. The material system is built within a simulation cell. Considering the relationship between temperature and translational energy, the mean energy at equilibrium for a particle (or atom) is

$$\mathrm{E} = \frac{3}{2}k_B T = \int_0^\infty \left(\frac{1}{2}mv^2\right) f(v)dv \tag{1.27}$$

the relationship between temperature and velocity can be established. By monitoring the movement of atoms, we can record temperature indirectly. The injection of energy can be achieved by the time the velocity with a reasonable coefficient.

Now that the injection of energy and temperature monitoring is practical, it would not be hard to simulate the physical process. Exert specified amount of heat energy into one end of the simulation box and fix the temperature of the other end. Under the influence of the heat, the temperature of the system rises heterogeneously. The temperature gradient can be recorded. According to the definition of thermal conductivity, thermal conductivity can be calculated as

$$k = -\frac{\vec{Q}}{\vec{\nabla}T} \tag{1.28}$$

1.3.2.2 equilibrium molecular simulation

EMD is based on the fluctuation-dissipation theorem (FDT) proposed by Nyquist in 1928 and developed by Callen, Welton, Kube and many other researchers.[30-33] The theory describes the fluctuation near the equilibrium from the point of view of statistical mechanics. According to the defining relationship for FDT, dissipated work can be expressed as

$$W_{diss} \approx \frac{\beta\sigma^2}{2} \tag{1.29}$$

where σ is the standard deviation of measurement of power. This theory

is applied in different fields, including electrical noise analysis[34-37], biological[38-40], plasmas[41-43] and even finance[44-45]. In the heat transport field, according to FDT

$$k = \frac{1}{kT^2V}\int_0^\infty < Q_x(t), Q_x(0) > dt \qquad (1.30)$$

where Q_x is the total heat flux on x direction. as discussed above, we can monitor energy, so the thermal conductivity can be calculated.[46]

1.3.3 Thermal conductivity of composites

According to classical kinetic theory, the calculation of thermal conductivity is based on periodic assumption for deriving the phonon density of states. The analysis is suitable for an infinite lattice model or crystal. However, for amorphous structures, the concept of phonon is difficult to define. Thus, in many limiting cases, it is best described by localized vibrational modes (LVMs). Molecular simulations have been developed according to the definition of thermal conductivity or according to FDT. These simulations can provide improved results in closer agreement with the experiment, especially when predicting the thermal properties of amorphous polymers and polycrystals whose non-ideal structures have an impact on thermal conductivity.[21-25] Additionally, there are simulations where the analysis is applied to the thermal conductivity of polymers.[26-29] However, molecular dynamics simulations are unable to describe the electron thermal conductivity. Hence, in this thesis, going beyond the simpler models is necessary to provide results that can be directly compared to measured data.

Another limitation of molecular simulation is the use of finite simulation cells. Since molecular simulations require setting up models at an atomic scale, for practical MD simulations, the cell is too small to provide a

structure as large as required to describe a typical filler. Diameters of carbon fibers, AlN, Al_2O_3, graphite, and diamond are generally larger than a 100 nm. This problem may be partially solved by introducing periodic boundary conditions or to consider heat flow across a single interface and using multiscale models to describe larger simulations based on the atomic scale modelling. However, when the composites containing these fillers are also modeled, practical MD simulations cannot easily overcome the scale problem. Hence the development of models predicting the thermal conductivity of composite based on macro parameters like filler concentration, scale and shape are valuable. Because of the variation of parameters, it is a challenging mission to unify them in a single predictive theory. Dr. Yu summarized the common models in 2012 in his PhD thesis.[47] The past 10 years have witnessed the advancement of some newer theories. Here some models developed after 2012 are listed in table 1.1.

Table 1.1. The models predict thermal conductivity of composite.

Name of models	Formulas	Applications	Published year
Li Zhou's model[48]	$k_{eff} = \frac{2\lambda_m(1-C)}{l}\int_0^{\frac{l}{2}} \frac{(y^2+\frac{l^2}{4})^{\frac{3}{2}}}{(y^2+\frac{l^2}{4})^{\frac{3}{2}}+a^3C}dy$	spherical particle	2019
Chuan-Yong Zhu's model[49]	$\frac{k_{eff}}{k_m} = \left(\frac{2+2\sum_k(\phi_p\beta_e)_i}{2-\sum_k(\phi_p\beta_e)_i}\right)\left(\frac{2+\sum_k((2\beta_e-1)\phi_p)_i}{2-\sum_k((\beta_e+1)\phi_p)_i}\right)$	single type of particles, hybrid particles, and core-shell particles	2021

Dae Han Sung's model[50]	$k_{a,ip} = f_{ip}k_a + (1 - f_{ip})k_m$ $k_{t,ip} = \frac{k_m}{4}[\sqrt{(1 - f_{ip})^2\left(\frac{k_t}{k_m} - 1\right)^2 + \frac{4k_t}{k_m}} - (1 - f_{ip})(\frac{k_t}{k_m} - 1)]^2$	Carbon-containing fiber-reinforced and multiscale hybrid composite	2018
Dayanidhi Jena's model[51]	$k_e = \frac{sk_ak_bk_c}{k_ak_c[s - 2(r_1 + r_2)] + 2k_b[r_1k_c + r_2k_a]}$ (FVF<13.08) $k_e = \frac{sk_ak_c}{2(r_1k_c + r_2k_a)}$ (13.08<FVF<20.307) $k_e = \frac{sk_ak_b}{2r1k_b + (s - 2r1)k_a}$ (FVF>20.307)	hybrid composite as per its fiber volume faction	2021
Yuan Fang's model[52]	$\frac{k_e^1}{k_1} = \frac{2V_1}{2V_1 + 3V_{m1}}$ $\frac{k_{eff}}{k_2} \approx \frac{\left(\frac{2k_2}{hR_1} + 1\right) - 2(V_1 + V_{m1})(\frac{k_2}{hR_1} - 1)}{\left(\frac{2k_2}{hR_1} + 1\right) + (V_1 + V_{m1})(\frac{k_2}{hR_1} - 1)}$	CNTs-reinforced composites with and without percolated CNTs	2021
LiChuan Zhou's model[53]	$k_{y\perp} = f(v_{yf})k_{PL} + [1 - f(v_{yf})]k_{CLT}$	Porous material	2019

Dan Dan's model[54]	$\lambda_c = \frac{Q_1 + Q_2 + Q_3 + Q_4}{\Delta T \frac{a}{2}}$ $= \frac{2\lambda_s[\frac{a^2 - \pi r^2}{2} + 2\arccos\left(\frac{a}{2r}\right) r^2 - a\sqrt{r^2 - (\frac{a}{2r})^2}]}{a^2}$ $+ \lambda_g \pi \left(\frac{r^2}{a^2} - \frac{1}{4}\right)$ $- \frac{\lambda_s \pi}{k^2 a}\left[kr(cos\theta_1 - cos\theta_0) - \frac{a}{2}\ln\left(\frac{krcos\theta_1 + \frac{a}{2}}{krcos\theta_0 + \frac{a}{2}}\right)\right]$ $+ \frac{4}{a}\int_{\frac{a}{2}}^{r} \frac{\arcsin(\frac{\frac{a}{2} - \sqrt{x^2 - \frac{a^2}{4}}}{\sqrt{2}x})xdx}{\frac{\sqrt{r^2 - x^2}}{\lambda_g} + \frac{(\frac{a}{2} - \sqrt{r^2 - x^2})}{\lambda_s}}$	through gases and solid skeleton, aerogel	2014
Hakim Abbasov's model[55]	k_{eff} $= p\varphi\left\{k_p\left[1 - (1-\varphi)^{\frac{2}{3}}\right] + \frac{k_{pol}}{(1-\varphi)^{-\frac{2}{3}} - \beta\left[(1-\varphi)^{-\frac{2}{3}} - (1-\varphi)^{-\frac{1}{3}}\right]}\right\} + (1$ $- p\varphi)[\left(1 - \sqrt[3]{\frac{9\pi\varphi^2}{16}}\right)k_{pol}$ $- \frac{\pi k_{pol}}{2\beta^2}\ln\left(1 - 2\beta\sqrt[3]{\frac{3\varphi}{4\pi}}\right) - \frac{k_{pol}}{\beta}\sqrt[3]{\frac{3\pi^2\varphi}{4}}]$	polymer composite filled with high conductive particles	2022
Deepti Chauhan's model (modified Maxwell's model)[56]	$k_e = k_m \frac{k_e + 2k_m + 2\phi_e(k_f + k_m)}{k_e + 2k_m - \phi_e(k_f + k_m)}$	Materials of different sizes of filler particles/matrix	2013

1.4 Promoting thermal conductivity of polymer composites

Thermal conductive composites consist of matrix and thermal conductive fillers. To promote heat transportation ability of composite, there are three strategies which are promoting the intrinsic thermal conductivity of matrix, using fillers with high thermal conductivity and optimizing the fabricating methods.

1.4.1 Promoting the intrinsic thermal conductivity of polymers

Relying on low cost, ease of processing and modifiability, polymers have become the most commonly used matrix material. However, general bulk polymers are generally regarded as thermal insulators whose thermal conductivities are lower than 1 W m^{-1} K^{-1}, a partial listing of the thermal conductivity of various polymers are given in table 1.2.[57-60] The data is from Matweb database.

Table 1.2. Thermal conductivity of commercial polymers

Polymers		Thermal Conductivity (W m-1 K-1)
Thermal-plastic	High Density Polyethylene (HDPE)	0.28-0.48
	Acrylonitrile Butadiene Styrene Copolymers (ABS)	0.12-0.20
	Polycarbonate (PC)	0.16-0.26
	Polyamide (PA)	0.16-0.29
	polypropylene (PP)	0.17-0.40
	Polystyrene (PS)	0.12-0.18
	Polyvinyl Chloride (PVC)	0.07-0.12

	Thermal Plastic Polyimide (TPI)	0.17-0.35
	Polyethylene Terephthalate (PET)	0.04-0.29
	Poly(ether-ether-ketone) (PEEK)	0.04-0.95
Thermal-set	Epoxy	0.17-0.80
	Polyimide (PI)	0.12-0.29
	Silicone Rubber	0.18
	polyurethane (PU)	0-0.83

Compared with the materials used as filler which generally exhibit good heat transport character, thermal conductivities for polymers are poor. On the contrary, considering that some polymers have a high degree of crystallinity and that strong covalent bonds from the polymer chains, they are anticipated to achieve comparable thermal conductivity as some ceramics. This contrast between the low thermal conductivity of commercial polymers and the expectation that high thermal conductivity should be achievable attracted numerous researchers to study the influences on thermal conductivity of polymers fillers by considering such factors as chain orientation[61-71], cross-link density[72-73], intra- and inter-chain interactions[61, 64, 74-75], crystallinity, molecular weight[25, 76], side chains[76-78], branching and cross-linking of polymers[75, 79-81], and lot others.[82] All these characters can be grouped into the molecular design and polymer morphology. In recent decades, the most attractive achievement in molecular design within this field is the promotion of thermal conductivity by introducing liquid crystal-like structures into polymers or constructing liquid crystal polymers (LCP), which in the polymer morphology field, it is realized by aligning the molecular chains by stretching.

1.4.1.1 Liquid crystal polymers

Liquid crystal polymers are a type of thermoset resin produced from the polymerization of functionalized liquid crystal monomers consisting of rigid rod-shaped mesogens, special flexible segments and active end groups.[83] The rigid rod-shaped mesogens usually contain aromatic structures between which the π-π conjugation enhances the construction of an organic crystal, enhancing the heat transport. As a result, the thermal conductivity of LCP is usually anisotropic, which displays better thermal transport capability along the molecular chain.

The most used two end groups in this field are acrylic acid and epoxy. Due to the conjugation between the aromatic structure composing rigid rod-shaped mesogens, liquid crystal tends to align and form a crystal-like structure in terms of alignment of the polymer chains, as discussed, which is related to thermal conductivity. By molecular design and process optimization, the alignment of the crystal polymers can be enhanced. Related works are shown in table 1.3.

Table 1.3. The thermal conductivity of liquid crystal polymers with different structure and processing

End group	Acrylic acid Thermal Conductivity	year	Ref.	Epoxy Thermal Conductivity	year	Ref.
Molecular design	5.2 W m^{-1} K^{-1}	1993	[84]	0.96 W m^{-1} K^{-1}	2003	[85]
	0.68 W m^{-1} K^{-1}	2007	[86]	0.2 W m^{-1} K^{-1}	2006	[87]
	2.24 W m^{-1} K^{-1}	2017	[88]	0.2 W m^{-1} K^{-1}	2007	[89]

			0.38 W m^{-1} K^{-1}	2013	[90]
			0.48 W m^{-1} K^{-1}	2018	[91]
			0.51 W m^{-1} K^{-1}	2019	[92]
			1.2 W m^{-1} K^{-1}	2020	[93]
			5.8 W m^{-1} K^{-1}	2020	[94]
			10 W m^{-1} K^{-1}	2021	[95]
Processing optimization	0.34 W m^{-1} K^{-1}	2016 [96]	0.89 W m^{-1} K^{-1}	2003	[97]
	2.5 W m^{-1} K^{-1}	2016 [78]			
	1.2 W m^{-1} K^{-1}	2018 [98]			

The earliest known author using LCPs to achieve high thermal conductivity was reported by Kurt Geibel in 1993, using diacrylates.[84] In the study, different rod-shaped mesogenic unit was introduced to optimize the primary structure. The highest thermal conductivity of the LCPs is beyond 5 W m^{-1} K^{-1}.

Takashi *et al.* constructed an LCP monomer with different functionality.[86] Mono- and bi-functional monomers with similar rod-shaped mesogens were synthesized and used to construct polymer. According to the analysis, the polymer network goes through the direction perpendicular to the rubbing direction of the mono-functional compound. On the contrary, the network in a bi-functional compound relies more on the rubbing direction in a di-functional compound. This difference is illustrated in figure 1.5. As the bi-functional monomer increases, thermal

conductivity along the direction perpendicular to the rubbing direction does not significantly change, increasing a modest value of 0.68 W m^{-1} K^{-1}.

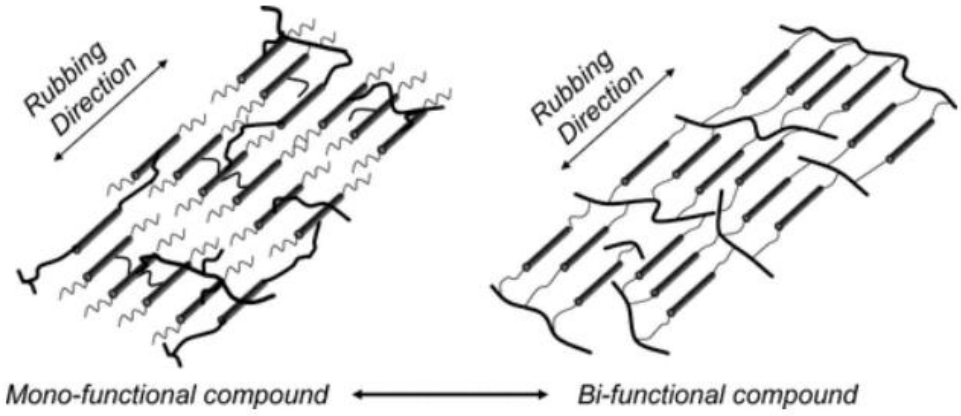

Figure 1.5. Illustrations of molecular alignment in homogeneous alignment films.[86]

Dong-Guede *et al.* reported an acrylic acid functionalized liquid crystal polymer used as thermal conductive material[98] In their study, a liquid crystal monomer with an anisotropic rod-shaped molecular structure was designed and synthesized. The monomer was aligned by application of a magnetic field, as shown in Figure 1.6, and in-situ photopolymerized. The thermal conductivity of the final product is 1.2 W m^{-1} K^{-1}.

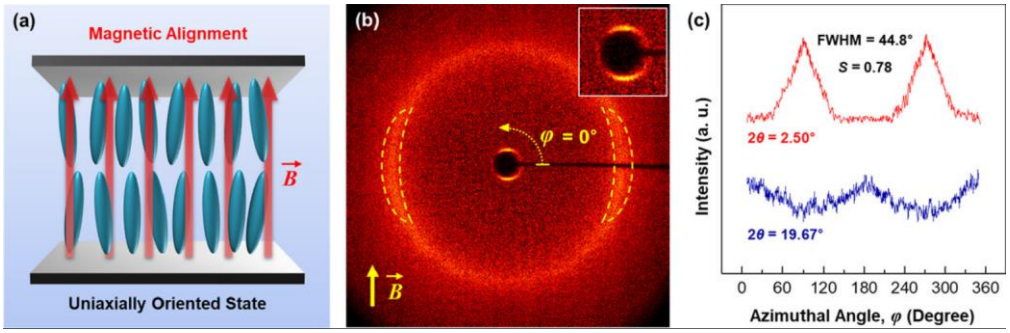

Figure 1.6. (a) Schematic illustration of the uniaxially aligned liquid crystal monomer under a magnetic field. (b) 2D WAXD pattern of LCP film. The insert presents the magnified image of low-angle diffraction. (c) Azimuthal scans between 2.3° and 2.7° and between 18° and 21° [98]

The primary structure of LCP is the most studied characteristic of these polymers. Unlike acrylic acid, epoxy LCPs are polymerized from monomer and initiator, both of which impact the thermal character. In 2003 Akatsuka *et al.* studied the relationship between epoxy LCP's monomers and thermal conductivity.[85] The LCPs with benzoate and diphenol structures as rod-shaped mesogens were first compared. Then the length of the flexible segment was investigated. With the shrinking of the flexible segment from 8 to 4 (the number of –CH2 – groups in the flexible segment), the thermal conductivity of the LCP increases from 0.85 to 0.96 W m^{-1} K^{-1}, which is approximately 5 times that of common epoxy.

Akherul *et al.* also studied the relationship between molecular structure and thermal conductivity. In their study, linear and non-linear initiators were used to construct LCPs. According to the discussion, non-linear initiators caused molecular disorder, which is a possible source of phonon scattering. Consistent with this supposition, the thermal conductivity of LCP constructed with a non-linear initiator is lower, as figure 1.7 shows. It is worth noting that the different structures of initiator can be regarded as the difference in functional groups. From this point of view, this report, together with Takashi's report, demonstrated that the use of two functional monomers or initiators might result in higher thermal conductivity due to the formation of a linear heat path.[86, 91]

The secondary structure also has an impact on thermal conductivity. With the help of magnetic or electric force, LCP molecular chain can be aligned. This phenomenon is widely applied in display applications. Miyuki et al. used a magnetic field to align the monomer of LCP and doubled the

thermal conductivity along the magnetic field direction.[97] In the report, the highest thermal conductivity is 0.9 W m^{-1} K^{-1}.

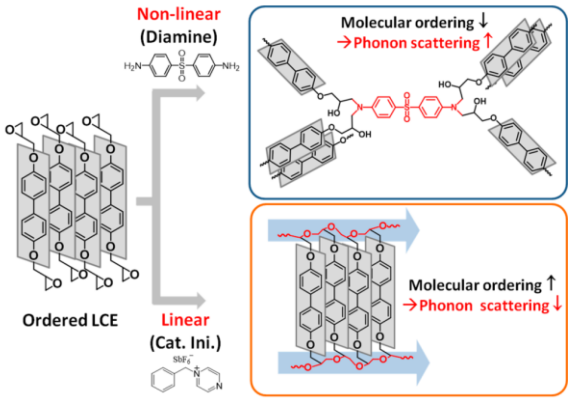

Figure 1.7. Molecular disorder caused by the introduction of non-linear initiator. [91]

The highest value in the field overall is reported by Ning *et al.* in 2020, reaching a value of 10 W m^{-1} K^{-1}. [95] From the liquid crystal molecular structure shown in Figure 1.8, it is clear to see, in contrast to previous LCP studies, that the structure of the mesogens was given particular attention. From the cyclohexane structure, the mesogens gain inherent flexibility. As an aside, this ground-breaking result is explained by the orientation of the LCPs in their report. However, perhaps a more convincing explanation is required for the enhancement relative to other aligned LCPs.

As mentioned, compared to acrylic acid ended LCPs, the epoxy ended LCP monomer has attracted more attention in experimental studies. There is a comprehensive review published in 2021 by Kunpeng *et al.* which summarizes the majority of these investigations.[99] And from the discussions in this thesis, it may be concluded that the thermal conductivity of LCPs is strongly correlated to molecular chain alignment. No matter if a clever molecular design or the application of an external electric or magnetic field, researchers tend to maximize the alignment of

the LCP chain to promote thermal conductivity.

In addition to acrylic acid and epoxy end groups, there are a small number of other end groups that have been considered.[100-102] And with the assistance of thermal conductive filler, LCP can be used to construct functional thermal management or composite.[63, 103-105]

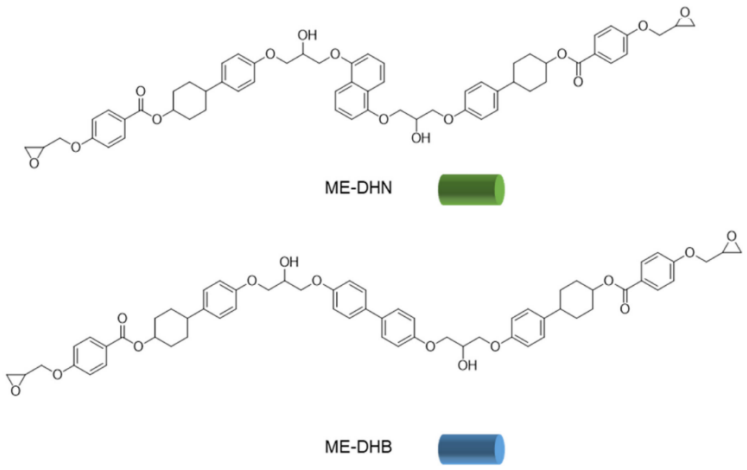

Figure 1.8. The epoxy liquid crystal monomer and initiator structures. [95]

1.4.1.2 Stretching polymer chain

Stretching polymer chain is another important road promoting intrinsic thermal conductivity of the polymer. Similar to LCP, the guiding philosophy induces the alignment of polymer chains.[106-107]

Numerous researches have predicted the thermal conductivity enhancements(TCE) related to the polymer chain stretch. According to simulation results, thermal conductivities of a single polyethylene chain can be beyond 100 W m^{-1} K^{-1} on the chain direction, which is similar to the value of metals.[21, 108-111]

Choy et al. performed a demonstration where he pointed out the relationship between the drawing ratio and the thermal conductivity.[112-114] When the drawing ratio exceeds 300, the thermal conductivity of ultrahigh molecular weight polyethylene can exceed 40 W m^{-1} K^{-1}, as figure 1.9 shows. In 1997, Fuji Shiro et al. studied the thermal conductivity difference between the axial and transverse direction of the polymer by testing the thermal conductivity of Poly benzobisoxazole fiber, which is about 100 W m^{-1} K^{-1}.[115]

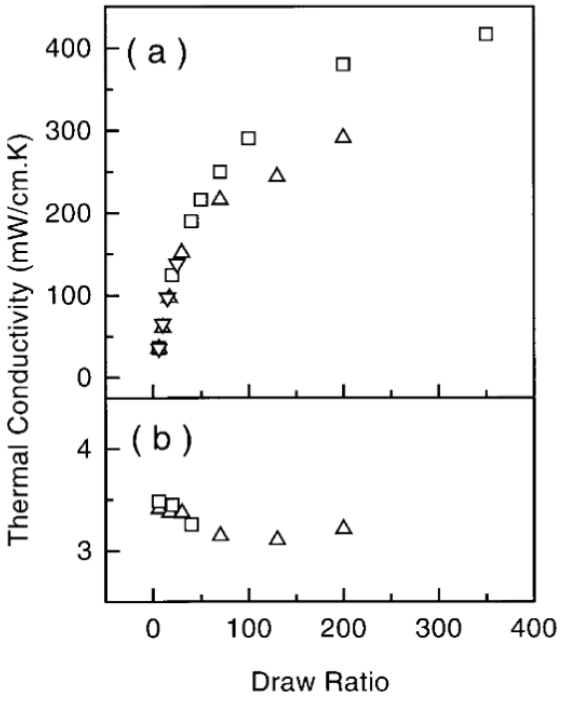

Figure 1.9. Axial and transverse thermal conductivity of PE versus draw ratio at 295 K. ▽, melt-crystallized PE;△, gel PE; □, singlecrystal mat PE.[113]

By applying two stage heat, Sheng et al. achieved 104 W m^{-1} K^{-1}.[67] To date, this value is still a peak in the field. The extreme thermal conductivity was attributed to improved crystallinity in the discussion, which was confirmed by other researchers achieving high intrinsic thermal conductivity by stretching polymers in the past few years.[116-118] However, the low thermal conductivity and high crystallinity of many

commercial polymers like HDPE seem counter-examples of the conclusion. This contradiction was explained in 2017 by Bowen et al. by amorphous restructuring. [119] In the study, polyethylene heat-stretched achieved 51 W m^{-1} K^{-1}, although the crystallinity decreased from 92% to 83%, as figure 1.10 shows. According to the report, the thermal conductivity promotion is not only related to crystallinity but also to the overall chain alignment.

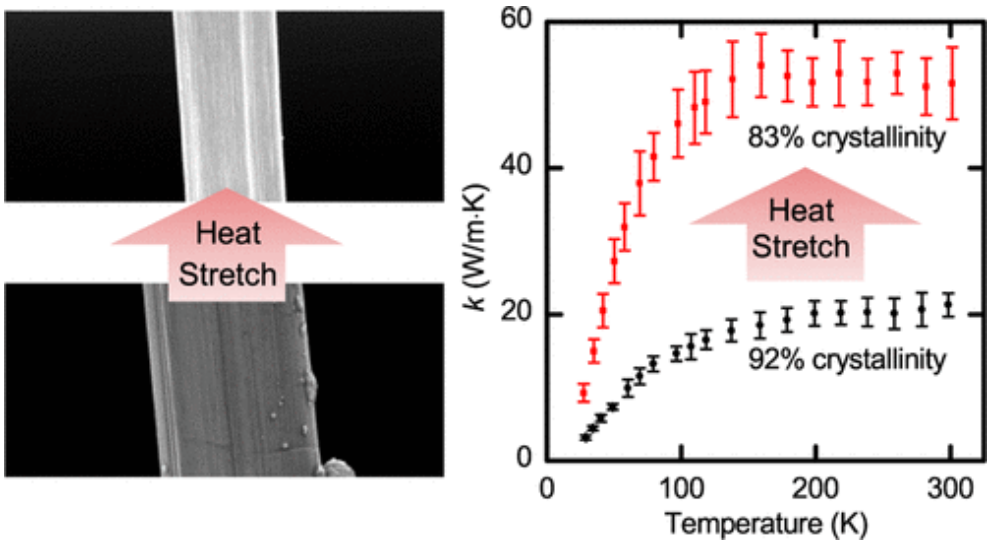

Figure 1.10. The scanning electron microscope (SEM) images and thermal conductivity of PE before and after heat stretching at different temperature.[119]

1.4.2 Property of fillers

Thermal conductivities of commercial polymers are generally low, as discussed, especially several years before when promoting the intrinsic thermal conductivity of polymer was still a challenge. To meet the requirement of heat dissipation, the general strategy is to construct composites with thermal conductive filler and polymer matrix. Fillers shoulder the heat transport and matrix endow composite with low density, flexibility and other mechanical property. The fillers have a substantial impact on the resulted thermal conductivity of composites. The

relationship between thermal conductivity and characters of filler like size, dispersion, the interaction between filer and matrix, synergistic effect, and construction of the network is studied. Here, different thermal conductive fillers are discussed in these aspects.

1.4.2.1 Metals and metallic oxide

Among traditional materials, metals are regarded as one kind of material with the highest thermal conductivity. The thermal conductivities of some common metals are listed in Table 1.4.

Table 1.4. Thermal conductivity of metals.

Metals	Thermal conductivity (W m^{-1} K^{-1})
Ti	17
Sn	63.2
Mg	159
Fe	76.2
Al	210
Ag	419
Cu	385
Si	124
W	163

Considering thermal conductivity and cost of materials, the most used metals in heat transport are Cu and Al. Copper pipe and heat sink, aluminum fine are important thermal management components of the electronic system. To introduce the development of thermal conductive metal composites, the impact of the structure of metal filler, including special structures and liquid metals, along with the character of overall composite like filler concentration, process and construction of network on the property of composites should be discussed. Different from ceramic, diamond and polymer thermal conductive fillers, composites of

metals inherited not only thermal conductivity but also high electronic conductivity from metals, which helps them to outstand electronic properties, including electromagnetic shielding, dielectric loss and dielectric constant. [120-121]

Liquid metal (LM) is a special class in thermal conductive fillers. As a metal, LM exhibits high thermal conductive characteristics.[122-125] Meanwhile, the fluidity and deformability of liquid metal make sure they touch with heat source and heat sink, which helps compromise thermal resistance. [126-127]Although exhibiting such advantages, the application of liquid metal was still precluded by its corrosivity to other metals and the leakage problem.

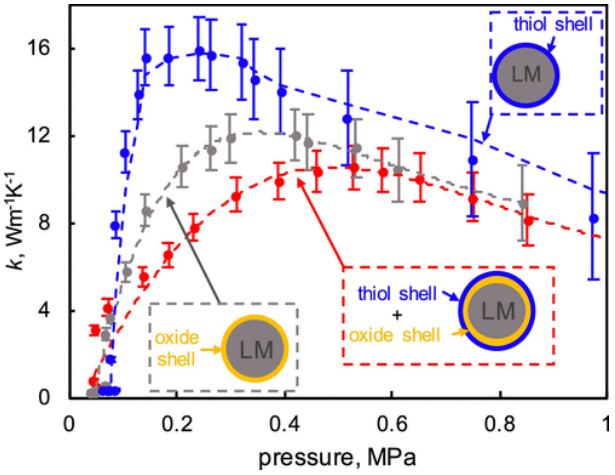

Figure 1.11. Thermal conductivity (k) of LM capsule beds as a function of the applied compressive pressure

Besides being used as filler, metal was also used as a cover on the polymer to form a heat exchanger. In these examples, the micromorphology of metal has a nonnegligible impact on thermal conductivity, as figure 1.12 shows.[128-129] The effect of structure on thermal conductivity of related structures was analyzed using a mathematical model.[130]

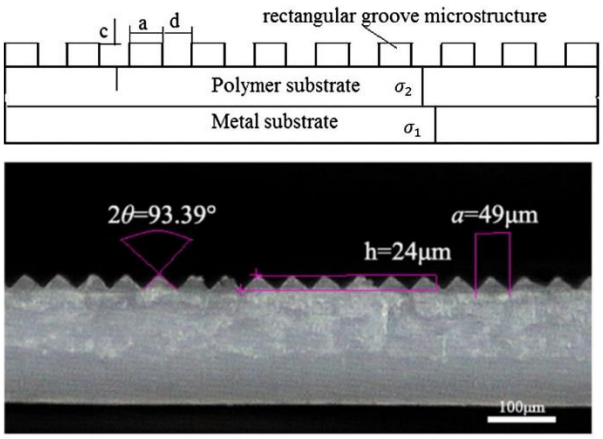

Figure 1.12. Some special groove microstructure of metal covered thermal exchangers [128]

The shortcut of metal is its heaviness and insufficient resistance to corrosion. These characters limited their application.

1.4.2.2 Ceramics

Ceramics are materials with high thermal conductivity. According to measurement and theoretical calculation, some ceramics are found to have thermal conductivity beyond 300 W m^{-1} K^{-1}, including AlN, SiC and boron nitride. Besides, some ceramics like Boron arsenide have been pointed out to have 2000 W m^{-1} K^{-1}, which is comparable with diamond.[131] Here, the measured thermal conductivities of ceramics are listed in table 1.5, and a brief introduction of ceramics' thermal conductivity was given. One of ceramics' valuable characteristics is insulating property. As introduced, heat can be transported by carriers, including electrons and phonons. The high thermal conductivity of metals is partly profit from their electronic conductivity. Unlike metal, graphene and carbon fiber(CF), ceramics like AlN, Al_2O_3 and boron nitride are insulators, which indicate that the heat is totally carried by phonon. The character makes ceramics

qualified for some special tasks in an electronic system.

Table 1.5. The thermal conductivity of general ceramics

Ceramics	Thermal conductivity ($W\ m^{-1}\ K^{-1}$)
Al_2O_3	20-40
SiC	100-180
AlN	250
boron nitride	1300 (in plane) 2 (Through plane)
TiB_2	60-120
BeO	250-325
WC	100

Alumina, as one of the traditional thermal management materials, has been widely used in constructing thermal conductive composite.[132-135] The thermal conductivity of Al_2O_3 is about 20-40 $W\ m^{-1}\ K^{-1}$ varying with the process method and crystal structure. The highest value belongs to alpha alumina. Although its performance is not as good as the ceramics following but still hundreds of times of polymers. Considering the low cost, hardness and maturity of processing technology, Al_2O_3 is still widely used.

AlN ceramic is also a widely used thermal conductive material that attracted much attention in the 1980s. The thermal conductivity is about 250 $W\ m^{-1}\ K^{-1}$ and exhibits a similar coefficient of thermal expansion(CTE) with silica.[136] Relying on these advantages, AlN possesses the ability to be a potential thermal conductive package material.[137-139]

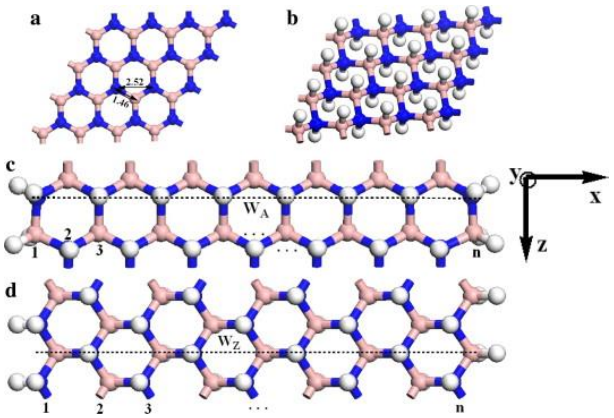

Figure 1.13. Structure of boron nitride in different view[140]. (a) The monolayer hexagonal boron nitride sheet (h-BN) and (b) The hydrogenated BN sheet in the chair conformation. Schematic representation of hydrogenated armchair (c) and zigzag (d) boron nitride nanoribbons.

Boron nitride is one of the most popular thermal conductive fillers, which has a similar structure to graphene, as figure 1.13 shows.[140-143] Boron nitride is a representative 2D anisotropic thermal conductive filler whose in-plane thermal conductivity in single crystal form is high to 1300 W m^{-1} K^{-1} while in through-plane, the value is only 2 W m^{-1} K^{-1}.[136, 144-146] To take the best advantage of Boron nitride, researchers tend to align the sheets in a specific plane or construct thermal conductive network so that the high thermal conductivity of raw material can be concentrated on the designed direction.[147-149]

Silicon carbide (SiC) as an important ceramic is also used in thermal conductive composite. [150-152] Meanwhile SiC can also be used as element of hybrid filer.[153-156]

1.4.2.3 Carbon materials

Carbon materials are a broad group of materials, including carbon fiber, graphene, diamond and polymers. Thanks to the variety of carbon

materials' structures, the thermal conductivities of these materials span from 0.1 to 2000 W m^{-1} K^{-1}. Specifically, graphene, diamond and carbon fiber exhibit thermal conductivity higher than 1000 W m-^{1} K^{-1}, while the values of bulk polymers generally are lower than 1 W m^{-1} K^{-1}.

Graphene is an important and widely used thermal management material whose thermal conductivity is high to 1500 W m^{-1} K^{-1}. As 2D material, graphene can be considered an anisotropic material. The high in-plane thermal conductivity can efficiently accelerate the heat transport in the direction. As a result, similar to boron nitride, to make full use of the high anisotropic thermal conductivity, much effort was made in this field to align graphene sheets or construct the thermal conductive network.[157-160] On the other hand, unlike boron nitride, graphene sheet is soft, so besides being used solely, graphene is often used as the bridge material between other thermal conductive fillers.[161]

The structure of a carbon nanotube seems like a tube of graphene. Theoretically, a carbon nanotube is a 1D anisotropic filler. If the nanotube can be aligned and unwound in cases, the high thermal conductivity of the material can be released.[162-163] This result can be achieved with different methods.[164-165] In other cases, they are used as hybrid fillers to enhance the interaction between major fillers and matrix or to bridge the significant fillers.[166-168]

Carbon fiber as a 1D filler exhibits anisotropic thermal conductivity in axial and radial directions. Commercial CFs can be classified into PAN-based CF and pitch-based CF according to the precursor. In term of mechanical, PAN-based CF have better strength while the pitch-based CF has better

modulus. When it comes to thermal property, pitch-based CF performs much better. In the axial direction, up to now, the highest value of commercial CF is 1000 W m^{-1} K^{-1} and the value is still growing with the development of technology. In the other direction, thermal conductivity is generally lower than 10 W m^{-1} K^{-1}, which can almost be ignored. Aligning CF is an efficient method to synthesize thermal conductive composite. As long macroscopical fiber, the aligning of CF should have been easy, but the strength of CF is challenging to cut the produced composite, especially along the direction perpendicular to CF. As a result, most reported CF thermal conductive composite is made by milled CF.

Diamond is another good carbon thermal conductive material. The sp^3 atom structure of diamond differs from other carbon materials, whether graphene or CF, which are formed by sp^2 carbon. According to calculation, the thermal conductivity of diamond is higher than 2000 W m^{-1} K^{-1}, which is even much higher than metals. Meanwhile, the coefficient of thermal expansion of diamond is just 1.2 ppm K^{-1}. These properties are very suitable for application in thermal management. As a result, although the cost of synthesis of diamonds is still high, many researchers tend to use it as thermal conductive filler no matter in metal, ceramic or polymer composites.[169-173]

Polymers are different from other carbon materials. The thermal conductivity of bulk polymer is low. So generally, polymers are mostly used as a matrix of composites instead of fillers. However, by stretching polymer chains or introducing a liquid crystal structure, polymer with high thermal conductivity is realizable. As an organic thermal conductive filler, the polymer is the only choice when constructing organic thermal

conductive composites.[174-175]

1.4.2.4 Hybrid fillers and special structures

Considering the development of materials with high intrinsic thermal conductivity is challenging and slow, constructing hybrid filler or special structure with existing material are another two efficient and practical methods to break the up limit of thermal conductivity.

The hybrid effect of thermal conductive fillers, which can endow the composites with properties of different fillers, is often applied to construct thermal conductive composites.[176] The hybrid of fillers brings many advantages. For example, modifying the interface between fillers and the matrix can influence the mechanical properties[177-178] or compromise the thermal resistance[179]. Besides, hybrid fillers can also be used to construct special structures by which heat can be transported more efficiently.[135, 180]

Constructing unique structures by hybridizing the metal particles with other materials is an effective method of adjusting the property of the final composite. A substantial amount of work in this field was done according to this strategy. By coating SiO_2 on Ag, dielectric constant at 1MHz, the dielectric loss of PI composite with 50% Ag@SiO_2 are 11.77 and 0.015 when thermal conductivity reached 7.88 W m^{-1} K^{-1}.[181] According to the author, the high thermal conductivity was inherited majorly from the metal Ag as figure 1.14(e) shows.

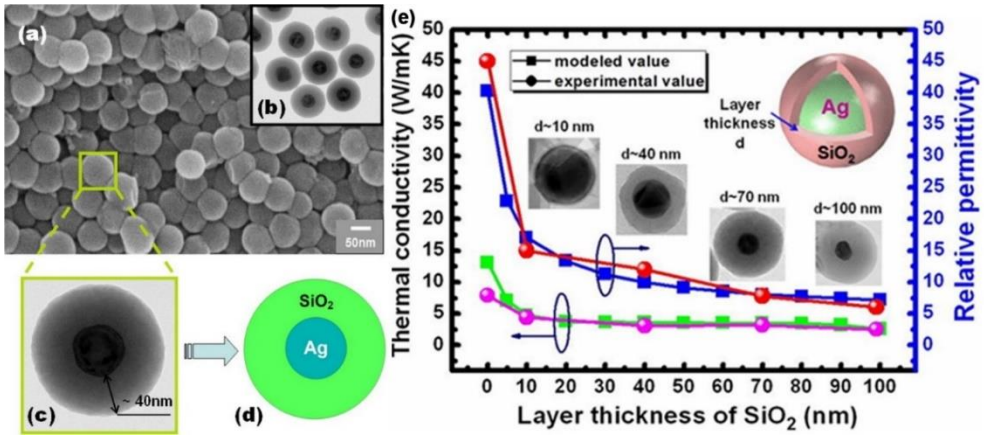

Figure 1.14. Core shell structure and thermal property of the composite. (a) SEM micrographs, (b) TEM micrographs, (c) partial enlarged drawing, and (d) a single nanoparticle schematic of core-shell Ag@SiO2 nanoparticles. (e) The thermal conductivity of composite versus thickness of SiO_2 [181]

1.4.3 Methods constructing the thermal conductive path

Besides the heat transport ability of filler, methods used to fabricate the composite significantly impact the thermal conductivity of resulted composites, particularly when anisotropic fillers are used. Here the development of different common methods which were often used to construct high thermal conductive composite was summarized briefly. Generally, these methods do not have their own exclusive application scenarios, but the choice of method should be carefully made to achieve the best possible performance of the final material.

1.4.3.1 Mixing

Mixing is the most used method in polymer processing. The agents and fillers are mixed with the precursor or monomer and initiator before

solidification. With respect to the construction of thermal conductive composites, this is also one of the easiest methods.[150, 182-183] This method is suitable for isotropic fillers where it is not necessary to consider the influence of alignment.

1.4.3.2 Hot press

The hot press is a traditional polymer processing method widely used in the vulcanization of rubbers. Constructing a thermal conductive path by hot pressing the metal coated polymer particles is a creative method. As introduced, when the thermal conductive fillers touch each other to form a continuous thermal conductive path, the thermal conductivity of the composite would reach a threshold value. Since the polymer particles were coated by a metal layer during the hot press process, the special structure makes sure a good connection between metals and the forming of a continuous network, as figure 1.15 shows. [184-186] This method is considered creative because of the new perspective on the relationship between filler and matrix.

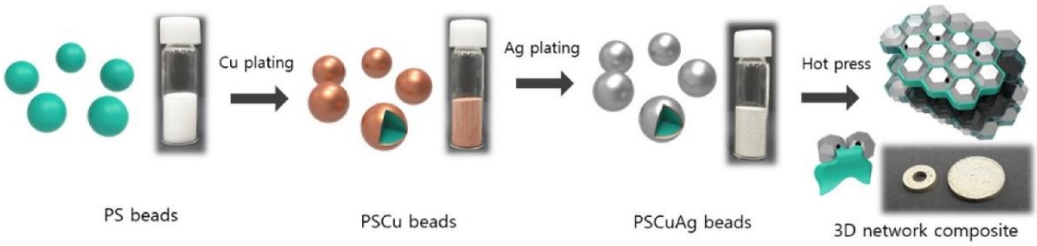

Figure 1.15. An example schematic illustration of the fabrication process of metal-coated polymer beads and their 3D metal shell network composites [185]

Similar with metal, hot press is also applicable on ceramics and carbon material composite.[135, 187]

1.4.3.3 Freezing casting

Freezing casting is a novel method of constructing aerogel. The general strategy is that when freezing the aqueous solution of fillers and matrix in a specific direction, ice would grow from the freezing area to the opposite. Relying on the growth of ice, fillers would be aligned along the ice grow direction. Meanwhile, with the decrease in temperature, the solubility of the matrix in water goes down. The precipitated matrix bestows mechanical property to aerogel in case of the breakdown of the skeleton. Finally, remove ice under vacuum by sublimation.[188-189]

The application of freezing casting is common in constructing thermal conductive composite with anisotropic thermal conductive fillers.[161, 190-191] Different freezing casting model has been developed.[192-197] Besides, some special structures can be achieved by designing the freezing cast model.[198-200] For example, Inspired by the nacre, a bidirectional freezing method was developed and applied to constructing thermal conductive material. Thermal conductive and insulating composite with 6.07 W m^{-1} K^{-1} thermal conductivity at 15 vol% BNNS loading was achieved as figure1.16 shows[201-202]

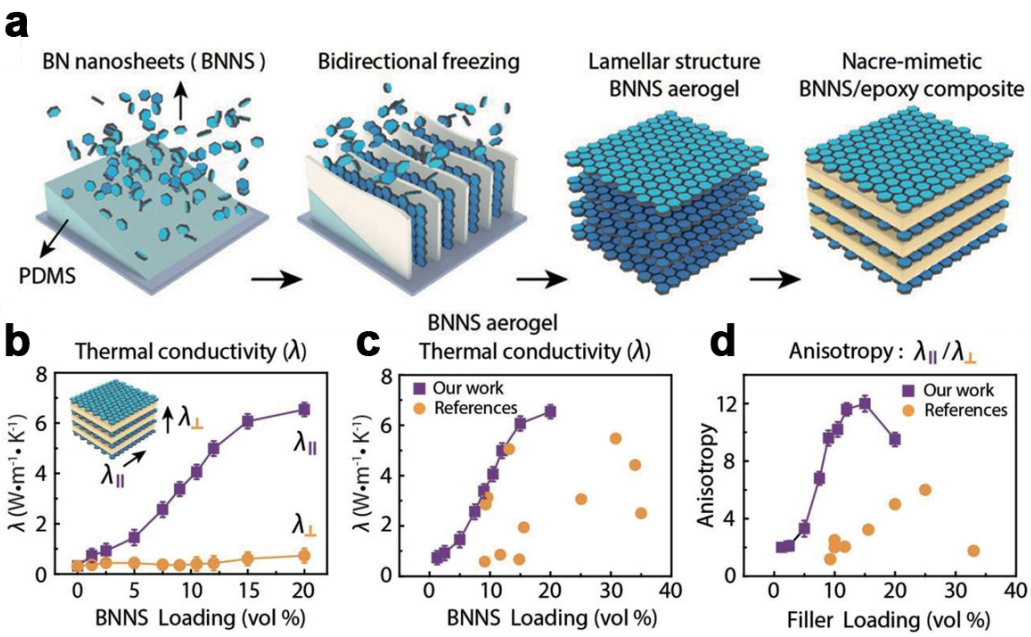

Figure 1.16. Fabrication and characterization of the boron nitride nanosheets (BNNS)/epoxy composite. (a)Schematic presenting the bidirectional freezing cast method fabricating BNNS aerogel. (b)The thermal conductivity of thermal conductivity on in-plane and through-plane direction. (c,d) Thermal conductivity and anisotropy comparation of the BNNS composite with other thermal conductive composites. [201]

1.4.3.4 Filtration

Filtration is an important method of aligning 2D material. Take aqueous solution as an example. To apply this method, researchers need to choose soluble polymer such as cellulose as a matrix. Filtrating the polymer solution is needed because of the small volume of water molecular. Water can go through the gauze while cellulose long chain blocked by the gauze and acts as a matrix to hold fillers. Since the flow of water is directional, 2D filters tend to align perpendicular to the direction forming a film.

With respect to thermal conductive composite, this method is suitable to

boron nitride and graphene specially.[135, 203-205]. For example, Lulu et. al. built up a cross linked 2D hexagonal BNNS by applicating vacuum filtration and self-assembling, as figure 1.17 shows.[205] The reported thermal conductivity in in-plane and through-plane directions are 14.21 W m^{-1} K^{-1} and 7.29 W^{-1} m K^{-1}, respectively.

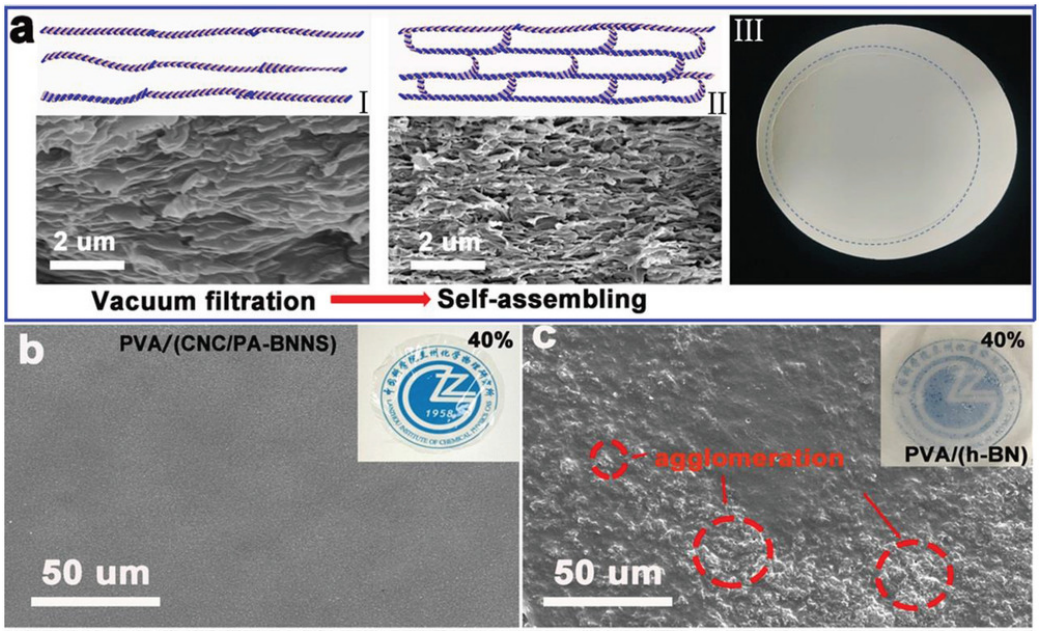

Figure 1.17. Morphology and structure characterization of the boron nitride sample. (a) Schematic diagram and corresponding SEM image of CNC/ PA-BNNS after filtration and self-assembling and a photograph of the sample (b) FESEM images of CNC/ PA-BNNs obtained. The illustration shows a comparison of the one-month dispersion of CNC/ PA-BNNS and BNNS in PVA. (c) TEM images of CNC/ PA-BNNS obtained. [205]

Another representative example should be mentioned. Yapeng et al. developed a pea-pod-like structure using graphene and Al_2O_3 by filtrating the fillers. Al_2O_3 working as scaffold seems like pea enfolded by graphene pod. Furthermore, soft graphene as a thermal conductive network promotes thermal conductivity. Unlike others, this structure is free-standing, so epoxy, as a matrix, is infiltrated after the thermal network is constructed. The final thermal conductivity reaches 33.4 W m^{-1} K^{-1}.

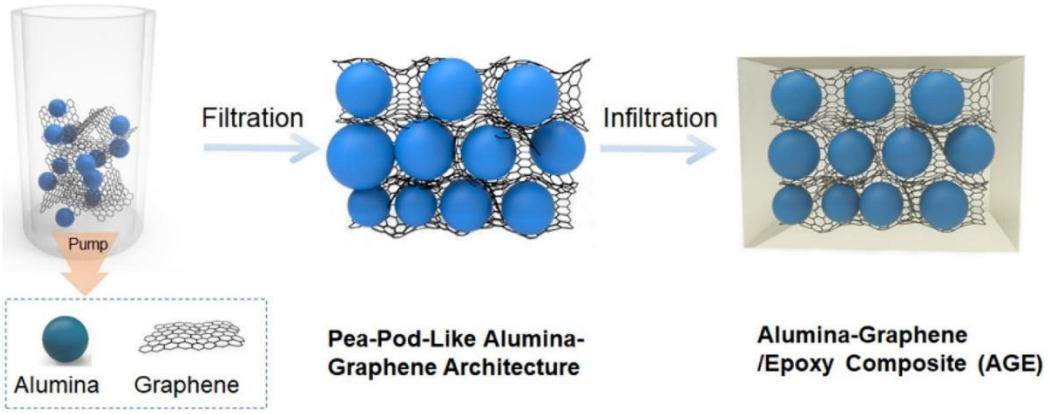

Figure 1.18 Construction of Alumia-Graphene/epoxy composite

1.4.3.5 Stretching

It is worth pointing out that stretching composite is also an effective method to align filler more than polymer chains. The effectiveness has been proved by applying the method to boron nitride.[206] By stretching PE/BNNP, as shown in figure 1.19, the thermal conductivity of the final composite can be promoted to 106 W m^{-1} K^{-1} at 15 wt% BNNC. However, this excellent achievement seems to have been ignored. Up to now, the article was just cited 8 times.

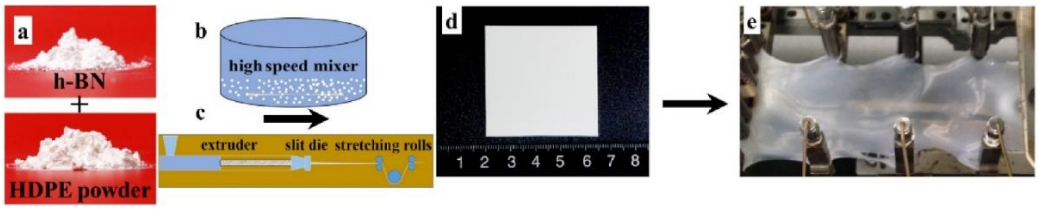

Figure 1.19. Preparation of PE/BNNP composite film (a) raw materials, (b) raw powers were mixed using high speed mixture, (c) mixed powers were extruded/pelletized using a single screw extruder, (d) as-extruded PE/BNNP firm made from pellets, (e) PE/BNNP nanocomposite film undergoing uniaxial stretching. [206]

1.4.4 Development of pitch-based carbon fiber and related thermal conductive composites

Carbon fiber was made by Edison for the first time in the 19th century as incandescent lamps. Otani proposed the approach to isotropic pitch-based carbon fibers. Carbon fiber can be grouped into pitch-based carbon fibers and PAN-based carbon fiber. As introduced, pitch-based CF has better thermal conductivity than PAN-based CF. As a high thermal conductive material pitch-based, CF began to attract attention since the 1960s. OTania first reported the synthesis approach to pitch-based carbon fibers with polyvinyl chloride as a precursor in 1965.[207] In the same year, Brooks and Taylor observed the nematic liquid crystal structure of mesophase carbon fiber, which melts at a temperature lower than the decomposition temperature.[208-209] From then on, researchers devoted more to this field.[210-212] Since then, pitch based carbon can be separated into isotropic pitch-based carbon fiber (IPCF) and mesophase pitch-based carbon fiber (MPCF). Compared with IPCF, MPCF had higher molecular weight, softening point, carbon aromaticity and degree of crystallinity.[213-216]

At that age, the most important application of CF was on constructing enhanced composites, so much work focused on synthesizing CF with higher modulus and strength. Union Carbide developed the strength and modulus of MPCF to 1960~2254 MPa and 519~823 GPa respectively in 1972 and started scale production in 1982. Until 1993, the production of CF was majorly concentrated in Japan and the United States when the highest strength and modulus record of pitch-based CF were 2940~3920 MPa and 245~882 GPa.[217] In different CFs, because of the abundant graphite structures, MPCF have a higher tensile strength and unique

modulus than IPCF.[212, 215, 218-219]

Because the waste heat problem was not urgent at that age and the potential as thermal management material was not found, CF was not applied to thermal management immediately. The study on thermal conductivity of CF composite was reported in 1979, and then thermal conductivities of different CFs were compared as composite filler.[220-221] After 1980, the potential of pitch-based CF as thermal conductive material was noted gradually; meanwhile, researchers started to make an effort to develop the thermal conductivity of CF.[222]

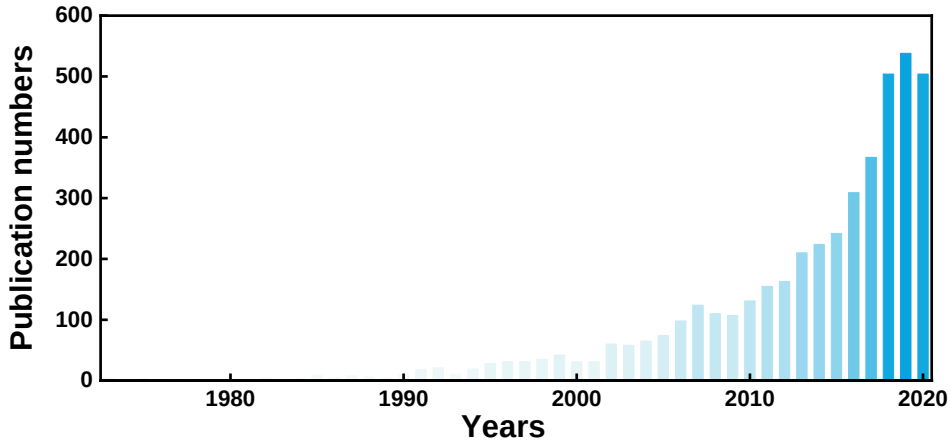

Figure 1.20. The publication number in different years

It was in the 21th century that the value of CF as thermal conductive filler was recognized, as figure 1.20 shows. Vary influences on the thermal conductivity of CF were studied during this period. The molecular orientation of pitch which is the precursor of MPCF can be important to the crystal structure of the product and finally influence the thermal conductivity of CF.[209, 223-224] Then, the mechanism of CF's high thermal conductivity was studied. The thermal conductivity of CF is affected by the crystal structure heavily. [225] PAN-based CF have particles of graphite crystal, while pitch-based CF has a macrostructure of graphite which

expand along the axial direction of CF. Phonon transport in graphite zoon is efficiently, so pitch-based CF has a thermal conductive path through the fiber inducing the higher thermal conductivity of pitch-based CF. On the contrary, the phonon transport in PAN-based CF is trapped in the graphite particles and blocked by the amorphous carbon between them. The different structures of the two kinds of CF can be checked in figure 1.21. For the same reason, With the size increase of graphite crystal, thermal conductivity increase.

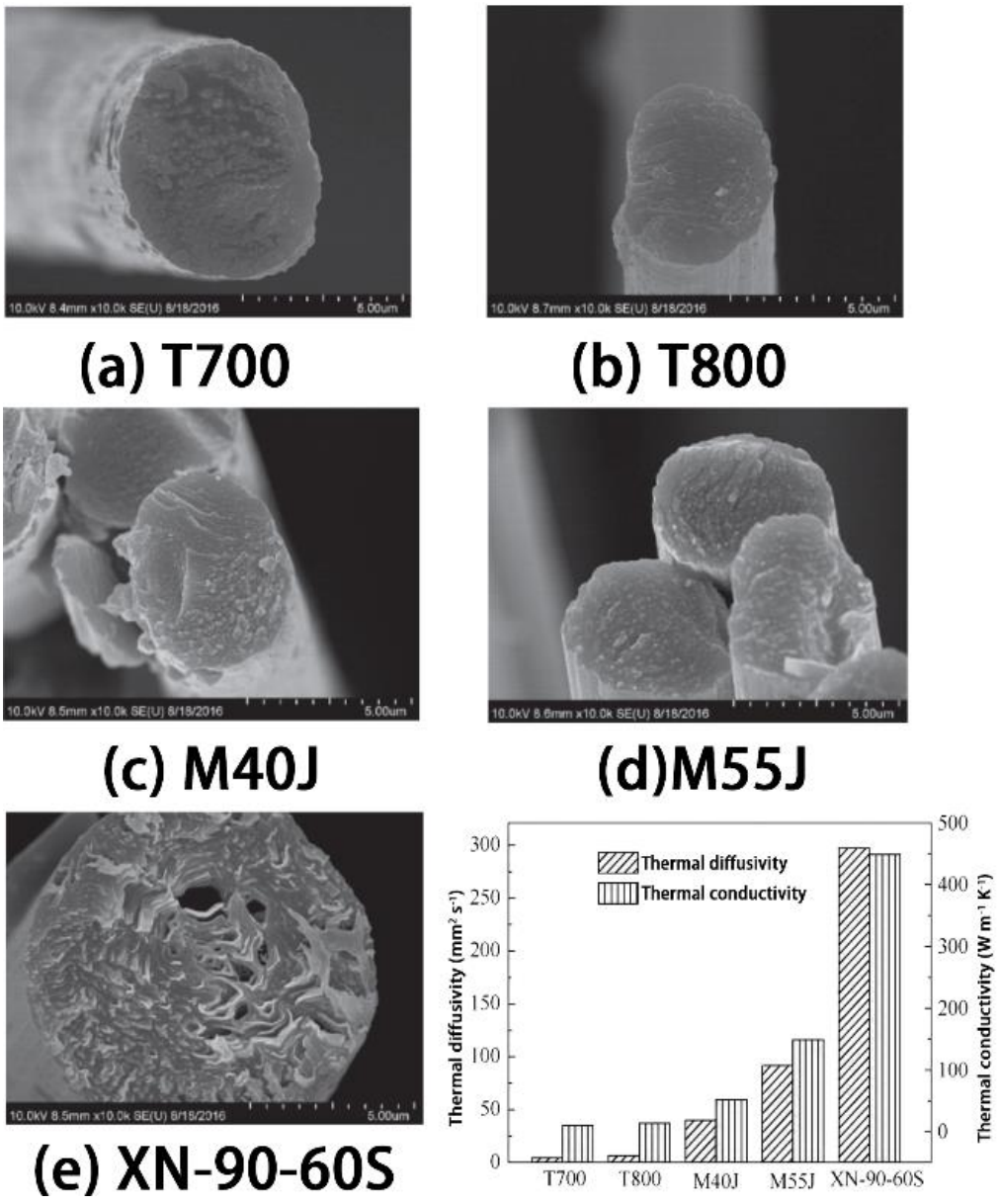

Figure 1.21. Structure of different CF and corresponding thermal conductivities. [225]

Nowadays, more researchers are attracted to the intrinsic thermal conductivity of CF. Different methods, including annealing and doping different elements, were developed.[226-229]. The most influential CF companies, Mitsubishi, NGF and Cytec Industries Inc, and some of their representative pitch-based CF product were listed herein in table 1.6.

Table 1.6. Three influential companies and their product

Company	Grade	Modulus (GPa)	Strength (MPa)	Thermal conductivity (W m-1 K-1)
Cytec Industries Inc	p-100s	760	210	520
	p-120	830	240	640
	p-120s	830	2240	640
	k-800	896	2900	800
	k1100	965	3100	1000
NGF	YSH-70A	720	36330	250
	YS-80A	785	3630	320
	YS-90A	880	3530	500
	YS-95A	920	3530	600
	XN-80	780	3430	320
	XN-90	860	3430	500
	XN-100			900
Mitsubishi	K1392U	760	3700	210
	K13916	760	3200	200
	K63A12	790	2600	220
	K13B2U	830	3800	260
	K13C2U	900	3800	620
	K13C6U	900	3600	580
	K13D2U	935	3700	800

1.5 Aims and objectives

Thus far, we have obtained a picture of the importance of thermal conductive materials, the requirement for thermal packaging materials

and the frontiers of the field. Meanwhile, the outstanding thermal properties and the anisotropic thermal conductivity of carbon fiber were interpreted. To make full use of the thermal conductivity of CF, the arrangement of CF in a specific direction was supposed so that heat can be transported from edge to edge. There are some methods introduced in this chapter could be applied to the arrangement. Compared with others, the mechanical method has many advantages, including energy conservation, safety, and non-limitation of filler concentration. In addition, as a traditional method, the mechanical method has incomparable stability.

This project aims to develop the thermal conductive composite, especially as the packaging or thermal interface materials, based on CF with a mechanical method and to hunt the possible solutions to the practical problems encountered in the electronic application. The most important indicator is thermal conductivity. Because of the anisotropies of carbon fiber and the application requirement, the project focuses on alignment of carbon fiber to the through plane direction of samples with a view to transporting heat from one side to the other. Such a simple and universal method was developed to fabricate material with thermal conductivity comparable with the samples made from other complex methods including ice template, electrical field and so on. And finally, we achieved the alignment of CF in composite and the sample we got possess thermal conductivity higher than 100 W m^{-1} K^{-1}. This value is comparable with metals and much higher than that of general carbon fiber composites. Or we can endow our samples with other functions like phase changing, to manage the temperature of equipment. A brief outline of the thesis is given below.

1.6 Thesis Outline

Chapter 1 gives a brief introduction to the field of thermal management material, including the theories explaining heat transport, methods constructing thermal conductive composite and the intrinsic properties of general thermal conductive fillers. Specially, it introduced the development of pitch-based carbon fiber which is a kind of promising thermal conductive filler. In this chapter, the strategy used in the thesis to enhance the thermal conductivity of composites on specific direction was identified. Furthermore, the chapter emphasizes the need for developing thermal management materials.

In chapter 2, the test methods are introduced. The equipment, manufacturing, and model of methods, including identification methods, thermal conductivity measurement and the structure analysis methods used in the thesis are given in the chapter. In addition, the theory of how to calculate the thermal conductivity of composites is also given in the chapter. Furthermore, the chapter also includes the most important filler used in the thesis, carbon fiber, and some common chemicals used. The morphology and the crystal structure of carbon fiber were studied. Meanwhile, the chemical of the matrix and raw material used to synthesize the matrix were identified.

In the subsequent 4 chapters, different strategies were applied to align the carbon fiber. In Chapters 3 and 4, we applied pressure on thermal conductive fillers to achieve the alignment in a plane. In Chapter 3, carbon fiber is used as thermal conductive fillers. Because of the mechanical field applied on it, carbon fibers tend to align in a plane perpendicular to the pressure direction. On the other hand, the

overlapping of carbon fibers promotes the construction of thermal path. Although a high thermal conductivity can be achieved by this method, it is not an efficient technique for one-dimensional filler.

Highlights

- Aligning carbon fiber to preparing high through-plane thermal conductive composite
- Using mechanical method to construct thermal conductive path
- Research about the relationship between thermal conductivity and the alignment of filler
- Simple and low-cost method fabricating thermal management material

Chapter 4 is an extension of the first work. Similar with the previous chapter, we studied the alignment of filler under compression. Graphite, a two-dimensional filler, was introduced to replace carbon fiber as a thermal conductive filler. Here the carbon fiber serves to fill gaps and flatten the surface of the sample. The synergistic effect of graphite and carbon fiber, which can efficiently enhance the thermal transport between two graphite is discussed in detail in the chapter.

Highlights

- Thermal interface material with low thermal resistance and high thermal conductivity
- The synergistic effect between carbon fiber and graphite as thermal conductive fillers
- Enhancing heat exchange between filler and matrix by strengthening the interaction
- Low-cost and practical method producing TIM with high thermal conductivity

After discussing the influence of pressure on the alignment and the resulted thermal conductivity difference, in chapter 5, the stress was studied. Compared with pressure, stress can achieve the alignment of one-dimensional fillers and, therefore, realize a higher thermal conductivity. However, how to apply stress on every specific carbon fiber is a challenge all the time. In this chapter, a medium, the paste, was introduced to hold the milled carbon fiber and assist them to align along the stress direction. Then the past was graphitized at high temperature to form a carbon network as a thermal transport path. The resulted thermal conductivity of the composite is about 110 W m^{-1} K^{-1}, which is comparable with metal. Meanwhile, the density is much lower than metal.

Highlights:

- Calculating the thermal conductivity of different carbon crystal styles
- Carbon fiber composite possessing metal-level thermal conductivity, suitable thermal expansion coefficient and low density
- Aligning 1D micro filler on single specific direction with a mechanical method
- Mathematic mold describing the alignment of 1D micro filler mixed in medium during stretching

In chapter 6, latent heat is bestowed to the thermal conductive composite by introducing phase change materials (PCM). With the help of phase change material, the composites can handle the over-loading of electronic equipment. In this work, a soft organic network, polyacrylic acid (PAA), is used to limit the leakage of phase change material at high temperatures so that the melted phase change material still displays elasticity without leakage. The soft thermal conductive composite can be

applied in a variety of scenarios. In this work, the material is used as thermal interface material to evaluate the heat dissipation ability by comparing the temperature with and without it.

Highlight:

- Fabrication of shape-stable thermal conductive phase change material
- Aligning carbon fibers with the assistance of organic crystal
- Investigating the influence of PAA on PEG crystal structure
- Enhancing the mechanical strength of phase change material

Finally, chapter 7 summarizes the thesis and highlight the contribution into constructing thermal management materials. The chapter ends by highlighting potential extensions and future research interests.

Chapter 2. Chemicals and Tests

2.1 Synopsis

Considering the practicality of the composites, besides thermal conductivity, various properties need to be evaluated, including mechanical property, thermal stability and so on. Meanwhile, to illustrate the relationship between properties and structures, it is necessary to observe the morphology and identify the components. To evaluate the properties and analyze the samples, different test methods were introduced.

Considering that the work of this thesis is around carbon fiber composite, as the most used material during the program, the carbon fiber used here was characterized carefully in this chapter to avoid repeating in the following chapters. In addition, the most used matrix including epoxy, polyacrylic acid and polydimethylsiloxane were also identified.

2.2 Test methods

2.2.1 Identification of chemicals

To characterize the molecular structure of the samples, nuclear magnetic resonance (NMR) spectra and infrared spectra (IR) were obtained using Bruker NMR (Bruker AVANCE III 400 MHz, Germany) and Fourier transform infrared spectroscopy (Thermo Nicolet 6700, U.S.A.), respectively.

2.2.2 Thermal conductivity and thermal resistance

Thermal conductivity is the kernel parameter of thermal conductive material. Here *ASTM E 1461-13: standard test method for thermal diffusivity of solids by the flash method* was introduced to test thermal conductivity of samples. Specifically, the thermal conductivity was calculated according to the follow formula,

$$K = \alpha \times Cp \times \rho, \quad (2.1)$$

Where α, Cp and ρ represent thermal diffusivity ($mm^2\ s^{-1}$), specific heat ($J\ g^{-1}\ K^{-1}$), and density ($g\ cm^{-3}$), respectively. Thermal diffusivity and specific heat were measured by laser flash apparatus (LFA; NETZSCH LFA 467, Germany), and differential scanning calorimetry (DSC; NETZSCH DSC 214, Germany) and the density was obtained according to the Archimedean principle with a balance.

Some statements should be made here regarding the form of the thermal conductivity. In 3D space, since the temperature difference and the heat flux are vector. Theoretically, the thermal conductivity should be expressed as a tensor, so that that the vectors can be transformed to each other by the tensor. However, it is not easy to measure all components of the thermal conductivity tensor. Meanwhile, in the application of the material, we lay more emphasis on the thermal conductivity on through plane direction. Considering these limitations, in this thesis, when we talk about thermal conductivity, it actually represents the through-plane direction component of the thermal conductivity tensor.

The test condition of specific heat is raising the temperature of samples from 0 to 125 ^oC with the step of 10 ^oC/min in N_2 atmosphere, during which period the heat flux of samples was monitored and compared with

the standard sample. Only the data between 25 and 100 ^{o}C are used.

Another method presenting the heat pass ability of composite is infrared images. Thermal conductive materials are heated on one surface and the temperature of the opposite surface is recorded in infrared images. According to the definition of thermal conductivity, the higher the temperature is, the higher this value is.

To measure the thermal resistance under different pressure and at different temperatures, thermal resistance and conductivity measurement apparatus (TRCMA; Longwin Science & Technology Corporation, LW-9389, Taiwan) was applied.

2.2.3 Thermal stability and latent heat of phase change

Thermal stability is sometimes important when we discuss the applicability of materials, including thermal decomposition and coefficient of thermal expansion, which was evaluated using Thermo Gravimetric Analysis (TGA, Diamond TG/DTA, US) and thermal dilatometer (DMA, Netzsch, DIL402C, Germany). The test condition is of TGA is raising the temperature of samples from 25 to 800 ^{o}C with the step of 10 ^{o}C/min in N_2 atmosphere, during which period the weight of samples were monitored.

Latent heat is used to evaluate the ability of phase change material on stabilize the temperature. This value is measured by differential scanning calorimetry (DSC; NETZSCH DSC 214, Germany). The test condition is raising the temperature of samples from 25 to 100 ^{o}C with the step of 10 ^{o}C/min in N_2 atmosphere, during which period the heat flux of samples

were monitored and compared with the controlled sample.

2.2.4 Investigation of structure

To investigate the dispersion of fillers in composites or the heat path going through composite, SEM and micro-CT were introduced. The tests were performed using scanning electron microscopy (SEM; FEI Quanta FEG 250, USA) and micro-computed tomography (micro-CT; ZEISS Xradia 510 Versa, Germany) SEM can observe the cross section while micro-CT can display the 3D structure of the composite.

Besides the fillers, the surface structure of composites was analyzed because of its importance to thermal management material especially to TIM. To compare the roughness of different samples, a 3D profilometer (UP-Lambda, USA) was used.

To characterize the crystal structure, X-ray diffraction (XRD) patterns and Raman spectra were obtained using a Bruker D8 Advanced diffractometer (Germany) and a Renishaw Reflex Raman System (UK), respectively. When analyze the bonding structure transform, X-ray photoelectron spectra (XPS, AXIS SUPRA, Kratos, UK) is used.

2.3 Characterization of CFs

Carbon fiber provided by Fujian United New Material Technology Co., Ltd. (Fujian, China) was used as a thermal conductive filler. It is a kind of pitch-based carbon fiber whose thermal conductivity is about 900 W m^{-1} K^{-1}, according to report. The Structure and geometry of the fiber were studied carefully. The SEM image of carbon fiber presented in figure 2.1(a) and the statistic of fiber length shown in figure 3.1(b) was

introduced to characterize the geometry on the order of micrometer. According to statistics, the average length of the carbon fiber is about 234 um.

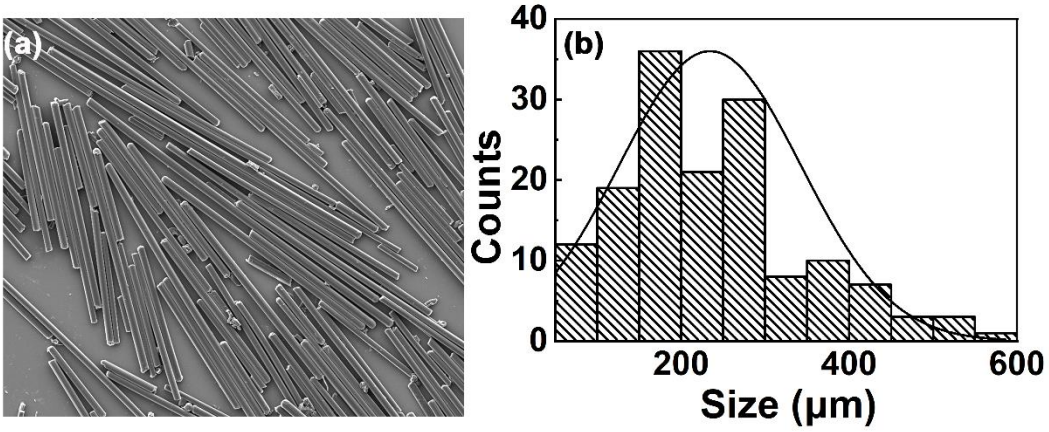

Figure 2.1. Morphology of CFs. (a)SEM image and (b)the statistic of CFs length.

The TEM is a method to analyze structure on a smaller scale. We can observe the crystals of carbon fibers intuitively. Here the TEM image and electron diffraction patterns shown in figure 2.2 is observed using TEM (Talos F200x, ThemoFisher, USA).

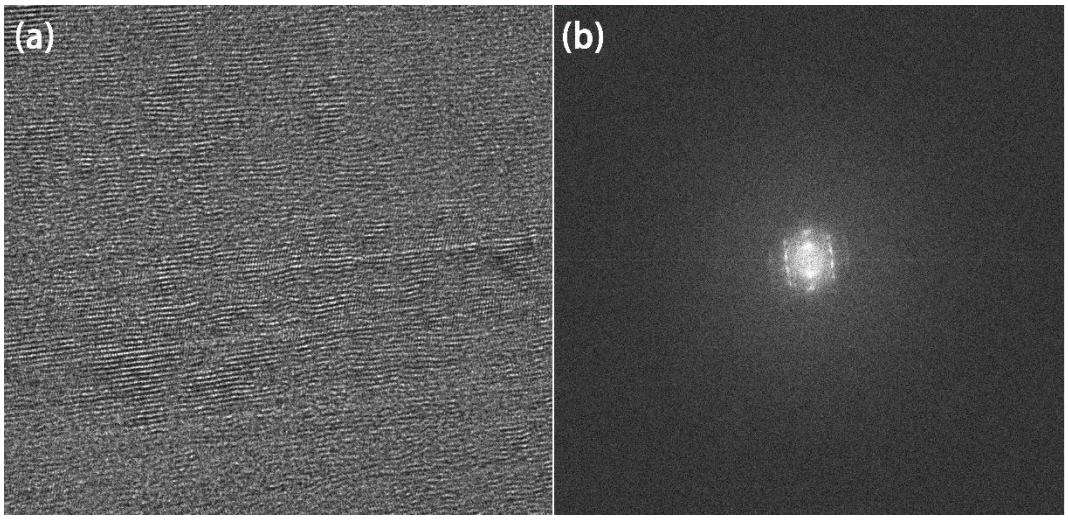

Figure 2.2. The TEM image (a) and electron diffraction patterns (b) of CFs.

Besides TEM, the atomic structure of carbon fiber was studied statistically by FTIR, XRD and Raman. As carbon material, the analysis of carbon fiber structure utilized the analysis of other carbon materials,

including graphene and graphite. The FTIR spectrum, XRD spectrum and Raman spectrum of CF was showed in figure 2.2.

FTIR demonstrates the molecular structure by a specific frequency of the asymmetric bond vibration. Here, FTIR was obtained using Fourier transform infrared spectroscopy (Thermo Nicolet 6700, U.S.A.). From the FTIR spectrum of CFs, as shown in figure 2.3(a), the O-H, C-H, C=O and C-O-C can be identified.[230] These asymmetric bond vibrations indicate the existence of functional organic groups. The defect caused by the inorganization of carbon atoms can be observed from Raman, which is widely used in analyzing symmetric vibrations. For example, in the field of carbon material, Raman is used to identify diamond (1332 cm^{-1}) and graphite (1350 and 1580-1600 cm^{-1}).[231-232] Here, Raman spectrum was tested using Renishaw8 Reflex Raman System. As carbon materials, CF, graphene, and graphite, which consist of sp^2 carbon share similar Raman spectrum and analysis method. 1350 and 1580-1600 cm^{-1} is labeled as D band and G band respectively as shown in figure 2.3(b). The intensity ratio between D band and G band, I_D/I_G is a characterization parameter for the quality of carbon material, which is related to the defect in graphene structure. The higher the value is, the worse the quality is. [232-233]

X-ray diffraction (XRD) is a test method for characterizing the crystal structure. Here, XRD patterns were obtained on a Bruker D8 Advanced diffractometer from a 2θ value of 5° to 80° and displaced in figure 2.3(c). From XRD spectrum, the leptokurtic band at 26.4° and 54.5° are assigned to (002) and (004) graphene. According to Bragg formula, the interlayer spacings d002 and d004 are 3.38 and 1.68 Å, respectively.

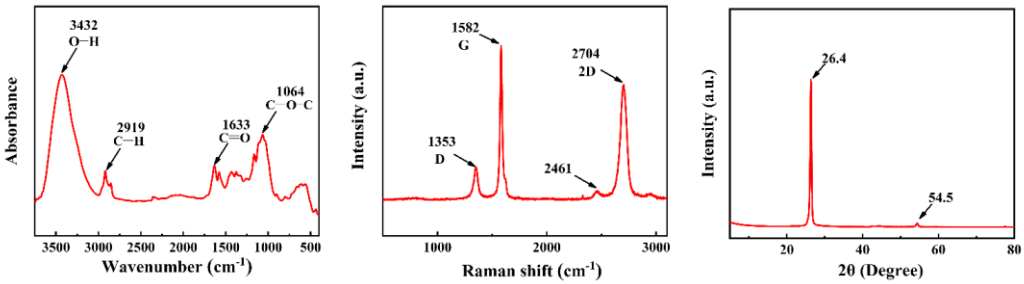

Figure 2.3. The characteristic of CFs. (a)FTIR spectrum of CFs. (b)Raman spectrum of CFs. (c) XRD spectrum of CFs

2.4 Matrix

Besides CFs used as thermal conductive filler, polymer matrix plays an important role in constructing composite. These polymers with different properties are applied according to the requirement of applications. In this thesis, epoxy, PDMS, PAA and polyethylene glycol (PEG) were introduced as matrix, among which epoxy, PDMS and PAA were purchased as monomers and initiators or catalysts, PEG is purchased as a polymer. The information is listed here.

The epoxy resin and curing agent methylhexahydrophthalic anhydride (MHHPA) were purchased from Dow Chemical Company and Zhejiang Alpharm Chemical Technology Co. Ltd., respectively. The curing accelerator Neodymium(III) acetylacetonate trihydrate (Nd(III)acac) was obtained from Sigma-Aldrich Corporation.

Polymethylhydrosiloxane was purchased from Shuangjixing Science and Technology Co., Ltd. (Tianjin, China). Platinum (0)-1,3-divinyl-1,1,3,3-tetramethyldisiloxane complex solution (1000 cP) that is used as catalyst was purchased from Zhongzhan Silicone Material Co., Ltd. (Guangdong, China). Vinyl terminated polydimethylsiloxane was purchased from J&K Scientific (Beijing, China). Coupling reagent (KH-570) is purchased from

Nanjing Chuanshi Chemical Co., Ltd. (Jiangsu, China). Analytical reagent grade ethanol absolute and glacial acetic acid were purchased from Sinopharm Chemical Reagent Co., Ltd. (China).

The PEG, whose average molecular weight equals 2000 and analytical reagent ammonium persulfate were purchased from China National Pharmaceutical Group Co., Ltd. (Shanghai, China). Acrylic acid and N,N′-methylenebis (acrylamide) (BAC) were purchased from Shanghai Aladdin Biochemical Technology Co., Ltd (Shanghai, China).

Chapter 3. Stress Inducing Carbon Fiber Orientation Enhanced Thermal Conductivity of Epoxy Composites

3.1 Synopsis

Polymer composites that have high thermal conductivity have become one of the most promising solutions needed to satisfy the thermal management requirements for high-power electrical and electronic equipment. In this work, a strategy relying on aligning carbon fibers through the application of a stress field is proposed. Ultrahigh through-plane thermal conductive epoxy composites with carbon fiber networks have been prepared by in-situ solidification within an epoxy. The thermal conductivity of these epoxy composites reaches as high as 32.6 W m^{-1} K^{-1} at 46 weight percent (wt%) of carbon fibers, which is about 171 times that of the pure epoxy. The alignment condition for the carbon fibers for a carbon fiber composite in which stress has been applied and a blended carbon fiber composite are compared using micro compute tomography (micro-CT) and scanning electron microscopy (SEM). These epoxy composites display attractive thermal properties and provide a practical route to satisfy the thermal dissipation requirements raised by the development of modern electrical devices and systems.

3.2 Finite element analysis of composite with different filler alignment

In order to explain the influence of alignment on thermal conductivity of carbon fiber plate, finite element analysis was carried out. CFs in epoxy resin were represented by 20 continuous rods with length-width ratio of 10. Thin heaters with a volume power density of 100 W m^{-3} were installed at the bottom of the different composites to form a gradient heat flow in the direction along orientation of the carbon fibers. As shown in figure 3.1, the range of temperature gradient with CF rod spindle Angle presents a quasi-random distribution. Here, because we focus on the influence of alignment on directional thermal conductivity, the thermal resistance between matrix and CF was not introduced. Note that an Angle of 0 means that CF is aligned along the temperature gradient, and an Angle of 90^{o} means that CF is perpendicular to the temperature gradient. The top surface temperature of the simulated composite was fixed at room temperature (293.15K), and the two boundaries at left and right are adiabatic. All boundaries are non-periodic and fixed. The calculated temperature difference between the top and bottom surfaces at equilibrium was marked as shown in Figure 3.1. The thermal conductivity is defined as $K = Q / \nabla TS$. Here Q is the heater power, S is the model sectional area, and ∇T is the temperature gradient. When the input power and cross-sectional area are constant, the thermal conductivity is inversely proportional to the thermal gradient ∇T. When the Angle values are evenly distributed within the interval [0,90 degrees], the direction of the carbon fiber is completely random, resulting in tortuous paths, so the heat cannot quickly pass through the composite heat transfer due to the long path length relative to the length of the sample. Heat builds up in the sample, causing the temperature to rise. Because the temperature

of the cooling area is fixed, the end result is a large temperature difference. Conversely, as the Angle of the CFs relative to the temperature gradient becomes zero, or the CFs is perfectly aligned with the preferred direction of heat transfer, the thermal path is minimized, resulting in more efficient heat transfer. The temperature difference decreases from 37 to 21 K. Simulation results point out that aligning carbon fiber is an effective method to enhance heat conduction of carbon fiber composites. In order to realize the alignment in the experimental study, CFs were forced into a mold. The detailed description was given in next subchapter.

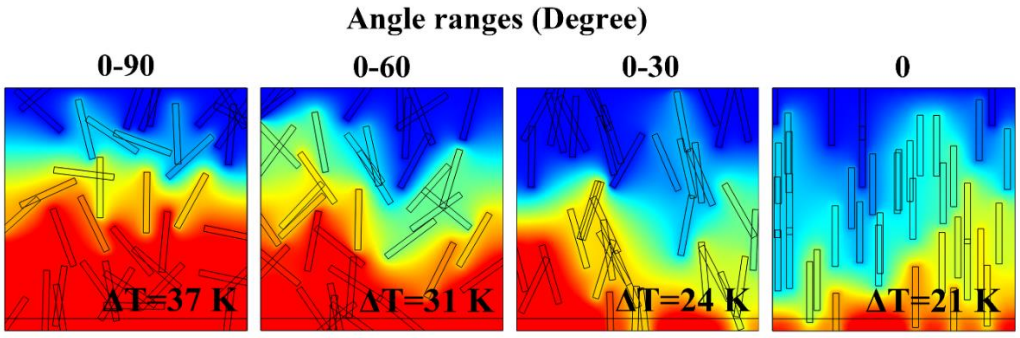

Figure 3.1. The temperature distribution of one-dimensional fillers distributed in epoxy resin under different arrangement conditions was calculated by finite element analysis. The top surface is fixed at 293.15 K and a 100 W m^{-3} heater is attached to the bottom of the block. The temperature difference between the top and bottom is marked to indicate the dependence of thermal conductivity on packing arrangement.

3.3 Preparation of epoxy composites

The ratio of epoxy resin, curing agent and accelerator was 100:95:0.5, and the deaerator was stirred. The mold as shown in figure 3.2(A) (its

photo can be found in figure 3.3), designed for storage of raw materials. Before the epoxy is injected, 3.5g of carbon fiber is pressed into the mold with a plug. The whole mold was placed in a vacuum oven at a fixed temperature of 70 ^{o}C to improve the flow performance of the epoxy resin. Air is pumped out of the mold through the hole to allow the epoxy to flow into the vacuum in the CF network. During this process, the liquid level can be monitored. additional epoxy was dropped in as air evacuated until the liquid level no longer decreases. The epoxy is cured in an oven with two temperature cycles. In the first cycle, the temperature was maintained at 135 ^{o}C for 2 hours to precure the epoxy resin. In the second cycle, the temperature was kept at 165 ^{o}C for 14 hours. The concentration of CFs varied between 30 and 46 wt%. These specimens made from pre-stressed carbon fiber epoxy composites, hereafter is referred to as s-CF/epoxy. On the other hand, epoxy, hardener and carbon fiber are mixed in equal proportions in a pot and are combined using a high-speed mixer. Curing method follows the same process as s-CF/epoxy resin. Carbon fiber epoxy composites were prepared by blending with the CF/epoxy obtained. In addition, in the preparation of CF/epoxy resin samples, once the concentration of CF exceeds 35 wt%, it is difficult to ensure the formation of a uniform mixture of raw materials. In this case, the epoxy resin is diluted with acetone to make the sample uniform. Because of these high concentrations of CF. The other step is to remove the acetone, which is achieved by curing the sample at 70 ^{o}C for 12 hours.

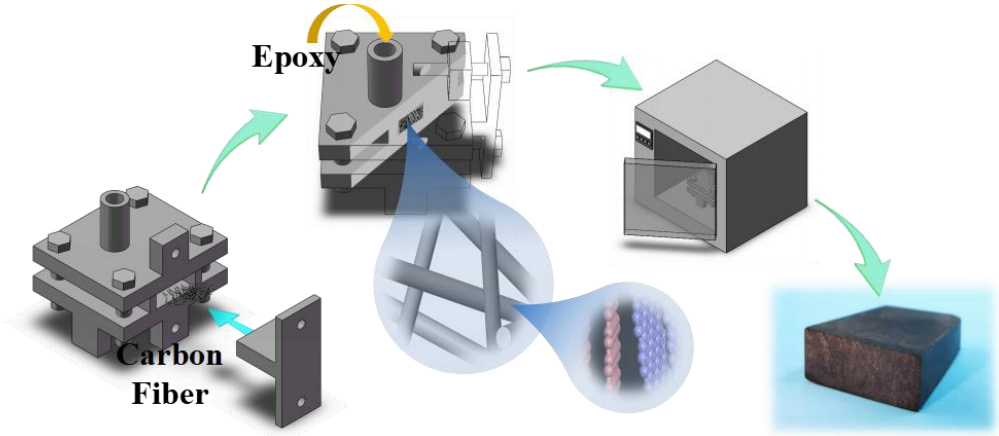

Figure 3.2. Schematic of aligning CFs under the stress field. The milled carbon fiber is compressed from a custom mold. The epoxy resin is then injected into a mold and cured at a specific temperature. A sample with aligned CFs is obtained, and its predicted microstructure is shown.

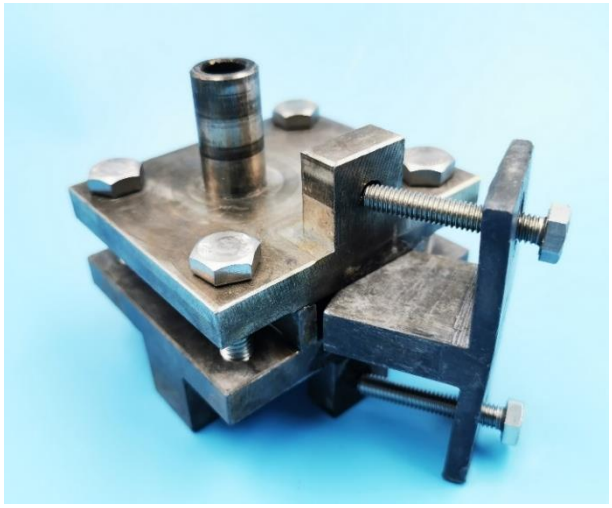

Figure 3.3. The mold used to orient CFs.

3.4 The micro structure of composite

To explain the orientation of the CFs, it was assumed as a bar whose one end was fix to the origin point of cartesian coordinate but reserved the rotation ability. The direction of CFs can be transformed by determining the distribution of the end of the fiber which is not fixed but located on a hemispherical surface as shown in figure 3.4 (a). In the image, angle

between the carbon fiber and the normal vector passing through the top surface of composite was labeled as A.

If rotation of CFs is completely random, the distribution of the endpoint on a finite area is the same, assumed as f here. The area of annulus at angle A can be expressed as

$$S = 2\pi \mathrm{L}^2 \sin A \ dA \tag{3.1}$$

where L is the length of CFs. Considering that the end of CF is located on a hemispherical surface as discussed,

$$1 = \int_0^{\frac{\pi}{2}} Sf \tag{3.2}$$

$$1 = \int_0^{\frac{\pi}{2}} 2\pi \mathrm{L}^2 \sin A \ f dA \tag{3.3}$$

$$f = \frac{1}{2\pi \mathrm{L}^2} \tag{3.4}$$

This formula indicates that the distribution of the endpoint on an annulus corresponding to a finite angle dA is

$$\mathrm{F(A)} = \sin A \, dA \tag{3.5}$$

In figure 3.4 (b), dA is set to 1°, and the relationship between the probability and Angle is given as a gray curve. The orientation distribution of CFs in s-CF/epoxy composite and CF/epoxy composite was analyzed according to their micro-CT scanning data and then plotted in the same figure. Compared with random distribution, s-CF/ epoxy samples have a higher probability of occurrence when a value is small and a lower probability when a value is large, as shown in figure 3.4(b). The statistics show that CF is aligned along the normal direction through the plane. On the contrary, CF/ epoxy resin samples have A lower probability at small A and A higher probability at large A, which may be caused by gravity. In support information, a video is displayed, with each frame parallel to the top portion. In the video, comparing two samples, we can see the

different arrangements between different samples. Figure 3.4(c, d) is also the spatial structure of carbon fibers dispersed in the two samples.

SEM images were recorded to analyze orientation of carbon fibers in two-dimensional (2D) space. The orientation statistics of carbon fibers were obtained by studying the cross-section morphology of carbon fibers. As shown in figure 3.4(e), in s-CF/epoxy, the fibers tend to be oriented along the direction of heat transfer, while in CF/epoxy, the fibers tend to disperse on the horizontal plane due to gravity. The results of SEM analysis confirmed the observed phenomenon by micro-CT measurement. In addition to the preferred orientation of the carbon fibers, the microstructure of the composites was illustrated by SEM. As shown in figure 3.4(g), few resins were found between CF of the s-CF/epoxy resin samples. In contrast, in the CF/ epoxy resin sample, it can be seen from figure 3.4(h) that there is always a resin between CF. Given that a force is applied to the carbon fibers before the epoxy is injected, it can be understood that a network is formed between the carbon fibers, allowing the applied force to be transmitted to the network. It is worth noting that the CF network also helps to improve heat transfer. In contrast, the CF in the control group is coated with epoxy, introducing additional thermal resistance between the CF's, thus further inhibiting thermal conductivity relative to the aligned CF network.

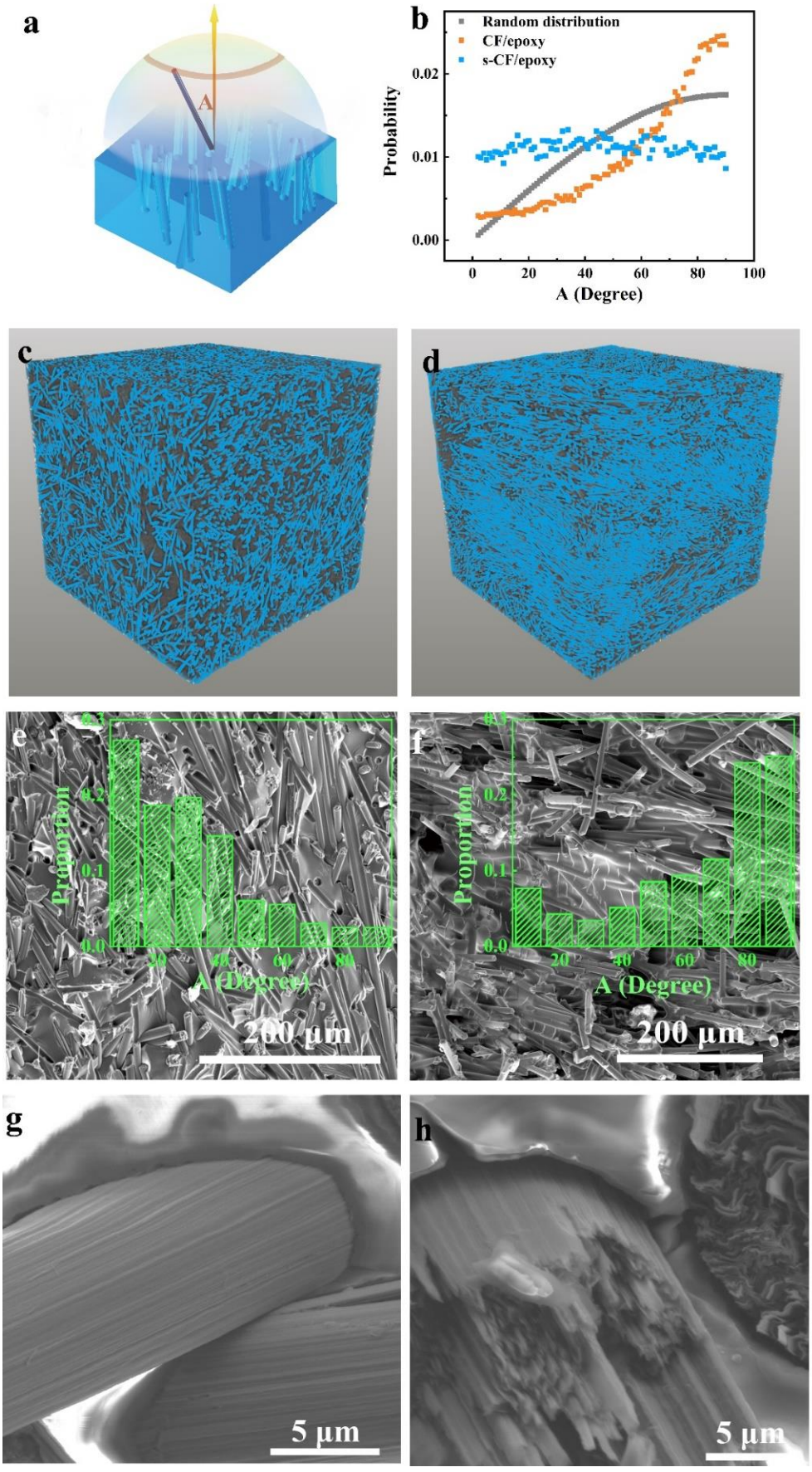
a
A
b
Random distribution
CF/epoxy
s-CF/epoxy
Probability
0.02
0.01
0.00
0
20
40
60
80
100
A (Degree)
c
d
e
Proportion
0.2
0.1
0.0
20
40
60
80
A (Degree)
200 μm
f
Proportion
0.2
0.1
0.0
20
40
60
80
A (Degree)
200 μm
g
5 μm
h
5 μm

Figure 3.4. The characteristic of CFs alignment. (a) Schematic of the angle between CFs, denoted A, and the normal vector to the through-plane. (b) The statistic of A in CF/epoxy (yellow dots) and s-CF/epoxy (blue dots) and theoretical value for a purely random distribution. (c,d) The micro-CT results of s-CF/epoxy(c) and CF/epoxy(d). (e,f) The SEM image of composites and statistic of A in s-CF/epoxy(e) and CF/epoxy(f). SEM statistic is based on the CF alignment on the 2D cross section, which is different from micro-CT based on that in 3D block (g,h) The SEM images showing the direct connection between CFs in s-CF/epoxy(g) and the epoxy separating the CFs in CF/epoxy(h).3.5 Relationship between thermal conductivity and structure

3.5 Thermal and mechanical property of composite

To evaluate the thermal conducting property of the resulted composites, *ASTM E 1461-13* was applied as Chapter 3 introduced. In figure 3.5 shows the relationship between thermal conductivity and CF content of the s-CF/epoxy and CF/epoxy samples. As reference, the result for pure epoxy is a thermal conductivity of 0.19 W m^{-1} K^{-1}. With the increase of CFs content, the CF/epoxy and s-CF/epoxy thermal conductivity improves to 4.7 and 32.6 W m^{-1} K^{-1}. The related original data used to plot the figure 3.5 were given in table 3.1.

Table 3.1. Concentration, thermal diffusivity, density, specific heat and calculated thermal conductivity of epoxy, CF/epoxy and s-CF/epoxy.

	Concentration (wt%)	**thermal diffusivity (mm^2 s^{-1})**	**Density (g cm^{-3})**	**specific heat (J g^{-1} K^{-1})**	**Thermal conductivity**

					(W m^{-1} K^{-1})
s-CF/epoxy	30.00	5.90	1.36	1.05	8.45
	33.00	7.17	1.38	1.03	10.17
	39.00	9.10	1.42	1.13	14.61
	49.00	20.53	1.48	1.06	32.12
CF/epoxy	30.00	1.80	1.40	1.12	2.81
	33.00	3.10	1.42	0.91	4.00
	39.00	2.57	1.43	0.98	3.60
	49.00	3.03	1.44	1.07	4.67
epoxy		0.13	1.23	1.20	0.19

According to our measurement, thermal conductivity is proportional to the loading of CFs and the different between s-CF /epoxy and the CF/epoxy also expands with the rise of loading of CFs. This behavior has been intensively investigated. Agari et al. proposed a mode[234] that specially describes the thermal conductivity of composites filled by 1D filler. Within the model, the apparent thermal conductivity is predicted by

$$\log k = VC_2 \log k_f + (1 - V) \log(C_1 k_p) \quad (3.6)$$

Where V represents the bulk concentration of the filler. C1 is a factor related to the crystallinity and grain size of the matrix. In this study, the substrate of both s-CF/epoxy resin and CF/ epoxy resin is the same epoxy resin, so C1 of the two samples should be equal or close. In the original literature, C2 was a general factor associated with the easy formation of conducting chains, but the physical significance of C2 may include other influences. Agari et al. 's model considered the effect of carbon fiber aspect ratio on C2, but did not consider the effect of linear shape. The parameters k_f and k_p are the thermal conductivity of the filler and the matrix respectively. In the model, k_f was strictly limited to 418 W m^{-1} K^{-1} (1 cal s^{-1} cm^{-1} K^{-1}).

However, with the continuous development of materials science, many new fillers with thermal conductivity much higher than this limit have been discovered, such as the carbon fiber used in this paper. In Agari et al. 's model, if k_f is less than 418 W m^{-1} K^{-1}, the possibility of forming a conductive chain is greater and C2 is smaller. However, the thermal conductivity of CF in this paper much higher than 418 W m^{-1} K^{-1}, so the negative sign introduced by $\log k_f$ disappears. As a result, C2 trends should be reversed, meaning that the more likely a conducting chain is to form, C2 should become larger. In this paper, the least square method was used to match the experimental data, and the C1 values of s-CF/epoxy and CF/epoxy composites were set as the same. According to our calculations, C1 is equal to 7.8. The apparent thermal conductivity calculated according to Agari et al. 's model is shown in figure 3.5. C2 extracted from the measured data of s-CF/epoxy resin and CF/epoxy resin were 6.8 and -0.7, respectively.

From the perspective of microstructure, there may be two reasons for the difference in the formation of conductive chain between s-CF/epoxy resin and CF/ epoxy resin. Firstly, under the action of external force, CFs tend to align along the normal direction of the through-plane. Because the axial thermal conductivity of CFs is approximately two orders of magnitude higher than the radial thermal conductivity, alignment makes the conduction chain more efficient in the heat transfer direction. Another possible reason is that CF can construct a frame in situ to transfer heat in s-CF/epoxy samples, whereas in CF/epoxy samples, epoxy coating outside of CF breaks the direct connection between individual CFs. In addition to SEM analysis based on the images shown in figure 3.4(e-h) as discussed, we also studied its mechanical properties to provide

support for the conclusion. The epoxy resin in the composite holds the carbon fibers together. Lack of epoxy resin between carbon fibers can cause changes in mechanical properties. Previous studies have reported the relationship between the damping term ($\tan\delta$) and the interface strength. [235-238] According to Ziegel and Romanov's analysis, this relationship can be expressed by the following formula:

$$\tan\delta_c = (1 - B\phi_F)\tan\delta_m \tag{3.7}$$

Among them, $\tan\delta_c$ and $\tan\delta_m$ are the damping terms of the composite material and the matrix, respectively, and ϕ_F is the volume fraction of the filler. B is a correction factor to compensate for the interface volume fraction due to the strong interfacial interaction of composites. The value of parameter B is positively correlated with the interface strength. The formula analysis shows that $\tan\delta_c$ decreases with the increase of interfacial strength. Figure 3.6 shows the DMA results of s-CF/epoxy, CF/epoxy and pure epoxy resins. Compared with CF/epoxy resin, the s-CF/epoxy resin samples have slightly larger brown $\tan\delta_c$, which indicates that the epoxy resin concentration on the surface of CF is low or absent. The most likely reason is that the interface strength between epoxy CF is low, resulting in a network of direct connections between CF. This is consistent with the conclusion of the microstructure observed by SEM.

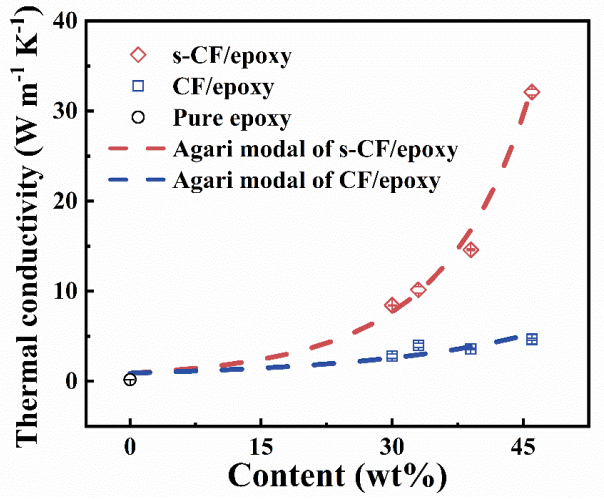

Figure 3.5. Thermal conductivity of s-CF/epoxy and CF/epoxy.

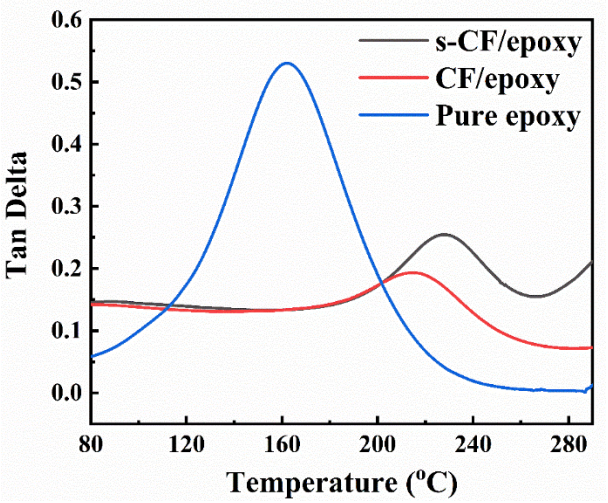

Figure 3.6. The DMA result of s-CF/epoxy, CF/epoxy and pure epoxy.

Thermal conductivity enhancement represents the improvement of Thermal conductivity of the composites compared with the matrix without filler. This parameter can be calculated according to

$$TCE = \frac{T_C - T_M}{T_M}\ 100\% \qquad (3.8)$$

Where, T_C is the thermal conductivity of the composite material, T_M is the thermal conductivity of the matrix. Figure 3.7 compares the TCE of s-CF/epoxy and CF/epoxy resins. When the CF content in s-CF/epoxy resin is 46 wt%, the best TCE value is 17137%. At the same concentration, the reinforcement effect of CF/ epoxy resin is 2471%, which is obviously better than that of unfilled matrix, but obviously lower than that of oriented carbon fiber obtained by pre-stressing.

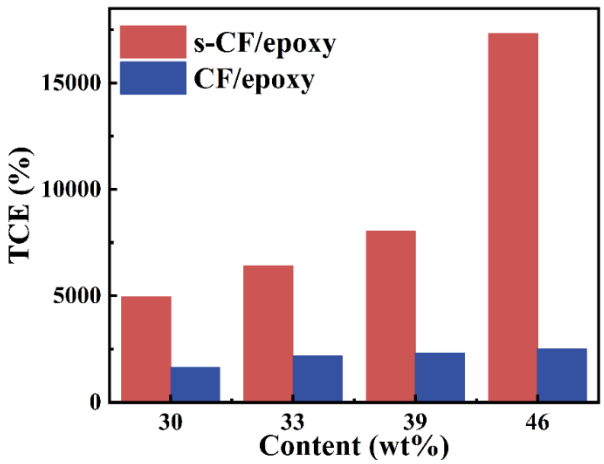

Figure 3.7. Thermal conductivity enhancement of samples

Figure 3.8(a) shows the decrease in thermal conductivity at higher temperatures. The thermal conductivity of s-CF/epoxy resin, CF/ epoxy resin and pure epoxy resin decreased from 32.6, 4.7 and 0.19 to 24.9, 3.9 and 0.17 w m^{-1} K^{-1}, decreasing by 24%, 17% and 11%, respectively, when the test temperature increased from 30 to 100 ^{o}C by 10 ^{o}C. The results show that the higher the CF content is, the faster the thermal conductivity decreases with the temperature. Figure 3.8(b) shows the thermal conductivity of 10 heating cycles. The thermal conductivity of these three samples can be affected by temperature, but the degradation of thermal conductivity is reversible, and the samples will return to the preheating stress temperature after cooling to room temperature. The thermal stability of composites is a key consideration for their practical application in electronic applications.

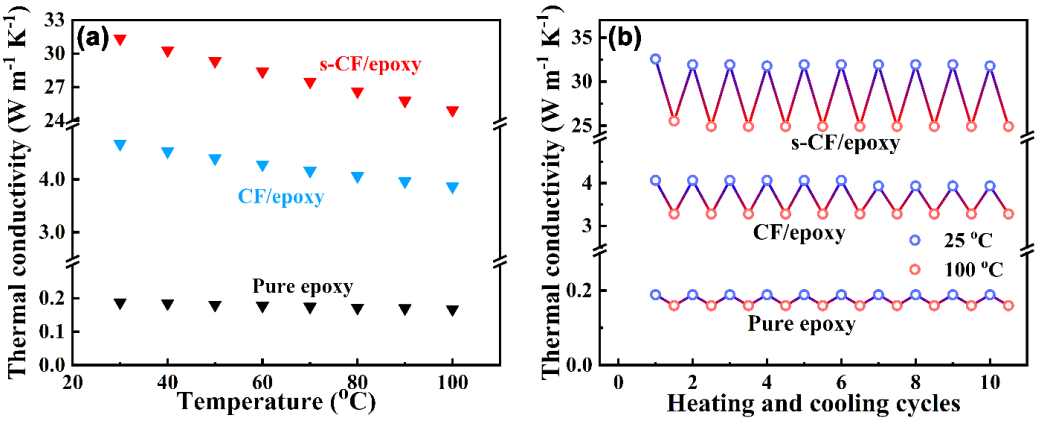

Figure 3.8. Thermal conductivity stability at high temperature. (a) The thermal conductivity of s-CF/epoxy, CF/epoxy and pure epoxy at different temperature vary from 30 to 100 °C (b) The thermal conductivity during 10 heating and cooling cycles.

The highest thermal conductivity obtained in this study is 32.6 W m^{-1} K^{-1}, 46%, which is equivalent to the thermal conductivity material made of 1D thermal conductivity filler. Table 3.2 shows the thermal conductivity of composite materials made of various metals, carbon nanotubes, glass fiber, ceramics, CF and other one-dimensional filler materials. [6-29] In figure 3.9, the TCE of the sample with the highest thermal conductivity among various fillers is calculated and compared. Since most polymer substrates are adiabatic, the TCE of different fillers is consistent with their thermal conductivity

Table 3.2. Comparison of the thermal conductivity and content of the s-CF/epoxy with the thermal conductivity and content of previously reported composites filled by 2D fillers including ceramics, glass fibers, carbon nanotubes, CFs, metals.

Fillers	Concentrations (wt%)	Concentrations (vol%)	resin	Thermal Conductivities (W m^{-1} K^{-1})	References

Ceramics	Boron Nitride	48.4		Epoxy	6.72	239
	Boron Nitride	2.0		Epoxy	0.21	240
	Silicon Nitride	81.1	60.0	Epoxy	9.20	241
	Basalt	40.0		Epoxy	0.95	242
	Porous Ceramic	50.0		Epoxy	0.47	243
Glass Fibers		27.0	15.0	Epoxy	0.34	244
		50.0		Epoxy	0.71	245
Carbon Nanotubes		3.0		Epoxy	0.28	246
		1.0		Epoxy	0.38	247
		0.6		Epoxy	1.2	248
		0.7		Epoxy	0.6	249
		1.0		PMMA	2.43	250
		1.5		PA6	0.27	251
		0.4		S160	1.21	252
Carbon Fibers		13.2		Rubber	23.3	253
		7.0		Epoxy	0.5	254
		7.5		Epoxy	1.75	255
		50.0		pCBT	6	256
		20		PDMS	2.73	257
Metals	Ag	46.5	9.0	PC	30.3	258
	Ag	66.4	25.0	PVDF	1.61	259
	Au	37.4	3.0	PDMS	5	260
	Ag	30.5	4.0	PDMS	6	261
	Cu	7.2	0.9	PA/SR601	2.46	262

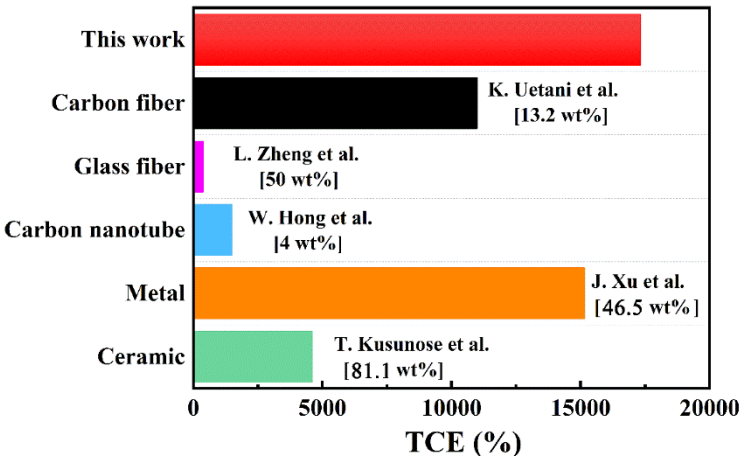

Figure 3.9. The representative results of thermal conductive polymer composites with

To demonstrate the thermal conductivity of these composites at different filling weight percentages, the samples were heated together on a ceramic heater powered with 12 V direct current. The samples were tailored to 1 cm^2 square with about 1mm thickness and put on the heater. The environment is room temperature without air flow. Figure 3.10(a) is the infrared image extracted during heating. During the heating process, the infrared images are token every 30 s, and during the cooling process, the time step was extended to 60 s. Dark colors represent low temperatures and light colors represent high temperatures. It is obvious that the temperature of s-CF/epoxy resin rises faster than that of CF/epoxy resin and epoxy resin samples. When the heater was turned off after 120s, the temperature peaks of s-CF/epoxy, CF/epoxy and pure epoxy samples were 97.4 ^oC, 94.8 ^oC and 82.9 ^oC, respectively. The temperature difference between s-CF/epoxy, CF/epoxy and pure epoxy can be determined from the infrared image and curing temperature in Figure 3.10(b). During the cooling process, although the temperature of s-CF/epoxy resin is always the highest due to the effect of the initial temperature difference, the temperature difference between samples decreases rapidly as time goes by. After 360 s, the temperatures of s-CF/epoxy resin, CF/epoxy resin and epoxy resin were 48.6 ^oC, 47.8 ^oC and 44.8 ^oC, respectively, which were significantly lower than those at 120 s. Figure 3.10(c) records the temperature during the cooling process. According to the definition of thermal conductivity, we already know that when same power is applied on a material, the higher the thermal conductivity is, the lower the temperature different between the two surfaces of material would be. Since the heat sink is exposed to air and

can be cooled efficiently, its temperature can be regarded as constant. So, by applying material with high thermal conductivity can suppress the temperature rise of the heat source. Imaging that the ceramic heater is an electronic equipment like chip which generate lot heat during working, if the power of equipment is the same, according to the analysis, by using the new material, heat can be transferred faster and chip can be cooled faster.

Thermochromic ink is sprayed on the surface of the sample heated by a ceramic heater, which appears red at room temperature and white when the temperature exceeds 65 ºC. s-CF/epoxy took 10s to reach the color transition temperature, while CF/epoxy took another 4s to study the color transition. The pure epoxy sample did not reach the transition temperature during observation as figure 3.10(d) shows. This trend is consistent with the thermal conductivity test results and supports our conclusion that s-CF/epoxy resin has excellent heat transfer ability.

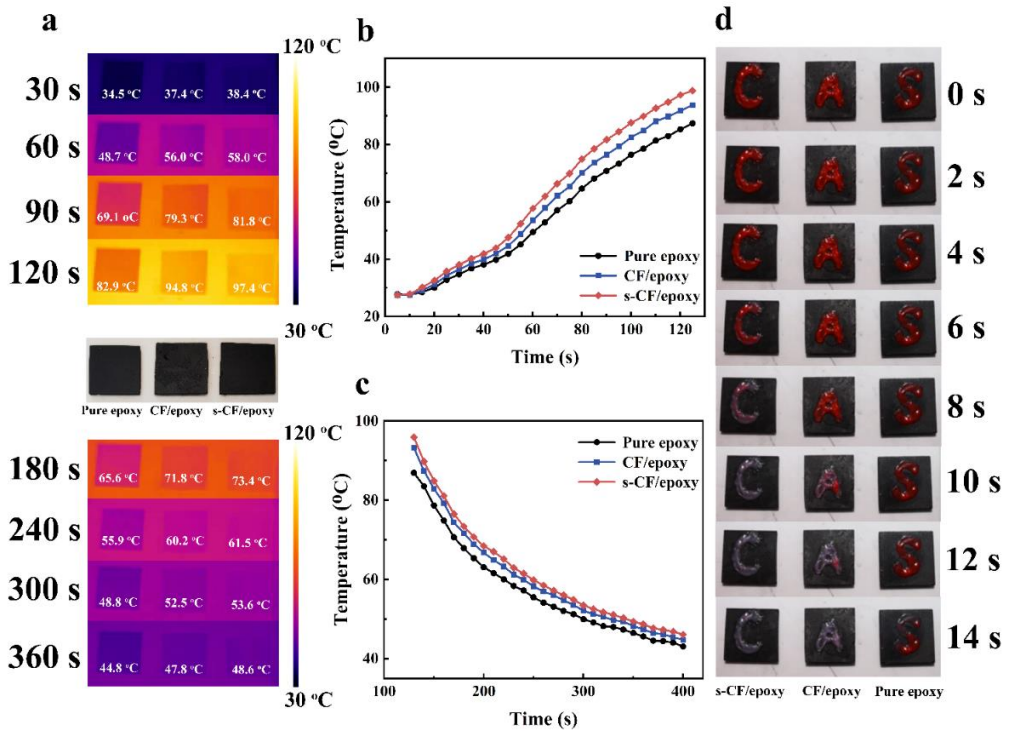

Figure 3.10. Temperature field analysis. (a) Infrared thermography of s-CF/epoxy, CF/

epoxy and pure epoxy at different times during heating and cooling. (b,c) The temperature of the sample during heating (b) and cooling (c). (d) Schematic diagram of thermochromic display devices with thermochromic ink patterns on different samples on hot plates.

3.6 Conclusion

In this chapter, we have fabricated a highly thermally conductive epoxy composite by stress induced orientation of CFs. Comparison with the existing composites using one-dimensional fillers, the s-CF/epoxy realized a high thermal conductivity of 32.6 W m^{-1} K^{-1} with a CF filler loading of 46 wt%. A new thermal conductivity enhancement record of 14,650% is reported. The main reason for this high value is that the orientation of CFs along the through-plane direction and a directly connected network between the CFs which builds an efficient heat path. Furthermore, we substantiate the orientation of CFs whose influence on thermal conductivity is demonstrated both by finite analysis and micro-CT statistics. As stress orientation is compatible with standard industrial processes, the proposed method has distinct advantages and a high potential in constructing filler frameworks to develop highly thermally conductive composites, which have broad applications electronics and beyond.

Chapter 4. Synergistic Effect on Constructing Thermal Interface Material with Low Thermal Resistance

4.1 Synopsis

In last chapter, we discussed the influence of filler alignment on thermal conductivity and enhanced the alignment of one-dimensional filler in two directions by compressing. Thereupon, the effectiveness of the method is proved and the efficiency can be taken into consideration. Compared with CF, graphite is an easily available material by handling the raw graphite ore and thereby cost less. Meanwhile, the method is supposed to exploit more potential of graphite as two-dimensional material. The high thermal conductive direction of carbon fiber and graphite is labeled as red arrows in figure 4.1.

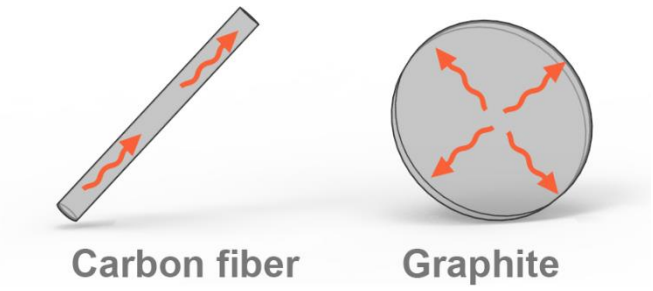

Figure 4.1. The high thermal conductive direction of carbon fiber and graphite.

The difference between the morphology of the materials causes the different thermal property. Under compression, materials tend to keep stable. one-dimensional materials like CFs, as we discussed in last

chapter, tend to align in the plane perpendicular to compression as figure 4.2(a) shows. However, by focus the direction of one-dimensional material like figure 4.2(b) shows, it is supposed to achieve a higher heat transport efficiency on specific direction. Unlike one-dimensional materials, two-dimensional materials conduct heat transfer in a plane, indicating that when two-dimensional planes are parallel to each other, the highest thermal conductivity can be detected in every direction within that plane as figure 4.2(c) shows.

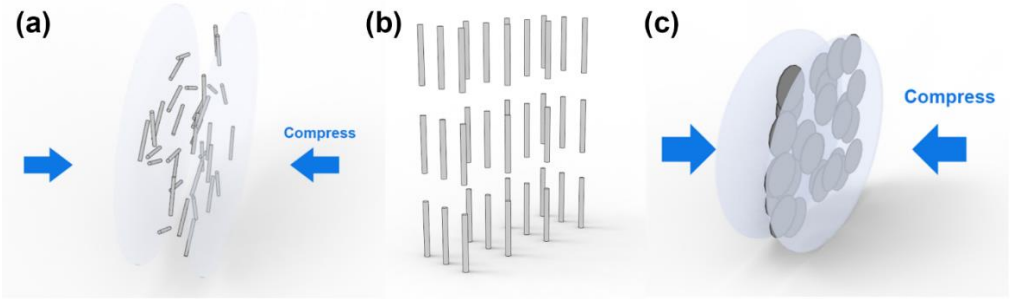

Figure 4.2. Morphology of different fillers under compression.

Besides the morphology of fillers, interaction between fillers and matrix were proved to have a nonnegligible impact on thermal conductivity. Weak interaction causes an extra thermal resistance breaking the thermal pass between matrix and filler. Various coupling agents were sometimes introduced to enhance the weak interaction between filler and matrix.[263-266] It was discovered that with the help of silane coupling agent, interaction between fillers can be enhanced, and so that thermal conductivities of composites rise.

In this chapter, method introduced in last chapter was applied to graphite to contract a thermal interface material which has become the leading solution for electronic devices to achieve lower operating temperatures. In order to improve the thermal conductivity and reduce the thermal

resistance, the thermal properties of carbon fiber - graphite interface materials were studied. When the ratio of carbon fiber to graphite was 1:1, the thermal resistance decreased to 1.8 K m^2 W^{-1} at 30 psi, while the thermal conductivity decreased from 34 to 19 W m^{-1} K^{-1}. The synergistic effect of carbon fiber and graphite was studied. The surface roughness of TIM was measured, and two different types of thermal conductivity measurements were used to demonstrate that graphite contributes to the thermal conductivity of the body, while CF plays an important role in smoothing the surface, thereby reducing the thermal resistance. In practical applications, the mixed packing performs better in enhancing the heat conduction of electronic packaging.

4.2 Characteristic of Graphite

As carbon material, graphite was characterized here and compared with CFs. The SEM images, Raman spectrum and XRD spectrum obtained are shown in figure 4.3. According to SEM images, the average diameter of graphite is 600 μm. Distribution graph of graphite size is given in the inset. In the XRD pattern shown in figure 4.4(a), peaks at 26.4° and 54.5° were observed and assigned to graphitic (002) and (004) planes. The appearance of (004) signal implies the carbon structure of graphite is of 3D crystalline order. Raman spectroscopy is another method frequently used to analyze carbonaceous structures. The Raman spectra of milled CF and graphite are similar to that of graphene. In the Raman spectrum shown in figure 4.4(b), bands around 1353, 1582, 2461 and 2704 cm^{-1} are labeled as D, G, D+D'' and 2D bands, respectively. The D-band is derived from the defects and disorder in the carbonaceous structure, and the G-band arises from ordered graphitic structure. The D+D'' band is

related to the combination of a D phonon and a longitudinal acoustic phonon branch. The 2D band is related to stacked graphene layers.[267-268] The Raman spectra indicate the similarity of defect and stacked layers between CF and graphite used here.

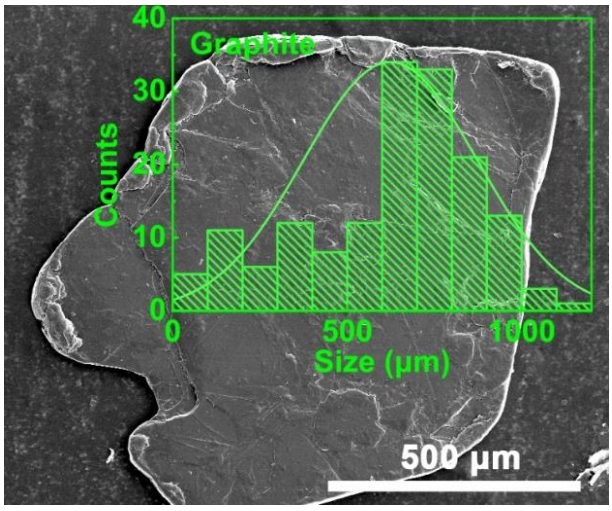

Figure 4.3. SEM image of graphite.

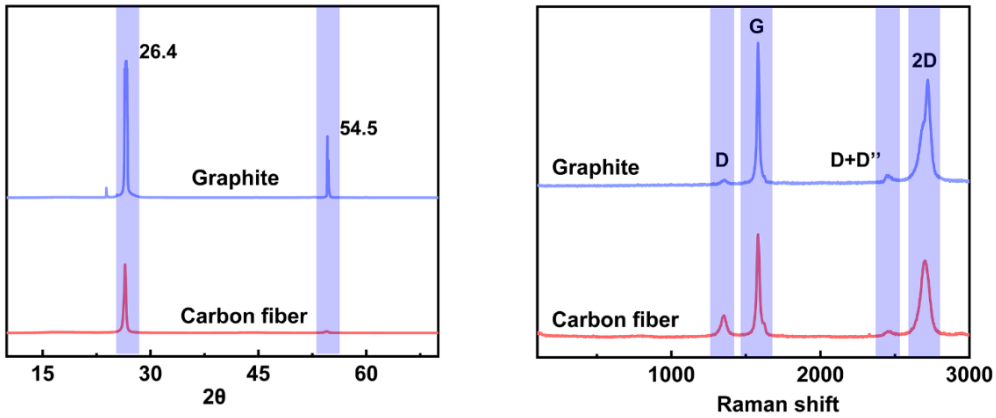

Figure 4.4. XRD and Raman spectrum of Graphite and CFs.

4.3 Preparation of composites

Vinyl-terminated polydimethylsiloxane 42.0 g and 3 drops of platinum(0)-1,3-divinyl-1,1,3,3-tetramethyldisiloxane complex solution with a mass of about 0.1 g were mixed in a high-speed mixer. Then 42.0 g of polymethylhydrosiloxane and 36.0 g of ethyl acetate were added to the

matrix and remixed. The compound labeled silica gel is then used as the matrix material.

The heat conductive filler is made of carbon fiber and graphite in different proportions. Before use in the composites, carbon fibers and graphite were heated at a temperature of 450 °C for 2 h. At the same time, some fillers were treated with KH-570 to investigate the effect of coupling agent. The mixture of 5.0 g filler, 10.0 g ethanol, 0.2 g KH-570 and 0.2 g glacial acetic acid was treated with ultrasound for 30 min. After filtration, the mixture was dried at 85 °C for 8 h to conjugate with the coupling reagent.

To accommodate raw materials, our lab produces custom designed molds. The process filler is pressed into the mold, and the characteristics of the mold design are shown in figure 4.5(a) and (b) respectively. A photo of the mold can be found in figure 4.5(c). The filler is added to the gap in the mold and a thin metal plug is used to apply pressure to the filler. The silicone is then poured into the mold opening. The whole mold is placed in vacuum (-80 ~ -90 kPa) for 4 h to exhaust the air around the fillers. The mold was then placed under a standard pressure of 85 °C for 48 hours, and the silica gel solidified. The cured composite was then used for subsequent characterization. The composites prepared from pure graphite and CF were labeled g-Si and CF-Si, respectively. CF:G= 3:1-Si, CF:G= 1:1-Si, CF:G= 1:3-Si indicate that the ratio of graphite to CF is 3:1,1:1, and 1:3 respectively. These samples were not treated with coupling agent and were labeled as original samples. If the filler is treated with KH-570, the corresponding samples are labeled g-C-Si, CF:G= 3:1-C-Si, CF:G= 1:1-C-Si, CF:G= 1:3-C-Si, and CF-C-Si represents the increasing order of CF concentration, where C represents these samples

are treated with coupling agent. Samples treated with the coupling agent are labeled as "coupled samples" to distinguish them from "original samples".

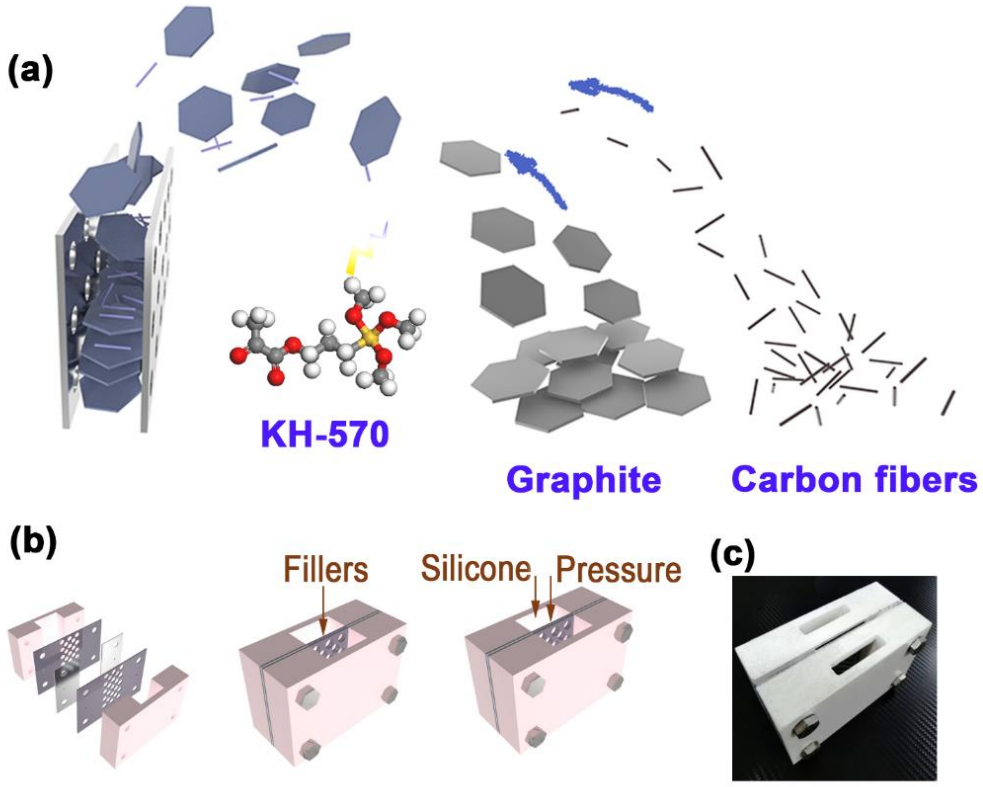

Figure 4.5. Schematic of sample preparation. (a) The process of compress graphite and carbon fiber into the mold. (b) Assemble mold and sample preparation procedures. (c) Photographs of the molds.

4.4 Finite element analysis of composite with different filler alignment

To illustrate the role of graphite in thermal conduction, finite element analysis was used. Carbon fiber and graphite were abstracted as cylindrical rods and pans in form. Different from last chapter, 2D model can hardly simulate the physical process because here 2D fillers were used, so a 3D model was built to do the simulation.

4.4.1 Thermal conductivity tensor of fillers in universal coordinate system

Both the CF and graphite are anisotropic materials, so the thermal conductivity should be expressed as a tenser. In a Cartesian coordinate system ($\overrightarrow{x'}, \overrightarrow{y'}, \overrightarrow{z'}$), the thermal conductivity of CF and graphite have been set as follows:

$$k_{CF} = \begin{bmatrix} 10 & 0 & 0 \\ 0 & 10 & 0 \\ 0 & 0 & 900 \end{bmatrix}, \; k_G = \begin{bmatrix} 100 & 0 & 0 \\ 0 & 100 & 0 \\ 0 & 0 & 10 \end{bmatrix} \tag{4.1}$$

in units of W m^{-1} K^{-1}. As figure 4.6(a) shows, the thermal conductivity of filler in composites need to be converted according to the relative position of principal axes system and the universal coordinate system ($\vec{x}, \vec{y}, \vec{z}$). Here, $\vec{x}, \vec{y}, \vec{z}$ is fix as follow.

$$\vec{x} = \begin{bmatrix} 1 \\ 0 \\ 0 \end{bmatrix}, \vec{y} = \begin{bmatrix} 0 \\ 1 \\ 0 \end{bmatrix}, \vec{z} = \begin{bmatrix} 0 \\ 0 \\ 1 \end{bmatrix} \tag{4.2}$$

The orientations of the rods in universal coordinate are randomly set as $\overrightarrow{x'}$, $\overrightarrow{y'}$ and $\overrightarrow{z'}$. The conversion matrix describing their relative orientation is then given by

$$T = \begin{bmatrix} \cos\langle \overrightarrow{x}, \overrightarrow{x'} \rangle & \cos\langle \overrightarrow{x}, \overrightarrow{y'} \rangle & \cos\langle \overrightarrow{x}, \overrightarrow{z'} \rangle \\ \cos\langle \overrightarrow{y}, \overrightarrow{x'} \rangle & \cos\langle \overrightarrow{y}, \overrightarrow{y'} \rangle & \cos\langle \overrightarrow{y}, \overrightarrow{z'} \rangle \\ \cos\langle \overrightarrow{z}, \overrightarrow{x'} \rangle & \cos\langle \overrightarrow{z}, \overrightarrow{y'} \rangle & \cos\langle \overrightarrow{z}, \overrightarrow{z'} \rangle \end{bmatrix} \tag{4.3}$$

The thermal conductivity matrixes of fillers in universal coordinate system were calculated by

$$k_{uni} = T k_{princ} T^T \tag{4.4}$$

where k_{uni} is the thermal conductivity matrix given in the universal coordinate system, k_{princ} is thermal conductivity matrix in the principal coordinate system and T^T is transpose of the conversion matrix.

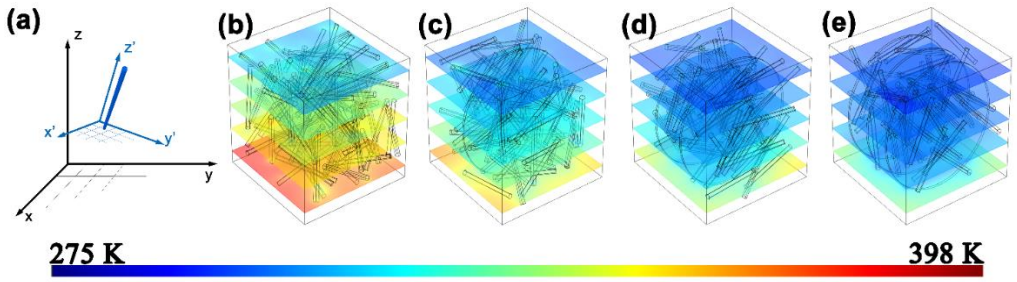

Figure 4.6. The schematic of coordinates and the heat transport simulation result.

4.4.2 Establishment of model

To establish the simulation model, a simulation box was configured to represent the material matrix of silica gel matrix with thermal conductivity of 0.18 W m^{-1} K^{-1} according to our measurements. A specific number of graphite sheets are introduced into the analog box. CF is then placed in the analog box without overlapping with graphite and other CFs. In figure 4.6(b-e), 0, 1, 2 and 3 graphite regions were placed in the box, respectively. Conversely, as the number of graphite sheets increased, the number of bars representing carbon fiber decreased from 100, 85, 70 to 55.

To establish the simulation model, MATLAB package was introduced. MATLAB script for generating 85 CFs was posted appendix A as an example for researchers to check and reuse.

4.4.3 Finite element analysis of composite.

The upper surface of the analog box is fixed at 293.15 K, and a 500W heater is attached to the lower surface of the analog box. The boundary on the front, back, left and right are adiabatic. The stationary condition is calculated from

$$\nabla \cdot \vec{q} = Q \tag{4.5}$$

$$\vec{q} = -k\,\nabla T \tag{4.6}$$

where $\vec{q}$ is heat transfer velocity, Q is the power of heat source, and T is the temperature field. For analysis, five equally spaced cross-sectional areas with the z-axis normal to the surface of the planes are chosen. The temperature contours on the planes are depicted with a temperature scale given in figure 4.6. As the results show, with the increase in the proportion of graphite in the simulation box, temperature of heat source decreases apparently. The thermal conductivity of different formulations was analyzed and compared.

4.5 Thermal properties evaluations

In order to evaluate the thermal performance of the sample, LFA and TRCMA are used for testing due to the different testing principles of the two methods, and confirmatory evidence can be obtained. The principle of LFA is shown in figure 4.7(a). The sample is heated by laser and the temperature of its opposite surface is monitored by an infrared detector. Strictly speaking, the measurement result of this technique should be considered as bulk thermal conductivity.

$$R_{TIM} = \frac{1}{k} \tag{4.7}$$

where R_{TIM} is the thermal resistance of the TIM, and the k is the bulk thermal conductivity.

Table 4.1. The raw thermal property data of samples.

Thermal diffusivity ($mm^2\ s^{-1}$)	**density ($g\ cm^{-3}$)**	**Cp ($J\ g^{-1}\ K^{-1}$)**	**Thermal conductivity ($W\ m^{-1}\ K^{-1}$)**	**TCE %**
original				
12.73	1.55	0.86	17.03	9311.83
7.07	1.35	0.95	9.03	4938.96

9.53	1.29	1.16	14.34	7840.82
9.39	1.20	1.19	13.36	7305.69
6.00	1.13	1.18	7.95	4347.99
coupling				
26.80	1.48	0.86	34.04	18607.25
14.10	1.53	0.95	20.43	11168.57
11.40	1.44	1.16	19.13	10455.71
9.65	1.52	1.19	17.41	9519.73
7.53	1.15	1.18	10.23	5594.89
Silica				
0.12	1.53	0.97	0.18	0.00

The thermal conductivity of the sample without curing agent was measured by LFA method, as shown in Figure 4.7(b), and marked as the original sample. The raw data was plotted in table 4.1 When more graphite was used, we can achieve a higher thermal conductivity. This result is supported by finite element analysis. According to the experiment and numerical simulation, it may resource from the better alignment of 2D filler under compression. Appling pressure on 1D and 2D filler, both of them tend to align their short edge along the compress direction which is a more stable state. Comparing the alignment of fillers with different morphology, it can be seen that the through plane direction of composite can always fall into the high thermal conductive plane of 2D filler, while there is an angle between axial direction of 1D filler and through plane direction of composite although the average angle become smaller under compress according to the conclusion of the previous chapter. According to the simulation, the application of 2D filler with a comparable thermal conductivity can promote the apparent thermal conductivity of the resulted composite. This can explain the downtrend of thermal conductivity with more carbon fiber loading in experimental

measured thermal conductivity curve. The next step is to examine the effects of coupling agents. Samples constructed with KH-570 treated filler were tested and labeled as coupled samples. The test results shown in figure 4.7(b) are for comparison with the original sample set. According to the results, at different CF/graphite ratio, the addition of coupling agent can help to improves the thermal conductivity of the composites. With the increase of CF content, the extent of thermal conductivity enhances caused by the presence of coupling agent decrease from 17.0 ,11.4, 4.8, 4.0 to 2.3 W m^{-1} K^{-1}. According to our measurements, the thermal conductivity of graphite composites increased by about 100%, while the thermal conductivity of CF composites decreased to 29% of the total. It is assumed that this phenomenon is due to the difference in surface roughness between samples. In different researches, since the variety of matrix with different thermal conductivity, thermal conductivity is somehow not enough to describe the enhance of method. Compared with pure silicon, the thermal conductivity of various composite materials is enhanced as shown in figure 4.7(c). The highest increase in thermal conductivity indicates an overall increase of 18,607%.

As introduced, two methods were introduced to evaluate the thermal property. Besides thermal conductivity, heat dissipation capacities of the sample under typical working conditions were also evaluated by TRCMA as well. There is a non-negligible thermal contact resistance here, and TRCMA technology is used to measure thermal resistance at pressure. Its principle is shown in Figure 4.7(d). The sample was secured with two copper stages at 30 psi. One stage is heated to a specific temperature of 80 ^{o}C. Then, the temperature of the other stage was measured. According to the definition of thermal resistance,

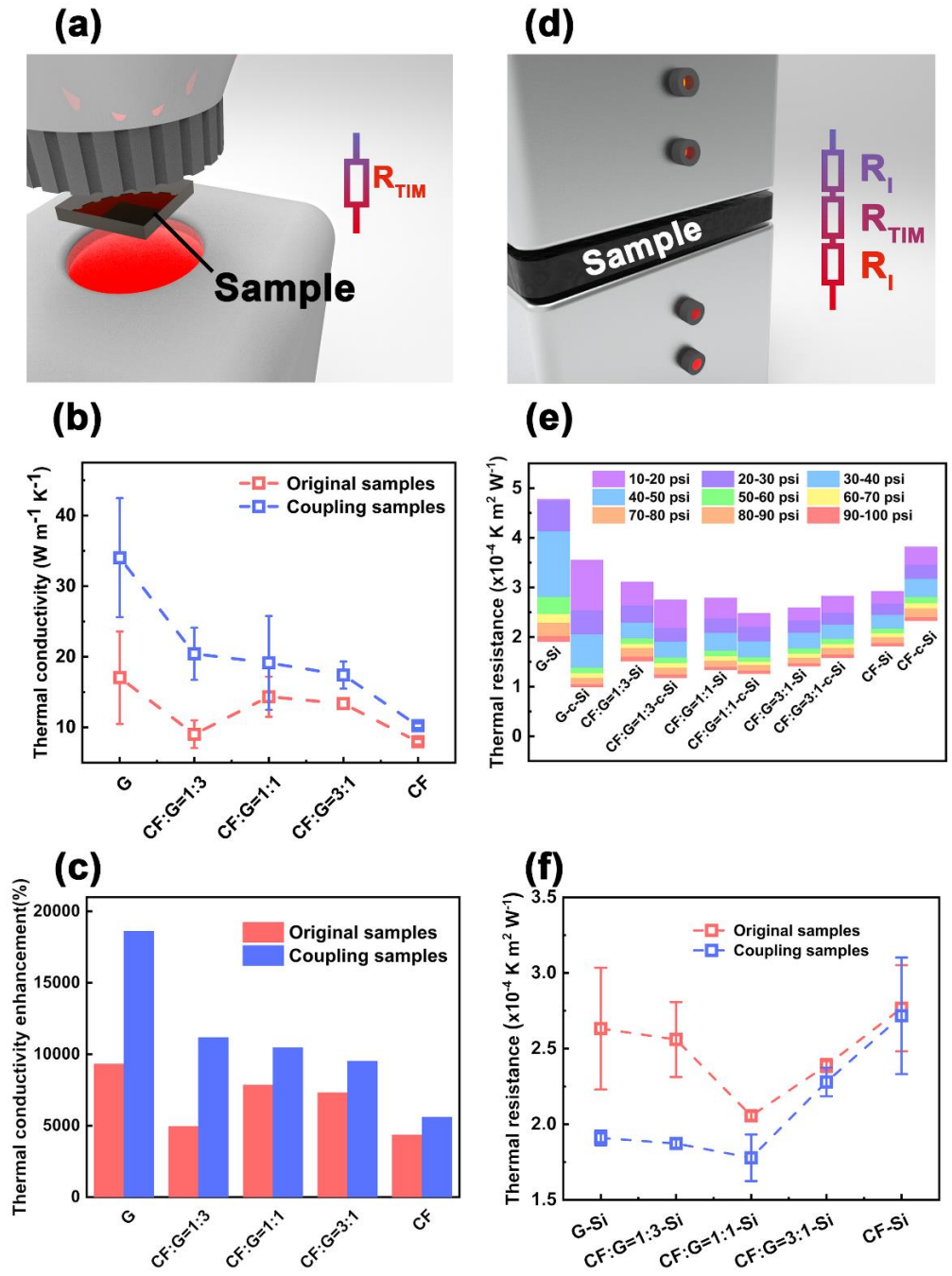

Figure 4.7. Thermal performance measurement. (a) Schematic diagram of LFA setting. (b) measured thermal conductivity, and (c) enhanced thermal conductivity of TIMs relative to silica gel. (d) Schematic diagram of TRCMA setting. (e) Thermal resistance of TIMs at different pressures. (f) Thermal resistance of TIMs at 30 psi.

$$I = \frac{T_h - T_c}{Q} \times A \tag{4.8}$$

where T_h and T_c are the temperature of the two copper stages, Q is the

energy passing through the sample, A is the area of the sample's cross section. In addition to R_{TIM}, there is another factor delaying thermal transport, the thermal contact resistance (R_c).[16] The measured thermal resistance, R_M consist the bulk thermal resistance of TIM and two thermal contact resistances. The relationship between R_{TIM}, R_M and k is showed here,

$$R_{TIM} + 2\,R_C = R_M > \frac{1}{k} \tag{4.9}$$

Figure 4.7(e) depicts the thermal resistance at different pressures and temperatures of 80 °C. The measured thermal resistance decreases with increasing pressure. And the thermal resistance, thermal conductivity data was summarized in table 4.2 and 4.3

Table 4.2. The thermal resistance of samples at different pressure.

Thermal resistance (x10^{-4} K m^2 W^{-1})	Pressure 10 psi	20 psi	30 psi	40 psi	50 psi	60 psi	70 psi	80 psi	90 psi	100 psi
G-Si	4.8	4.7	4.1	3.3	2.8	2.5	2.3	2.1	2.0	1.9
G-c-Si	3.5	2.5	2.0	1.5	1.4	1.3	1.2	1.1	1.0	1.0
CF:G=1:3-Si	3.1	2.6	2.3	2.1	2.0	1.9	1.8	1.7	1.6	1.5
CF:G=1:3-c-Si	2.7	2.2	1.9	1.7	1.6	1.5	1.4	1.3	1.2	1.2
CF:G=1:1-Si	2.8	2.4	2.1	1.9	1.7	1.6	1.5	1.4	1.4	1.3
CF:G=1:1-c-Si	2.5	2.2	1.9	1.7	1.6	1.5	1.4	1.4	1.3	1.3
CF:G=3:1-Si	2.6	2.3	2.1	1.9	1.8	1.7	1.6	1.5	1.5	1.4
CF:G=3:1-c-Si	2.8	2.5	2.2	2.1	2.0	1.9	1.8	1.7	1.6	1.6
CF-Si	2.9	2.7	2.4	2.3	2.2	2.1	2.0	1.9	1.9	1.8
CF-c-Si	3.8	3.4	3.2	3.0	2.8	2.7	2.6	2.5	2.4	2.3

In most cases, a thermal resistance at 30 psi can be used to predict the performance of the TIMs at work. As shown in figure 5.7(f), which shows a comparison of all samples. When the ratio of graphite to CF was 1:1, TIM had the lowest thermal resistance regardless of the use of coupling

agent. This phenomenon highlights the synergistic effect of carbon fiber and graphite on reducing low thermal resistance in proper proportion. Since the maximum thermal conductivity of the body belongs to G-C-Si, this result seems to indicate that the inverse relationship between thermal conductivity and thermal resistance has been broken. However, given the different test principles, the irregularities can reasonably be attributed to the difference in thermal contact resistance between the sample and the copper stage. Thermal contact resistance is positively correlated with surface roughness as previous work has suggested.[269-271]

Table 4.3. The thermal conductivity and thermal resistance at 30 psi

	Thermal conductivity (W m K^{-1})	Thermal resistance at 30 psi ($x10^{-4}$ K m^2 W^{-1})
G-Si	17.0	4.1
CF:G=1:3-Si	9.0	2.0
CF:G=1:1-Si	14.3	2.3
CF:G=3:1-Si	13.4	1.9
CF-Si	8.0	2.1
G-c-Si	34.0	1.9
CF:G=1:3-c-Si	20.4	2.1
CF:G=1:1-c-Si	19.1	2.2
CF:G=3:1-c-Si	17.4	2.4
CF-c-Si	10.2	3.2

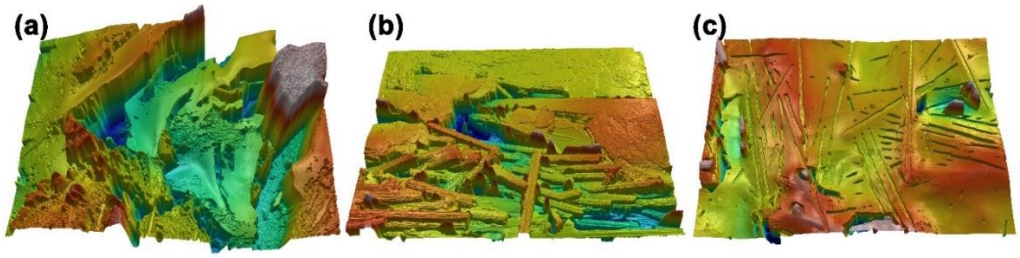

Figure 4.8. The 3D morphologies of G-Si, CF:G=1:1-Si and CF-Si, respectively.

To confirm this explanation, the roughness of G-Si, CF:G=1:1-Si and CF-Si was measured with a 3D profilometer and shown in figure 4.8. The sharp jumps on the g-Si surface indicate that the volume between the graphite is difficult to fill with silicon. The calculated average surface roughness of G-Si is 60.1 μm. Compared with G-Si, CF:G=1:1-Si and CF-Si have smoother surfaces, and the parameters are 8.21 and 6.57, respectively. Smooth surfaces are expected to provide low thermal contact resistance.

Then, the stability of the 3 typical samples during heating and cooling were evaluated as shown figure 4.9. The thermal resistance of three of the samples did not changes apparently during the heating and cooling cycles. The thermal resistance of CF-C-Si is about 2.5 × 10^{-4} K cm^2 W^{-1} and does not change significantly with temperature. However, for g-C-Si and CF:G= 1:1-C-Si samples, this value changes with the change of temperature. When the temperature is 40 °C and 100 °C, the average thermal resistance of G-C-Si is 1.60 and 1.75 ×10^{-4} K m^2 W^{-1}, respectively, and that of CF:G= 1:1-C-Si is 1.40 and 1.49 ×10^{-4} K m^2 W^{-1}, respectively.

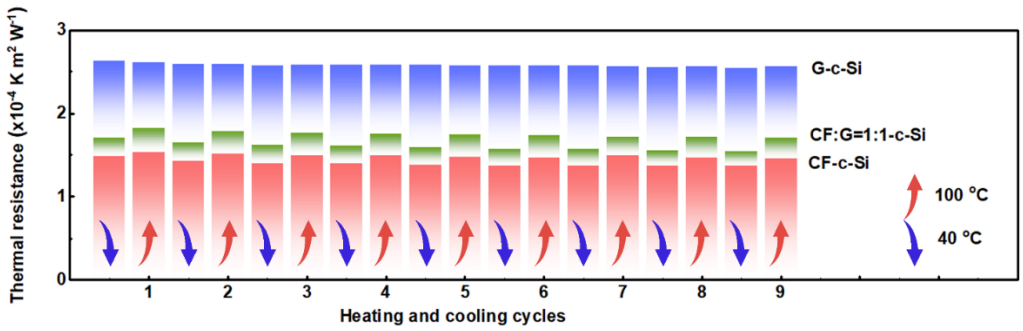

Figure 4.9. Thermal resistance changes of TIMs during 9 heating and cooling cycles.

In order to intuitively display the thermal behavior of the sample, we collected an infrared image, as shown in figure 4.10(a). Neat silica gel is placed on a heater along with 3 representative samples. Infrared cameras record temperature changes on the top surface in heating and cooling cycles. The corresponding relationship of temperature is reflected by color scale shown in figure 4.10(a). In the heating process, CF:G= 1:1-C-Si has the brightest color, indicating the highest temperature among the 4 samples. Due to the low thermal resistance of CF:G= 1:1-C-Si, heat can pass through CF:G= 1:1-C-Si quickly, making the temperature of the top surface rise quickly. During cooling, waste heat is conveyed from the bottom surface to the top surface and is dissipated by convection of atmosphere. Samples with low thermal resistance show rapid cooling. figure 4.10(b) and (c) show the temperature of each sample at selected time points during the heating and cooling cycles. In order to display the performance under the service condition, a further test was done applying the sample directly between the CPU chip and the fan-cooled fin. The schematic diagram of experimental instrument was shown in figure 4.10(d). The CPU then runs at full load to generate heat with maximum power, meanwhile the temperature was recorded as showed in figure 4.10(e). The thermal conductivity of silicone resin is poor, and the corresponding temperature of CPU reaches more than 90 °C. The other

three samples performed much better due to the use of thermal fillers. Among them, CF:G=1:1-C-Si showed the best performance. This result is consistent with TRCMA measurements and supports the finding of a synergistic effect between carbon fiber and graphite.

4.6 Evaluation of mechanical property

Considering the specific application environment, TIM need to be soft to be squeezed into the gap between heat sink and heat source. To evaluate the hardness, shao-00 test was introduced. The results of all samples are in the range of 45-50 without obvious fluctuation. According to test result, all samples is soft enough for application.

4.7 Conclusion

In summary, a method to prepare silicon TIM using graphite and CF as thermal conductivity filler is proposed in this chapter. By aligning graphite in the entire plane direction, TIM achieved a bulk thermal conductivity of 34 W m^{-1} K^{-1}, an 18,607% improvement compared to pure silicon. While this value is attractive, the thermal contact resistance is still too high to use as a TIM because its rough surface makes effective thermal coupling challenging. The 3D profilometer was introduced to prove the hypothesis that rough surfaces caused by gaps between graphite sheets. Thermal resistance can be reduced when CF is used to fill the void at the expense of body thermal conductivity to smooth the interface. When graphite ratio CF = 1, the thermal resistance can be reduced to about 1.8×10^4 K m^2 W^{-1} with the assistance of 80 ^oC and 30 psi coupling agent, although the thermal conductivity is found to be reduced to 19.1 $W^{-1}m^{-1}$ K^{-1} for the most part. The resulting TIM samples have obvious advantages in applications requiring sufficient softness, appropriate compressibility, and strong heat

conduction.

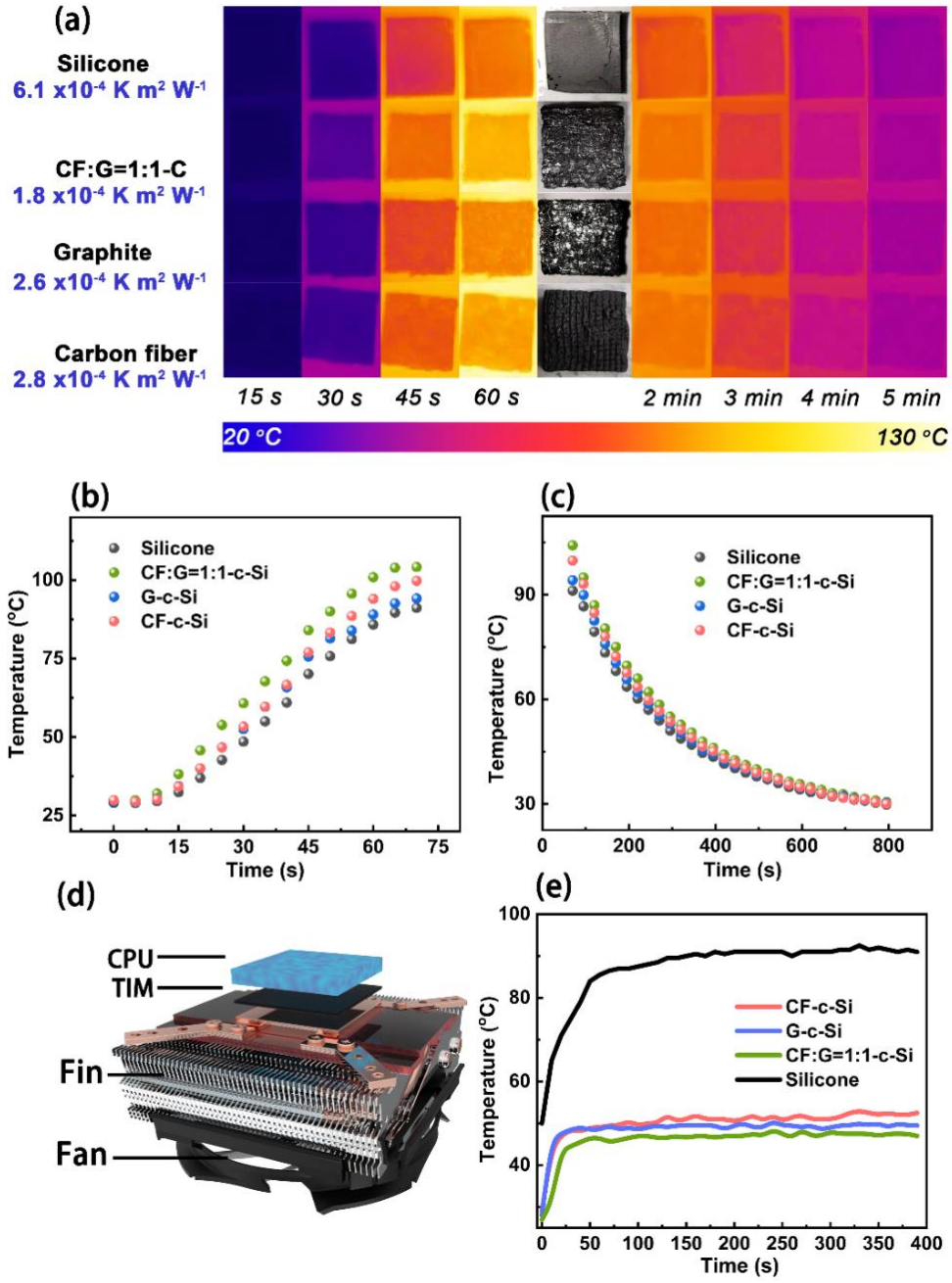

Figure 4.10. Temperature change of top surface of samples during the heating and cooling process. (a) Infrared images of samples during the heating and cooling process at selected times. (b, c) Temperature data for the samples at different times during the heating and cooling phases, respectively. (d) Sketch of the use of the samples to a CPU to enhance cooling. The blue block represents the CPU and the black sheet represents a TIM sample. (e) The temperature of the CPU under full-load operation.

Chapter 5. The Achievement of Metal-level Thermal Conductivity by Aligning CFs with the Help of Stretching Medium

5.1 Synopsis

As introduced in last chapter, by focusing the direction of one-dimensional materials like figure 4.2(b) shows, it is supposed to achieve a high heat transport efficiency on specific direction. Some methods have been developed to achieve this purpose. Besides freezing casting introduced in chapter 2, there are electrostatic flocking applied on aligning CFs.[253-254] Because employ electromagnetic field, this method was only applicable on conductive or magnetic fillers.

In this chapter, a developed method aligning 1D fillers was developed. This method was inspired by the making of a traditional Chinese noodle called lamian. The noodles are made by stretching dough, so the sample is called "Lamian". The 1D filler can be arranged well in a single direction by stretching the medium embedded with the filler. In addition, the filler can be bridged by the graphitized medium to form a heat-conducting frame. By applying this method, the strategy achieves unprecedented heat conduction across the plane. In this study, CFs was used as a filler material to give the composite a coefficient of thermal expansion comparable to that of many metals, which is the primary consideration in the design and selection of electronic packaging materials. The results

show that the composite has obvious advantages as a high thermal performance packaging material.

Here two influences were analyzed to explain the thermal conductivity rise. First one is the medium stretching cycles triggering the alignment of filler. To explain the relationship between the stretching cycles and the final thermal conductivity of composite, a mathematic mode was built up. The resulted formula is considered suitable to analyze the attitude of all 1D fillers in stretching process. The other one is the carbon structure variety with different thermal conductivity. Before and after graphitization, major change of the carbon structure in medium have taken place, which will be confirmed by different tests. The thermal conductivity different origin from the change is analyzed using molecular dynamics in LAMMPS package.

5.2 Preparation of epoxy composites

First, combine 7 g flour, 7 g CF and 8.4 g water in a high-speed blender. After knead Dough/CF the paste for 20 minutes, about 20 g paste was left for the waste in the process. The paste is then stretched to 10cm and folded at the middle point. This process is repeated for several cycles. Dip the stretched paste into liquid nitrogen for 5 minutes and transfer it to freeze dryer after being completely frozen. The sample is kept in the instrument for 48 hours to sublimate all the ice. The composite material composed of flour and CF was then pretreated at 1000 ^{o}C for 2 h under vacuum conditions, and the products of this step were labeled as preheated samples. After this, the pretreated sample was graphitized at 2800 ^{o}C argon for 2 hours to prevent reaction with the atmosphere. The amorphous carbon remaining as a result of flour decomposition is

recrystallized in the graphitization step to achieve enhanced thermal conductivity.

Mix the epoxy resin, curing accelerator and curing agent at a weight ratio of 100:5:95 until the curing accelerator is completely dissolved in the epoxy resin/curing agent mixture. The mixture is then injected into a carbon mesh made of carbon fiber and graphite carbon. The composite was then degassed in a vacuum oven at 60 ^{o}C for 1 hour, then the temperature was raised to 135 ^{o}C and kept constant for 2 hours for pre-curing, and then held at 165 ^{o}C for 14 hours to obtain the final thermal conductive composite. Epoxy composites are labeled as lamian-1,2,5,7,10 and 20 according to the number of stretching cycles. Schematic diagram of sample preparation shown in figure 5.1.

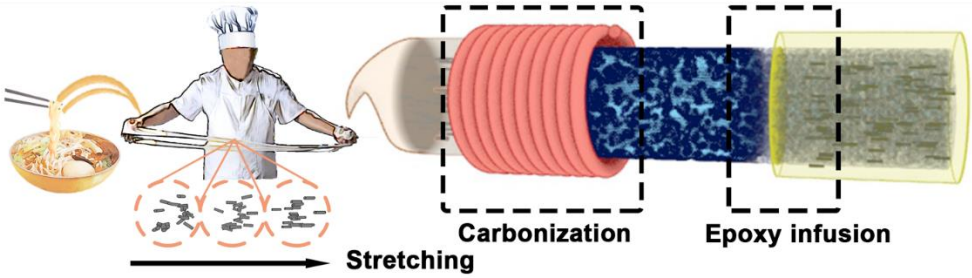

Figure 5.1. Schematic diagram of the strategy.

5.3 Thermal conductivity improvement

The thermal transport characteristics of samples are estimated using the results shown in figure 5.2, meanwhile, the raw data used to calculate thermal conductivity was plotted in table 5.1. According to measurement, the thermal conductivity of the preheated sample is 10.2 W m^{-1} K^{-1}. The graphitization process increases the value to 18.5 W m^{-1} K^{-1}, which reflects the influence of graphitization process on thermal conductivity. After stretching for 1, 2, 5, 10 and 20 times, the thermal conductivity increases to 83.2, 101.5, 105.6, 111.0, 119.8 and 109.8 W m^{-1} K^{-1},

respectively, reflecting the effect of carbon fiber arrangement on the thermal conductivity. The results show that after 10 stretch cycles, the value is stable at about 110 W m^{-1} K^{-1}, which is comparable to Al, Fe, Ni and other metals.

Table 5.1. The raw thermal property data of samples.

Stretching Turn	**Thermal diffusivity (mm^2 s^{-1})**	**Density (g cm^{-3})**	**Cp (J g^{-1} K^{-1})**	**Thermal conductivity (W m^{-1} K^{-1})**
Graphitized				
0	10.6	1.42	1.23	18.54
1	48.9	1.44	1.16	81.68
2	63.4	1.47	1.08	100.79
5	70.9	1.46	1.02	105.51
10	64.9	1.47	1.16	110.89
15	63.0	1.49	1.27	119.05
20	83.6	1.46	0.9	109.84
Preheated				
0	7.1	1.40	1.03	10.27
1	12.0	1.45	1.04	18.11
2	13.0	1.45	1.21	22.86
5	16.2	1.47	0.91	21.66
10	15.2	1.49	1.08	24.38

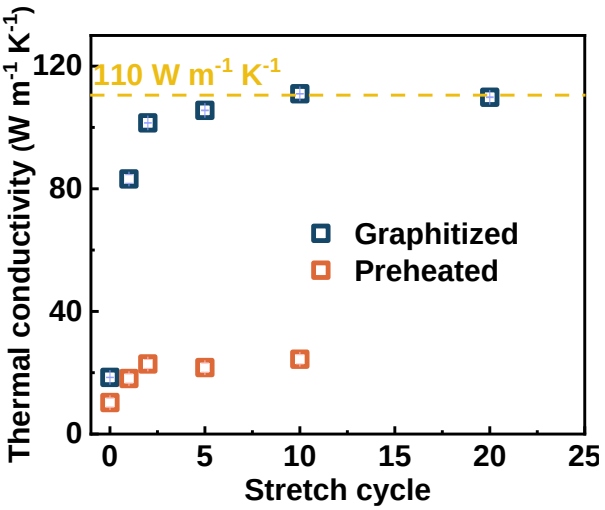

Figure 5.2. Thermal conductivity of samples with different stretch cycles.

Considering the influence of packing concentration on thermal conductivity, in order to determine the reason for the increase of thermal conductivity, it is necessary to control packing concentration thermal conductivity packing, in this case carbon from CFs and slurry is weighed by TGA. The material is stable in a nitrogen atmosphere where the epoxy resin decomposing at about 250 °C. The TGA curve obtained is shown in figure 5.3. The total carbon content of each sample was measured in the range of 43-45 wt%. Since the loading amount of thermal conductivity filler is similar in all samples, the huge difference in thermal conductivity coefficient is not caused by the different packing concentration.

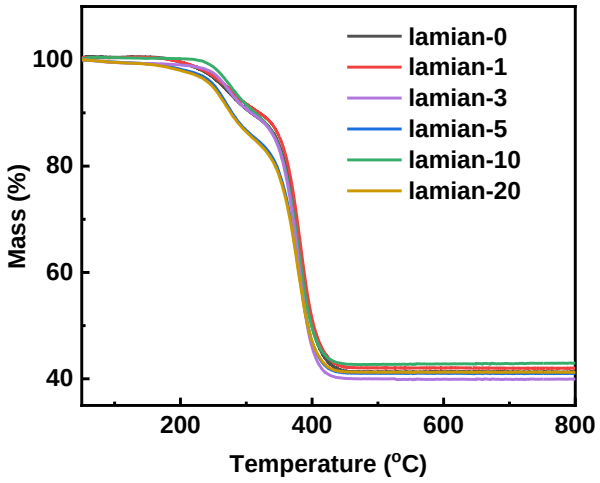

Figure 5.3. TGA analysis of Lamian samples with 0,1,3,5,10,20 stretching turn

In order to evaluate the stability of thermal conductivity to temperature, the thermal conductivity of the graphitized Lamian-10 sample after preheating was measured at different temperatures, as shown in figure 5.4(a), to evaluate the stability of thermal conductivity. The results show that the thermal conductivity does not decrease with the increase of temperature in the range of 20-100 °C. The exact data was given in table 5.2. In 10 heating and cooling cycles, all thermal conductivity of three samples were stable, as shown in figure 5.4(b). The thermal conductivity of the Lamian-10 has never fallen below 110 W m^{-1} K^{-1}. These two tests show that the sample has a high degree of thermal stability.

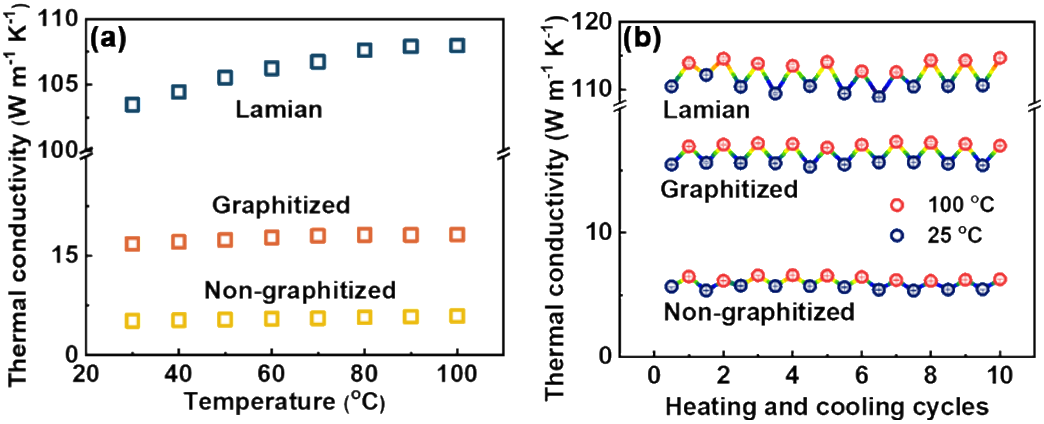

Figure 5.4. Thermal stability of thermal conductivity. (a) thermal conductivity at different temperatures. (b) Stability of thermal conductivity during 10 heating and cooling cycles.

Table 5.2. Thermal conductivity of samples at different temperature.

Temperature(°C)	**Thermal conductivity (W m^{-1} K^{-1})**		
	Preheated	Graphitized	Lamian-10
30	5.2	16.8	103.5
40	5.3	17.1	104.5
50	5.4	17.4	105.5
60	5.5	17.7	106.2

70	5.6	18.0	106.7
80	5.7	18.1	107.6
90	5.8	18.1	107.9
100	5.9	18.2	108.0

To determine the temperature dispersion in samples when used as thermal management material an infrared camera is then used to record the temperature of the sample as it is heated. four columns made of epoxy resin, preheated specimens, graphitized specimens and Lamian-10 were installed on the heater, as shown in figure 5.5(a). Figure 5.5(b) shows the temperature rise of the top surfaces of the samples which were also labeled in figure 5.5(a) in the heat process. The ambient temperature which is also the initial temperature of top surface is about 25 ^{o}C. After turning on the heater, temperatures of the top surfaces grow up at different speed. At 45s, this value of epoxy, preheated sample, graphitized sample and Lamian-10 rise to 26.2, 31.8, 42.7 and 48.9 ^{o}C respectively. The corresponding temperature rise average speed are 0.06, 0.16, 0.40 and 0.53 K s^{-1}. At the same time, 45s, the temperature of heater corresponding to them are 58.4, 53.7, 53.4, 51.3 ^{o}C, which phenomenon indicates the improvement of heat transport ability. Temperature dispersion at 0, 15, 30 and 45 s after the heater is turned on is shown in figure 5.6. The results show that the high temperature zone of sample Ramen-10 diffused rapidly to the top surface. In contrast, the epoxy surface remained significantly cooler than the bottom after 45 seconds. Under same condition, the temperature dispersion during heating process was simulated with finite element analysis, and the results were shown in figure 5.7. Color mapping is used here to show the temperature distribution on the sample surface. The lighter red means high temperature while dark blue means low temperature. Heat flow is represented by red arrows whose size is proportional to the density of

heat flow.

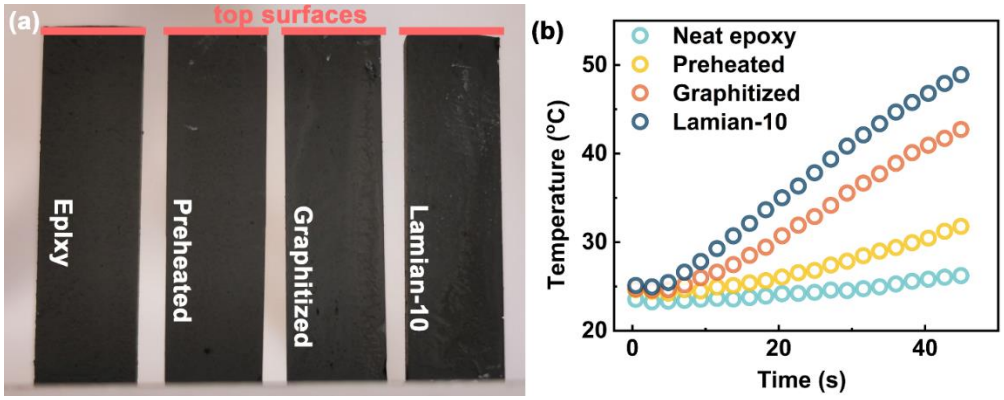

Figure 5.5. (a)Position of samples placed on the heater, (b)The temperature of top surface of samples

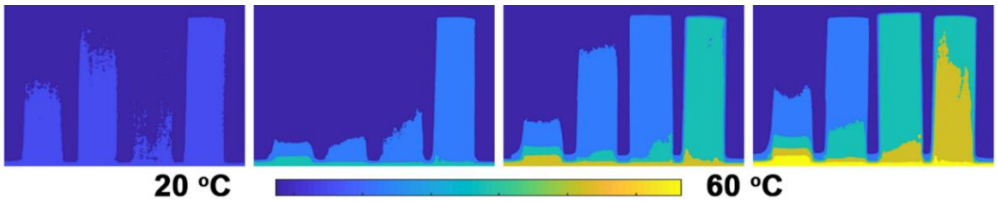

Figure 5.6. Temperature dispersion recorded by infrared camera.

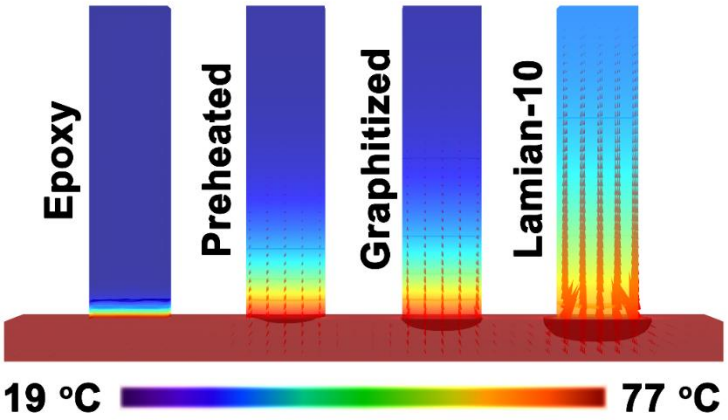

Figure 5.7. The temperature dispersion and heat flow calculated by finite element analysis.

According to the processing technology of CF, the previous research on CF thermal conductive composites was divided into three groups: randomly dispersed CF, directionally arranged CF and surface modified CF, as shown in Figure 5.8.[167, 253, 272-282] When CF was mixed with the

matrix material to produce randomly dispersed CF the thermal conductivity is generally less than 2 W m^{-1} K^{-1}. In these researches, because of the anisotropic thermal conductivity of CF and the random dispersion of CF, the direction with highest thermal conductivity can hardly be aligned on single direction, which causes the low efficient application of the thermal conductive filler. The thermal conductivity of the composites prepared by alighting the carbon fiber plates can reach tens of W m^{-1} K^{-1}. Surface modification can enhance the bonding between the matrix and CF or the bridging CF, forming additional thermal paths and thus enhancing heat exchange. Lamian-10 showed a significant improvement in thermal conductivity compared to the above studies, probably due to the synergy of the two enhancement mechanisms. Graphitized paste can be seen as a bridge between carbon fibers, at the same time, CF is aligned during stretching.

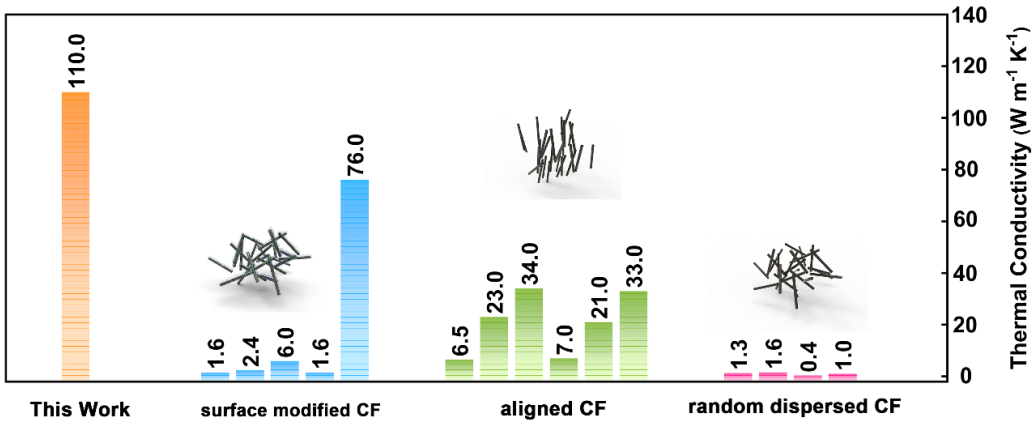

Figure 5.8. Review on thermal conductivity of carbon fiber composites. The composites were divided into randomly dispersed CF, directionally arranged CF and surface modified CF.

Previous work in our lab has also applied this strategy. Xiao et al. And Ali et al. Use cellulose and graphene as Bridges between fibers and introduce directional freezing technology to arrange carbon fibers into thermal conductive composites respectively. Their thermal conductivity

is 6.04 W m^{-1} K^{-1} and 21.19 W m^{-1} K^{-1} respectively.[190, 273] Lamian-10 has an even higher thermal conductivity than these. The structure of the bridge material is considered to differ from the previous work on Lamian-10. In the previous work, the bridge material was separated, whereas in Lamian-10, the carbon bridge in the gluten flour was generated in situ during the graphitization process. Because the slurry is continuous, it is reasonable to assume that the carbon produced forms a continuous network. The network and embedded oriented CF ensure efficient heat transfer.

5.4 The mathematic mode of 1D filler attitude in stretching process

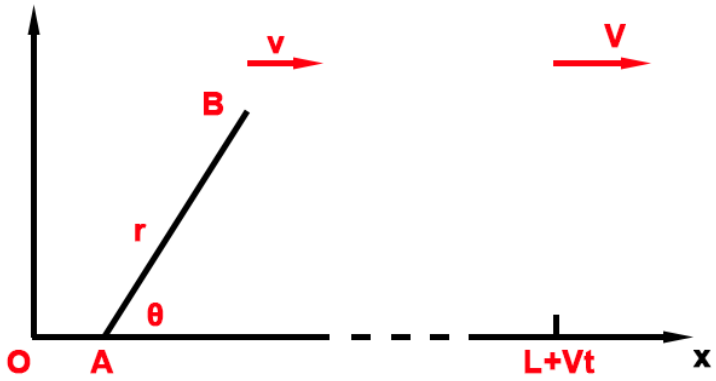

Figure 5.9. Schematic diagram showing the alignment of fillers during stretch process

In order to predict the effect of stretching on the arrangement of CFs in paste and the resulting change in thermal conductivity, a mathematical model was established. Assume that the length of the paste along the stretching direction at time t is L+Vt, where L is the initial length when t=0, V is the stretching speed, and t is the time of stretch. CF has two ends, A and B, and its length is r. Considering that the angle between AB and the stretching direction, θ, rather than the exact positions of A and B, determines the alignment condition of CF, for each CF, A coordinate

system can be established parallel to the stretching direction with A as the origin. Then the velocity difference of paste around B and A is V, and the relationship between v and V can be expressed as

$$v = \frac{r\cos\theta}{L+Vt}V \tag{5.1}$$

Wherever A and B is, v can always be resolved into two, parallel and perpendicular to CF. Only the perpendicular one contributes to the rotation of CF. It can be calculated as $v\sin\theta$. So,

$$-\frac{d\theta}{dt} = \frac{v\sin\theta}{r} \tag{5.2}$$

$$-\frac{d\theta}{dt} = \frac{\sin\theta\cos\theta\, V}{L+Vt} \tag{5.3}$$

Integrate the equation, it can be draw that

$$\ln(L+Vt) = -2\ln|\tan\theta| + C \tag{5.4}$$

Where C is constant.

Then the boundary condition was considered. Before stretching, the alignment of CF is randomly dispersed. But along the stretch direction, defined as x direction in figure 5.9, the two ends of CF with lower x coordinate can always be defined as A. In this condition, the range of θ is actually from 0 to $\frac{\pi}{2}$. Assuming in cartesian coordinate system, the average angle dispersion before stretching is $\overline{\theta_0}$. In chapter 4, we have a conclusion that the distribution of the endpoint on an annulus corresponding to a finite angle $\mathrm{d}\theta_0$ is

$$\mathrm{F}(\theta_0) = \sin\theta_0\, d\theta_0 \tag{5.5}$$

The $\overline{\theta_0}$ can be expressed as

$$\overline{\theta_0} = \int_0^{\frac{\pi}{2}} \mathrm{F}(\theta_0)\theta_0 \tag{5.6}$$

It can also be expressed in detail as

$$\overline{\theta_0} = \int_0^{\frac{\pi}{2}} \frac{2\pi\theta_0 r^2\sin\theta_0}{2\pi r^2}\,\mathrm{d}\theta_0 \tag{5.7}$$

$$\overline{\theta_0} = 1 \tag{5.8}$$

When t=t_0,

$$\theta = \overline{\theta_0} \tag{5.9}$$

$$C = \ln L + 2\ln|tan\theta_0| \tag{5.10}$$

$$\ln(L + Vt) = \ln L + \ln(\frac{\tan\theta_0}{\tan\theta})^2 \tag{5.11}$$

So

$$\tan\theta = \frac{\tan\theta_0}{\sqrt{1+\frac{Vt}{L}}} \tag{5.12}$$

$$\tan\bar{\theta} = \frac{\tan 1}{\sqrt{1+\frac{Vt}{L}}} \tag{5.13}$$

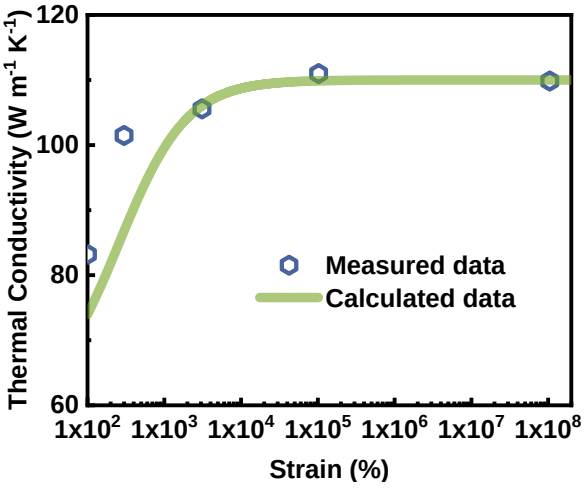

Figure 5.10. Thermal conductivity versus strain during stretches process. The blue points and green curve are measured data and calculated data respectively.

Then the relationship between thermal conductivity and CF arrangement is considered. In the specification of CF, the axial thermal conductivity is 900 W m^{-1} K^{-1}, while the radial thermal conductivity is only 10 W m^{-1} K^{-1}, which is extraordinarily lower compared with the that on axial direction. Suppose CF conducts heat axially and radially adiabatically. Then the thermal conductivity of the composite material in the tensile direction can be expressed as

$$\frac{k_{stretch}}{k_{CF}} = c \cdot \cos[\arctan(\frac{\tan 1}{\sqrt{1+\frac{Vt}{L}}})] \tag{5.14}$$

where $1 + \frac{Vt}{L}$ is actually the strain of paste and k_{CF} is the thermal

conductivity of CF on the axial direction. Since only the influence of packing orientation is considered in the model, a parameter c reflecting other structural characteristics is needed. Here

$$c \cdot k_{CF} = 110\ W\ m^{-1}\ K^{-1} \tag{5.15}$$

The formula was plotted with our measured data as Figure 5.10 shows.

5.5 Thermal conductivity analysis of different carbon structures

Then let us analyze the structure transformation of carbon during the graphitization. This phenomenon has actually been studied.[283-286] However, the structure transformation was still identified by various methods.

Figure 5.11 shows TEM images of preheated paste, graphitized paste and carbon fiber samples. The insertion depicts the corresponding electron diffraction patterns. The electron diffraction pattern of preheated paste shows diffuse halo rings, indicating the amorphous carbon structure remaining after paste decomposition. The slurry is decomposed under vacuum conditions so that the residue consists of amorphous carbon and bridged carbon fibers. After the preheating step, the slurry is heated to 2800 °C and held at the constant temperature for 2h, during which the residue is converted to a graphene structure. TEM of graphitized paste and CF were token to confirmed the transformation. From the electron diffraction pattern of the graphitized paste embedded in TEM as shown in figure 5.11(b), a clear diffraction pattern can be observed, in which multiple points of light were distributed around the polar angle, indicating a carbon polycrystalline form. TEM images of CF samples were shown in figure 5.11(c) for comparison with graphitized

paste. It can be found that the electron diffraction pattern tends to show a hexagonal diffraction pattern, confirming the existence of graphene.

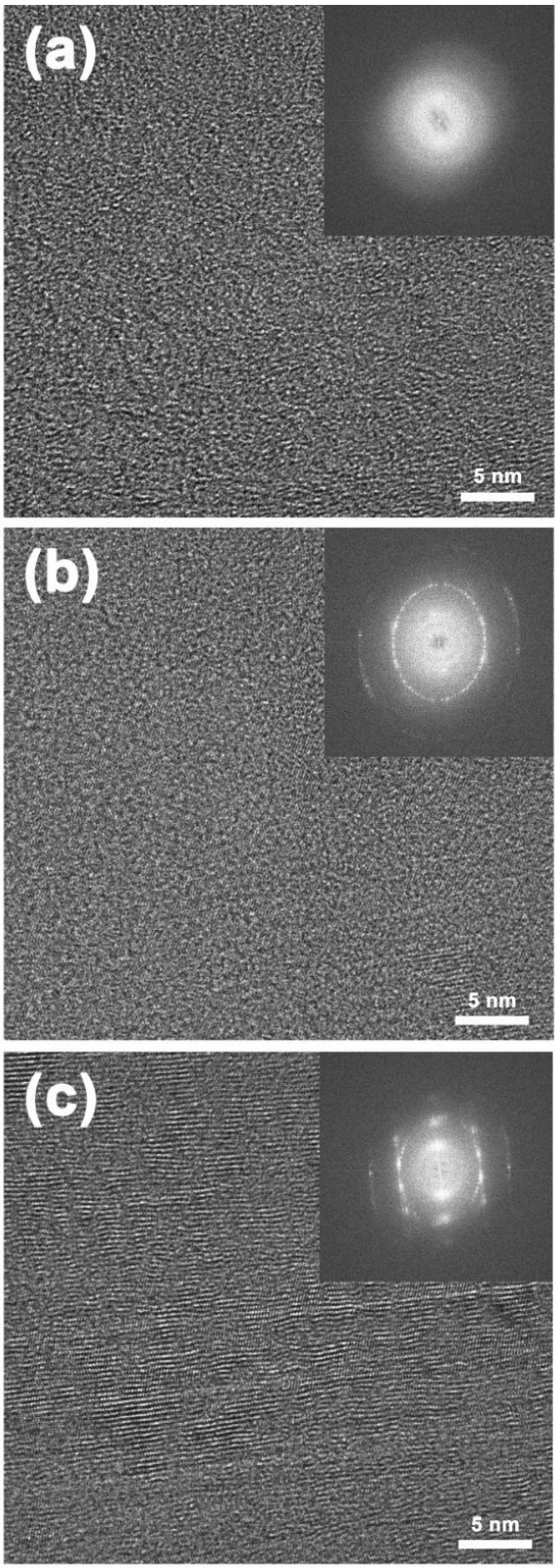

Figure 5.11. The TEM images of preheated paste, graphitized paste and CF. Insert of the TEM images are electron diffraction patterns that reflect the underlying carbon structure.

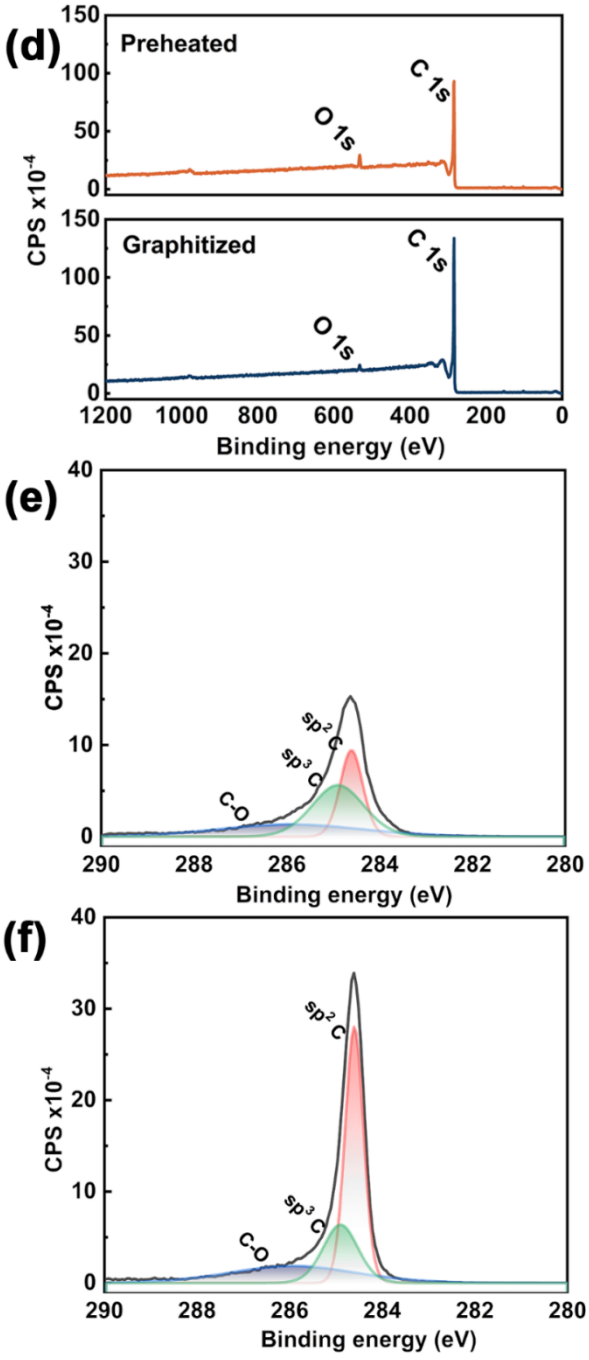

Figure 5.12. The survey and high-resolution XPS of preheated and graphitized paste.

XPS survey spectra of preheated paste and graphitized paste samples

are shown in figure 5.12(a). Figure 5.12(b, c) shows the high-resolution XPS spectra in the C1S state. A significant increase in sp2 hybrid carbon can be observed in the high-resolution spectrum, indicating the transition from sp3 to sp2 hybrid carbon. TEM and XPS results show that the amorphous sp3 carbon changes to the crystalline sp2 carbon during graphitization. Considering that the general form of sp2 crystalline carbon is graphene, it can be assumed that graphene structures are formed during this process. To further confirm this conclusion, Raman spectra of preheated paste and graphitized paste samples are given in figure. 5.13. Such as preheating paste Raman spectrum, D band intensity is stronger than G band, and after carbonization, D band almost disappeared. The resulting spectrum is similar to that of graphene. This phenomenon shows that the transformation of carbon atoms during carbonization can be regarded as the recrystallization of atoms, resulting in graphene with lower defect density. Taken together, these analyses clearly demonstrate the formation of graphite-carbon.

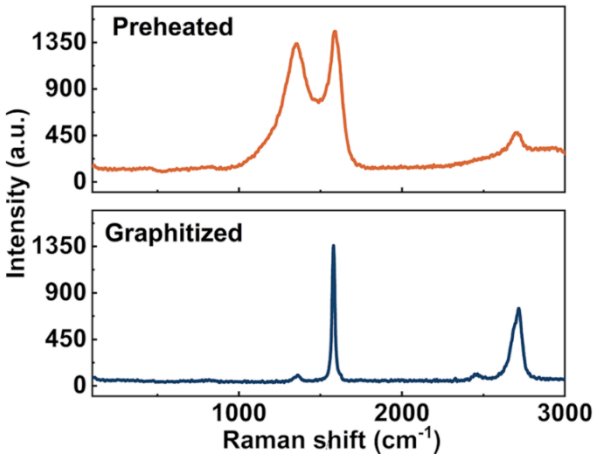

Figure 5.13. Raman spectrum of preheated and graphitized paste.

NEMD simulations were performed to analyze the influence of structural transformations on thermal properties. Different structural models were constructed, for amorphous carbon, spherical crystalline carbon, a

polycrystalline form of graphene with varied orientation (PGVO) and a polycrystalline form of graphene with aligned orientation direction (PGAO). Here, amorphous carbon represents the carbon structure of the preheated paste. The spherical crystal carbon and PGVO models represent two possible carbon structures for the graphitized paste. The PGAO model represents the carbon structure for the CF samples.

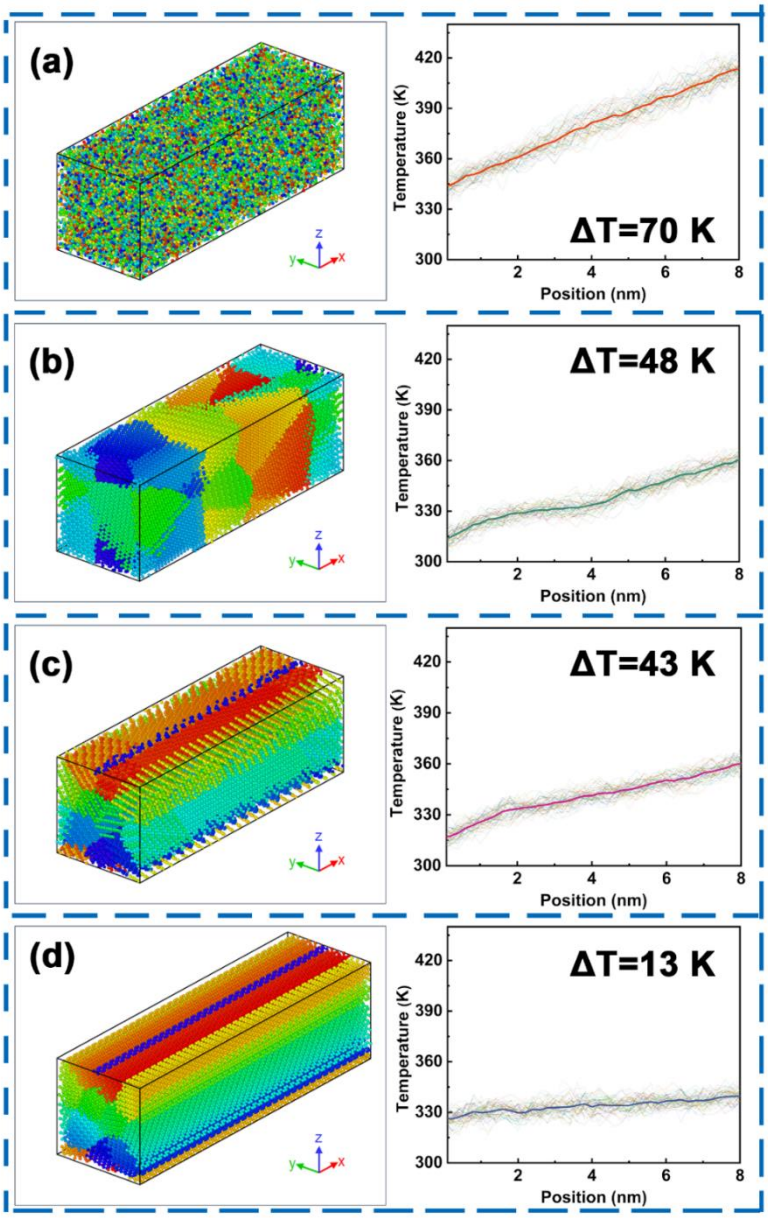

Figure 5.14. Schematic diagrams of four different carbon structures and the average temperature dispersion curves during NEMD simulations and the original curves.

Each simulation cells contain approximately 2300 atoms. All of the atoms were placed in a simulation cell of dimension 50×50×100 Å. These structures are depicted in figure 5.14. The AIREBO potential was used to describe the interaction between carbon atoms. [26] The temperature within the simulation cells was stabilized at 300 K for 25 ps using a canonical ensemble thermostat before inward heat flow allowed from one end of the cell and allowed to flow out from the opposite side of the cell. This phase of the simulation was allowed to run for a simulation time of 500 ps to ensure the simulation reached a steady state. The temperature dispersion for the simulation cells was taken every 0.5 ps during the last 25 ps and recorded to evaluate the thermal transport efficiency. The temperature dispersion curve corresponding to each of the carbon structure is presented on the down side of figure 5.14. The bold curve in every of figure 5.14 is the average temperature dispersion during the recording period. The average temperature dispersions shown together in figure 5.15 for comparison. The temperature difference between the heat source and heat sink in amorphous carbon, spherical crystal carbon, PGVO and PGUO simulation cells are for temperatures of 70, 48, 43 and 13 ^{o}C, respectively. The thermal conductivity is proportional to the inverse to the temperature difference, hence the simulation results suggest that the graphitization effectively enhances thermal conductivity, although it remains overall lower than that of the CFs. The simulations reveal the contribution of the various carbon structures to thermal.

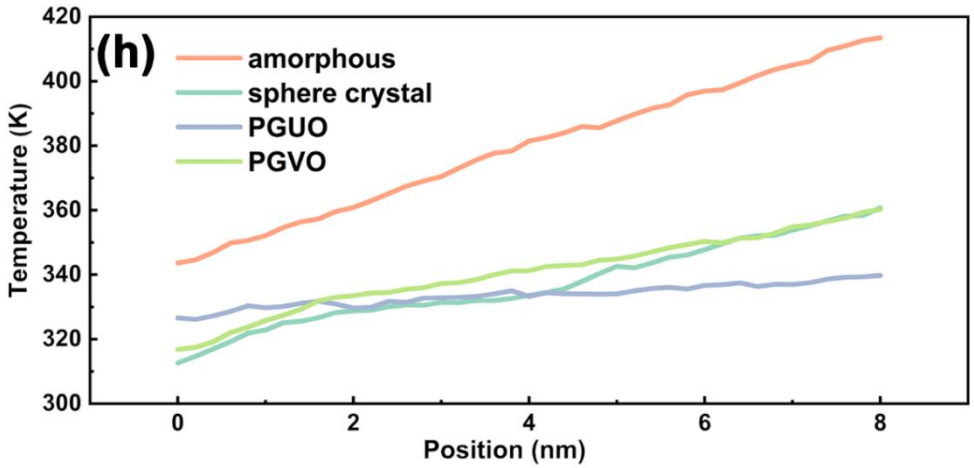

Figure 5.15. The summary of average temperature dispersion curves during NEMD simulations.

As introduced, to perform the Nonequilibrium molecular dynamics, lammps package was applied. In appendix B, the lammps script was posted here as an example for researchers to check and reuse.

5.6 Evaluation of mechanical property

Applied in different environment, materials are required to possess different mechanical property. In last chapter, we introduced the most important mechanical property of TIM, softness. In this chapter, because the preconstructed carbon thermal pass cannot be compressed, TIM is not a suitable application for the composite. However as passaging material, the composite is promising.

As packaging materials, besides high thermal conductivity, it is required to possess proper mechanical properties. For example, a low CTE is needed to avoid thermal stress in the temperature change process. If CTE is high, material tend to expand dramatic in heating process. At 25 ^{o}C, CTE of Si, Al and Cu are about 2.5, 33 and 16.5 ppm K^{-1}. To constrain the thermal stress into an acceptable range, packaging material should

display similar mechanical property. The CTE of epoxy and Lamian-10 in relation to temperature was measured and plotted in figure 5.16. At 30 ^{o}C, the CTE value of epoxy and Lamian-10 were 49.8 ppm K^{-1} and 7.1 ppm K^{-1}. Compared with that of epoxy resin, Lamian-10 have a much more preferred CTE. This value is between CTE of Si, Al and Cu. considering the space relationship of silicon chip, packaging material and heat sink, it is supposed to compromise thermal stress. In order to comprehensively evaluate the thermal conductivity and CTE, I.R. Walker proposed the Thermal Distortion Parameter (TDP) in 2011, which has gradually become a recognized indicator to evaluate the temperature-induced deformation of engineering materials used in electronic packaging.[151, 287-288] TDP is expressed as

$$TDP = \frac{CTE\ (ppm\ K^{-1})}{Thermal\ conductivity\ (W\ m^{-1}\ K^{-1})} \quad (5.16)$$

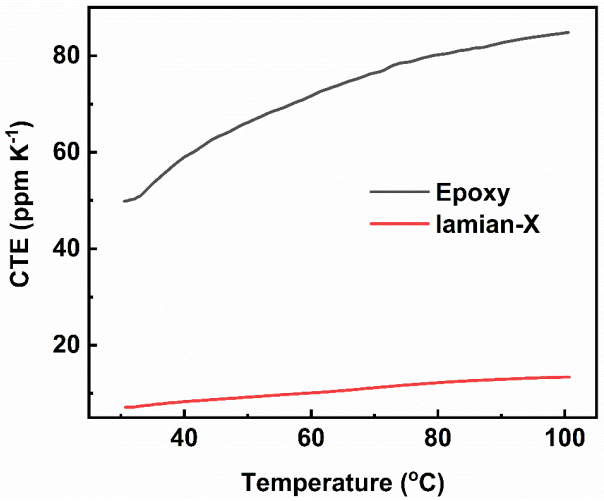

Figure 5.16. The CTE values for epoxy and Lamian-10.

Table 5.3. TDP of related composites, epoxy, and metal compared with Lamian-10.

Material	Thermal Conductivity (W m^{-1} K^{-1})	CTE (ppm K^{-1})	TDP	References
Epoxy	0.19	50	263.1579	/
carbon nanotube/EP	0.29	64.71	223.1379	[289]
AlN/EP	0.507	53.7	105.9172	[290]
Cellulose nanofiber/EP	0.23	23	100.0000	[291]
glass microsphere/EP	0.34	28.72	84.4706	[292]
SiC/EP	0.449	30	66.8151	[151]
Silica/EP	0.6	29	48.3333	[293]
SCAN/EP	1.2	36	30.0000	[293]
Alumina/EP	1.9	38	20.0000	[293]
AlN/SiC/PE	2.25	15.8	7.0222	[294]
CeO2	3.1	19.6	6.3226	[295]
Ti	17	8.9	0.5235	/
Sn	63.2	23.8	0.3766	/
Mg	159	26.1	0.1642	/
Fe	76.2	12.2	0.1601	/
Al	210	25	0.1191	/
Lamian-X	110	7.1	0.0646	/
Ag	419	20	0.0477	/
Cu	385	16.4	0.0426	/
Si	124	2.49	0.0201	/

Low TDP value indicate comprehensive capability as packaging material. Some TDP with ceramic or carbon materials as fillers reported in related studies are summarized and compared with metal, as shown in table 5.3. [151, 289-295] TDP of epoxy samples measured was higher than 200 ppm m W^{-1}. Thanks to the unremitting efforts made by researchers, this value for composite materials is gradually compressed to a few ppm m W^{-1}.

However, these values are still too high to match with metals whose TDP is more than one or two orders of magnitude lower. Compared with previous work on similar materials, Lamian-10 is unique in that its TDP is only 0.0645 ppm m W^{-1}, which is closer to metal than similar carbon-based materials. When used in packaging applications, the low TDP for the Lamian-10 will significantly reduce failure due to metal mismatches at higher temperatures.

Figure 5.17. Samples flow in multilayer solvents with different densities.

At the same time, the material is much lighter than metals. We conducted a simple experiment to explore the density difference between composites and metals, as shown in figure 5.17. Three solutions with different concentrations of 0.86, 1.25 and 1.48 g cm^{-3} were prepared with xylene, Na2WO4 solution and trichloromethane. In order to identify their interfaces, different colors were introduced by dripping specific indicators into solvents. They are then added to a bottle in sequence. Mixing of two organic solvents is prohibited due to the presence of aqueous solution. Then drop Cu, Al, Lamian-10 and epoxy resin into the bottle in turn. Details of this process are given in the support materials. Cu and Al, with densities of 8.9 g cm^{-3} and 2.7 g cm^{-3}, respectively, sank directly to the bottom. Lamian-10, with a density of about 1.4 g cm^{-3}, floats on the interface between Na_2WO_4 solution and chloroform, while epoxy resin

floats on the interface between xylene and Na_2WO_4 due to its lower density. In table 5.4, metals, polymers and CF composites are reviewed and compared with Lamian-10.[253, 255-256, 296-297] From the summary, it is clear that, in broad terms, Lamian-10 has metal-grade thermal conductivity and polymer-grade density, which is a significant improvement over similar materials previously reported.

Table 5.4. Thermal conductivity and density of related composites, epoxy, and metal compared with Lamian-10.

Material	Thermal Conductivity ($W\ m^{-1}\ K^{-1}$)	Density ($g\ cm^{-3}$)	Reference
Ag	419.0000	10.5	
Al	210.0000	2.7	
As	50.2000	5.72	
Au	301.0000	19.3	
Cr	69.1000	7.19	
Cu	385.0000	8.93	
Fe	76.2000	7.87	
Ni	60.7000	8.88	
Sn	63.2000	5.76	
Ti	17.0000	4.5	
PP	0.2000	0.91	
ABS	0.1700	1.07	
PVDF	0.1900	1.78	
PA	0.2100	0.95	
PC	0.2000	1.2	
PBT	0.2700	1.3	
POM	0.1550	1.3	
PE	0.4000	0.95	
PS	0.1600	1.04	
Carbon/carbon	27.45	1.68	[297]

CF/acrylic adhesive	23.3	1.9	[253]
CF/EP	18	1.74	[296]
CF/pCBT	5.2	1.58	[256]
CF/EP	2.21	1.28	[255]

5.7 Conclusion

In conclusion, in this chapter, a Lamian heuristic method to construct CF composites with metal grade thermal conductivity was proposed. Due to the alignment and bridging effect of the thermal conductive filler, the prepared composite possesses a thermal conductivity of 110 W m^{-1} K^{-1}, a density of 1.4 g cm^{-3} and 7.4 ppm K^{-1} CTE. The alignment filling here is achieved by mixing with a viscoelastic medium which is stretched over several cycles. Due to the stretching of the medium, the carbon fibers are aligned in the stretching direction, during which the advantages of carbon fiber as a thermal conductive material can be better utilized. The alignment degree was studied by SEM and micro-CT, and the mathematical model of alignment mechanism was established. The model has enough generality that it can be expected to be applied to most 1D anisotropic fillers. Then, the medium or slurry is graphitized to bridge the carbon fibers, forming a thermal conductivity network and enhancing the heat exchange between the fibers. It is worth noting that the resulting carbon structure has a significant effect on the thermal conductivity, which is analyzed using molecular dynamics simulations. The structural transformation of carbon during graphitization was confirmed by TEM and Raman spectroscopy. The composites synthesized by this method have excellent thermal and mechanical properties and have a wide application prospect in electronic packaging technology.

Chapter 6. Thermal Management Material with High Thermal Conductivity and Phase Change Latent Heat

6.1 Synopsis

In the previous chapters, the thermal conductivity as a core parameter of thermal management material was discussed and developed by adjust the dispersion of thermal conductive fillers. However, as practical thermal management material, some special condition should be considered. For example, the heat overload which is a general condition electronic system suffering which may cause the fluctuation of temperature. The temperature shock can hurt electronic system in short time, so stabilizing temperature is important. Relying on latent heat, phase change material (PCM) can stabilize temperature by absorbing heat when an overload happens and gradually release heat after the overload period. Several phase change materials have been used in this field, including liquid metals and crystalline polymers.[298-300] However, once phase change materials melt, it is not easy to prevent the leakage of resulting liquid.[298] liquid leaking in electronic system is a disaster, because it may pollute the whole system, and can never play its due role. To prevent PCM leakage, researchers developed compensation techniques including microencapsulation, porous materials, nanostructures and embedding PCM into polymer substrates.[301-312]

In this chapter, we will construct a practical thermal management material which was supposed to have good thermal conductivity and phase change latent heat to stabilize temperature during thermal overload. Meanwhile, since the leakage of phase change material is not welcomed, leakage of the milted phase change material should be precluded. But the good news is that, as TIM, PCM is special. Unlike other TIM whose hardness have influence on the ability of heat pass as discussed in Chapter 4, PCM can fill the gaps between heat source and heat sink in the form of gel.

6.2 Preparation of phase change material

The PEG was heated to 70 °C and held for 0.5 h to ensure that all the PEG pieces melt into a transparent liquid. 0.44 g deionized water, 0.03 g ammonium persulfate, 0.07 g BAC and 1.48 acrylic acid was mixed in a high-speed mixer. The solution becomes transparent. 10g of molten PEG and carbon fiber are then mixed into the solution in various proportions using a high-speed mixer. Heat the mixture to 80 ^{o}C and keep it at that temperature for 2 hours. The final product is cooled to room temperature and characterized. The samples were labeled E10A2C3, E10A2C5, E10A2C7 and E10A2C10 according to CF weight. Samples without CF were labeled as E10A2 for reference. All samples were sliced to 1mm thickness. The cooling process may influence the alignment of CFs and furthermore influence the thermal conductivity, which will be discussed. The samples quenched at -24 ^{o}C were labeled as quenched samples while the samples free cooled were labeled as annealed samples. The process is scheduled in figure 6.1

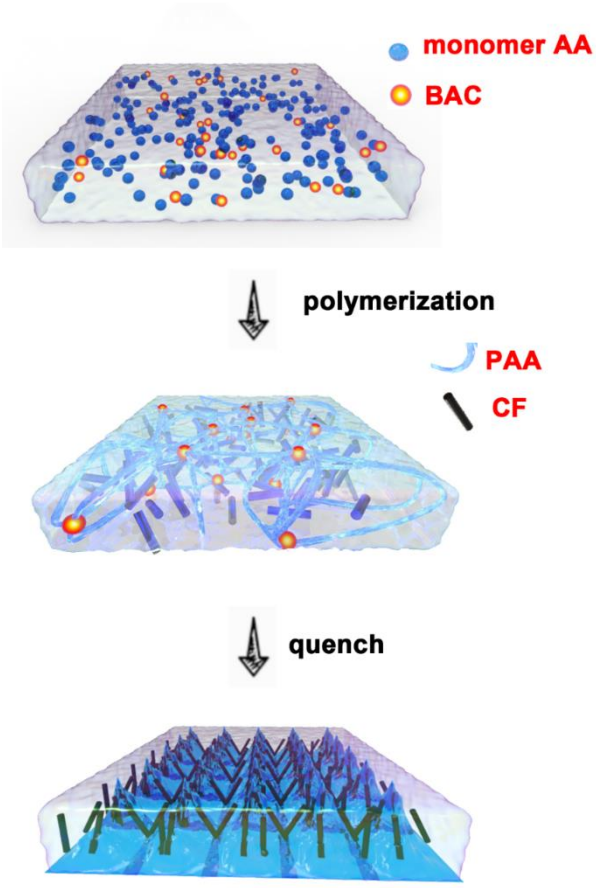

Figure 6.1. Schematic illustration of constructing thermal conductive phase change material.

PAA produced from the polymerization of acrylic acid constructs a soft 3D network with the assistance of BAC, as shown in Fig.1b. The network of PAA cured with the help of BAC has been characterized in previous studies.[313] According to the previous report, BAC was copolymerized into the PAA chain and react as essential coupling reagent. Besides the covalent bonding, hydrogen bonding may play important role in the formation of the network as supposed. Here, we introduced reduce density gradient(RDG) theory to analyze the hydrogen bonding between BAC and PAA.[314] The Gaussian quantum chemistry packaged was applied to determine the molecular orbitals, and then the utility programs Multiwfn and Visual Molecular Dynamics were applied to plot the

hydrogen bonding between molecules as shown in figure 6.2.[315-317] According to Johnson, sign(λ2)ρ is a good indicator of interaction strength.[314] A large, negative values of the parameter indicate attractive interactions such as hydrogen bonding. In Fig.1c, the blue regions demonstrate the attraction between the acid group and amide groups as seen being mediated by the directional hydrogen bonds. The relationship between RDG and sign(λ_2)ρ is plotted in figure 6.3. The simulation result indicates that hydrogen bonds play an essential role in the construction of a 3D network.

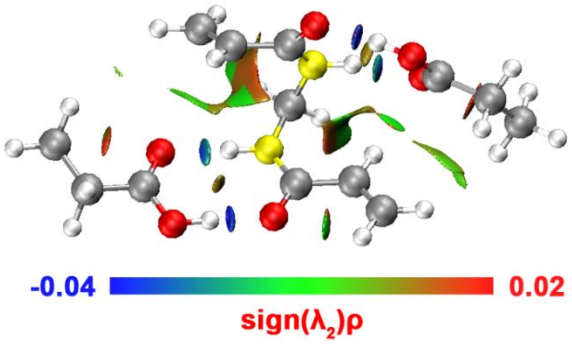

Figure 6.2. The interaction strength between AA and MBA expressed as sign(λ_2)ρ.

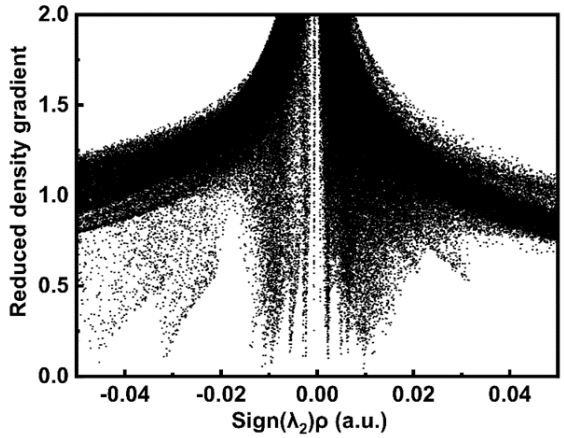

Figure 6.3. Plots of the reduced density gradient versus the electron density

6.3 Characterization of crystal structure

First of all, the phase change process was analyzed. The crystal processes of PEG and E10A2 were observed using a polarizing

microscope. According to the morphology analysis, crystal structure between them have significantly different. Figure 6.4 shows the morphology change during PEG and E10A2 crystallization observed using polarizing microscope. Without PAA, PEG molecules constitute spherical crystals where Maltese cross patterns can be observed. On the other hand, the appearance of PAA provided dispersive nucleation points from which PEG molecules could form polycrystals, only crystals with limited space to grow could be observed. Spherical crystal is constructed by the stacking of lamella crystal according to polymer physics. The morphology of lamella crystals was studied at a smaller scale using AFM. Left side of figure 6.5 shows the height figure of PEG and E10A2 while the right side shows the corresponding phase figure. In AFM images of PEG, lamella crystal shows long-range order, while in that of E10A2 only fragments of crystal could be observed. This phenomenon was also attributed to the nucleation points provided by PAA. The results of the AFM and optical microscope tend to support one another leading to the same conclusion.

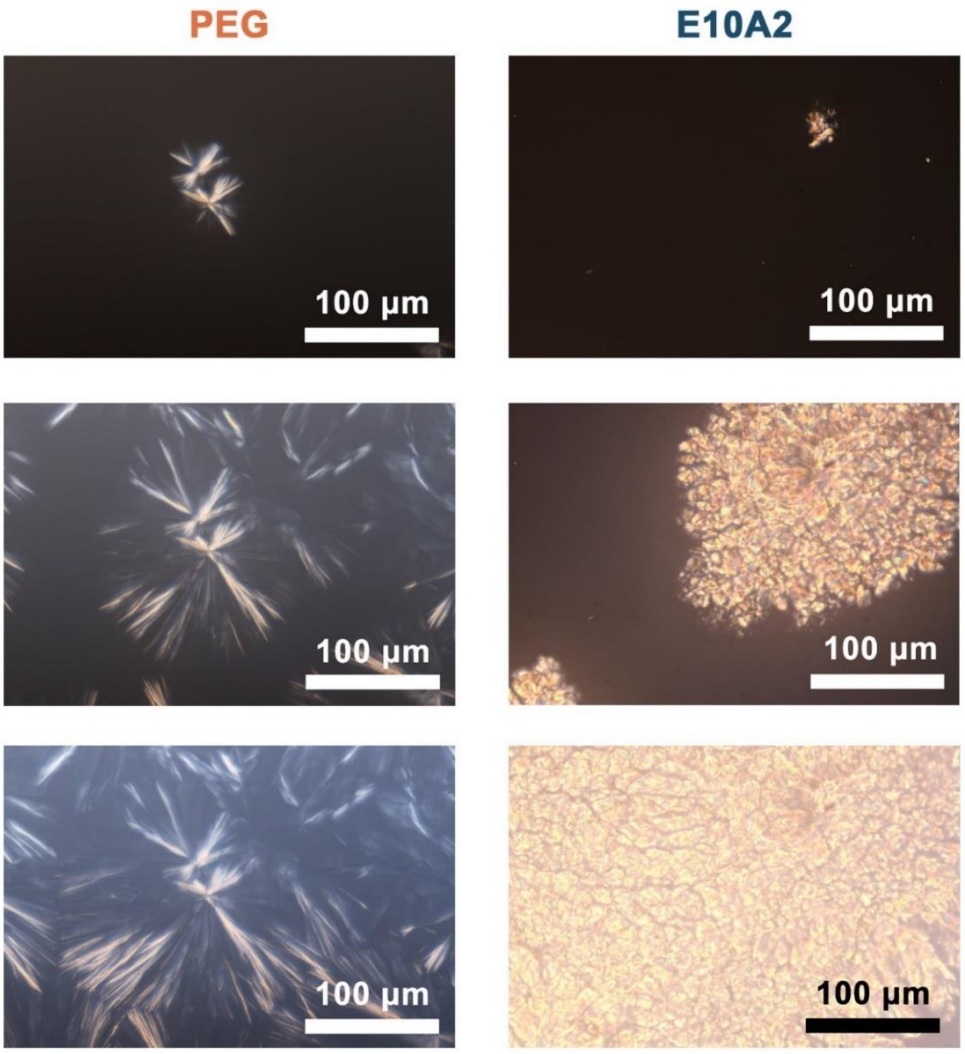

Figure 6.4. Growth of a PEG and E10A2 crystal in.

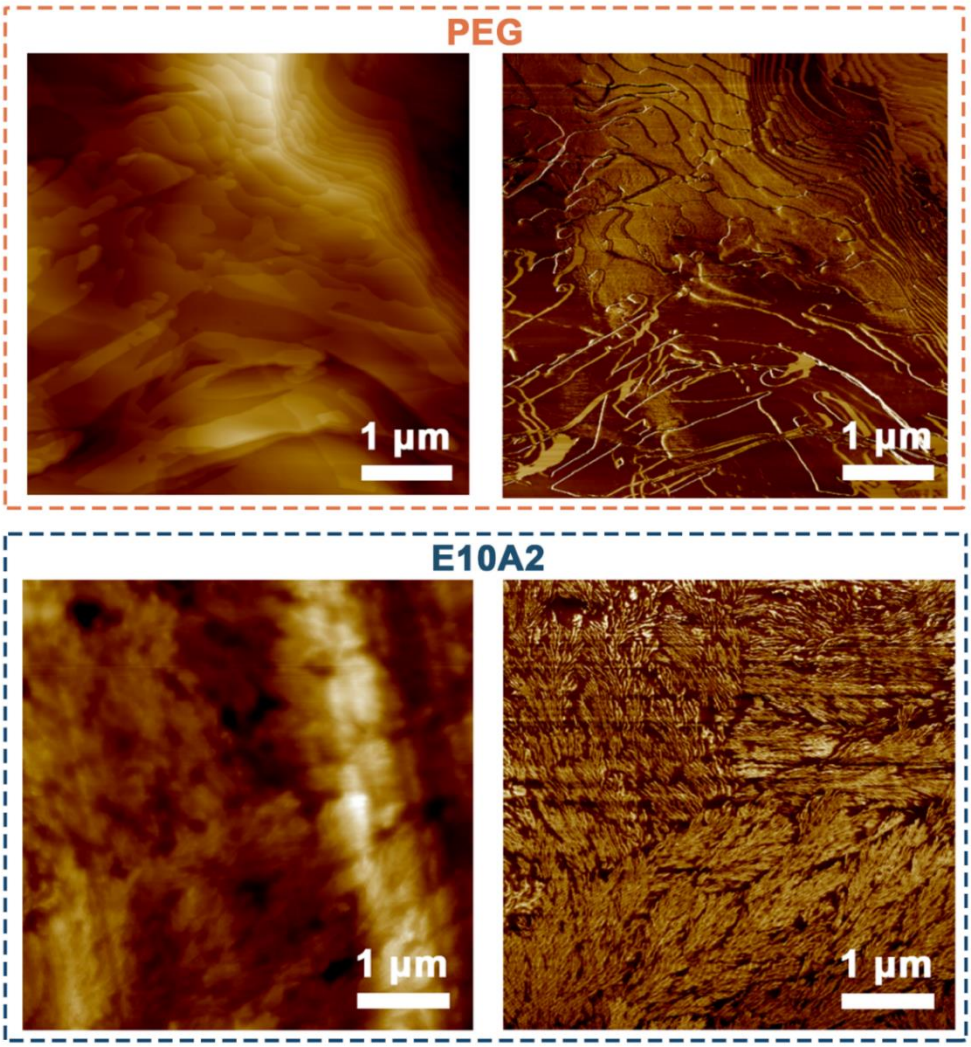

Figure 6.5. AFM image of PEG and E10A2 crystal

Although the long-range crystal structure shows significant change after the introducing of PAA, the parameter of crystal parameter seems not changed a lot according to the XRD spectrum shown in figure 6.6. In both spectra of PEG and E10A2, the band at 19.2^{o} and 23.3^{o} can be observed. Even at the weak peaks including 26.3^{o}, 26.9^{o}, 36.2^{o}, 39.6^{o}, the two spectra give similar details which indicate the similar crystal parameter of the samples.

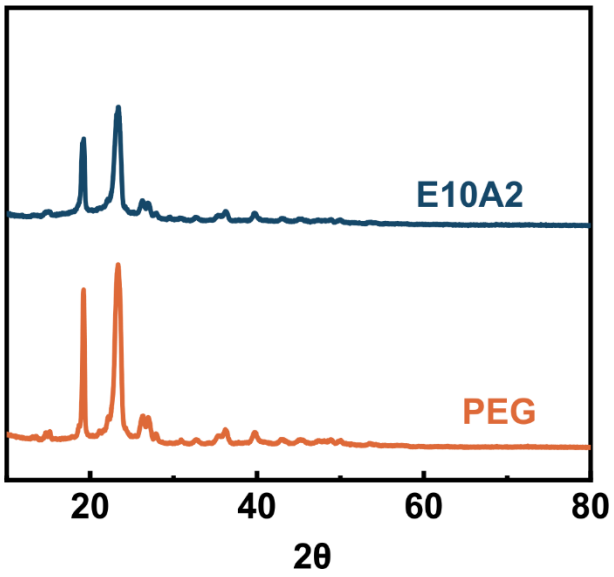

Figure 6.6. XRD spectra of PEG crystal and E10A2 crystal.

6.4 Thermal properties and the structure characterization

Two important properties of thermal management composites are latent heat of phase change and thermal conductivity. DSC was used to evaluate the latent heat of the phase transition by heating the sample beyond the phase transition temperature and measure the heat difference before and after the phase transition. The DSC curve of the obtained sample is shown in figure 6.7(a). With the increase of CF load, the phase transition temperature decreased from 62.4 °C to 56.8 °C. The melting temperature range is related to the CF content, which can accelerate the heat exchange. With the help of carbon fiber, more heat is transported into the sample and stored as latent heat, which lowers the apparent melting temperature of the sample. With the addition of CF, the latent heat of the melting process also decreases, as shown in figure 6.7(b). In the absence of CF loading, the latent heat of E10A2 is 133.5 J g^{-1}. With the addition of CF, the value gradually decreases to 62.0 J g-1 when the loading amount of CF reaches 10 g. The exact values of latent heat of all samples were labeled in figure 6.7(b) on the corresponding

columns. The latent heat would not change a lot during the heating and cooling cycles. 20 heating and cooling cycles was done to prove the statement as figure6.8 shows. In figure 6.8(a), it was depicted that the latent heat of the composite in 20 heating and cooling cycles was stable at about 60 J g^{-1}. The original DSC curve is given in figure 6.8(b). The intensity of red color of background demonstrated the level of temperature, with a maximum at 100 °C. Although the absolute heights of peaks in different cycles are different, latent heats reflected by the area of peaks calculated by integration of power over time are similar.

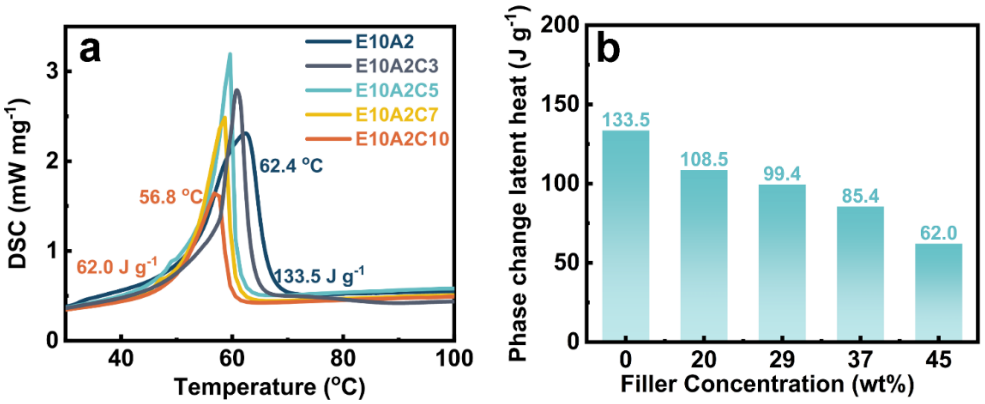

Figure 6.7. (a) DSC curve of samples. (b) Latent heats integrated from the DSC curves.

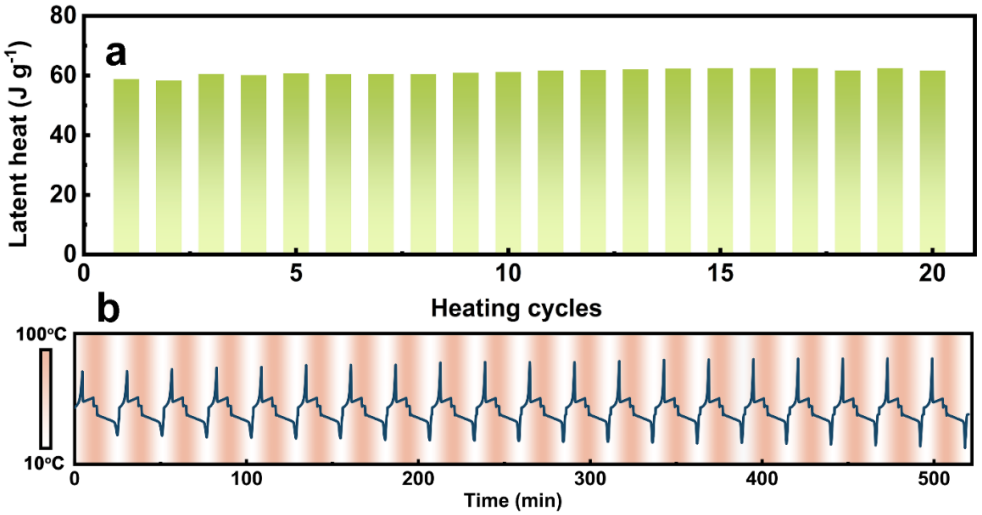

Figure 6.8. (a) Latent heats of E10A2C10 in 20 heating cycles (b) DSC curve during 20 heating cycles.

Although the addition of CF reduces the value of latent heat of phase transition by about 50%, the thermal conductivity increases more rapidly as compensation. The thermal conductivity of annealed and hardened specimens is shown in figure 6.9 and the raw data used to calculate the thermal conductivity were given in table 6.1. It is worth pointing out that since the quenched sample and the corresponding annealed sample are actually the same one but treated by different postprocessing, the densities and Cp values of the corresponding samples where were related only with the constituent of samples, are also the same. Without the addition of carbon fiber, the thermal conductivity is only 0.2 W m^{-1} K^{-1}. This value is in the same order as common polymers such as polyethylene[318], epoxy[135] and PDMS[17]. The thermal conductivity of E10A2C3 can be significantly increased to 8.5 W m^{-1} K^{-1} by loading only 3 g CF. Therefore, about 25% latent heat of phase change is lost; The increase in thermal conductivity offsets the loss of latent heat. With the increase of CF loading to 10 g, the thermal conductivity of E10A2C10 reaches 15.6 W m^{-1} K^{-1}.

Table 6.1. The thermal conductivity and related raw data of samples.

CF concentration (wt%)	**Thermal diffusivity (mm^2 s^{-1})**	**Density (g cm^{-3})**	**Cp (J g^{-1} K^{-1})**	**Thermal conductivity (W m^{-1} K^{-1})**
annealed				
20	4.36	1.34	1.45	8.46
29	5.29	1.31	1.66	11.48
37	6.61	1.37	1.45	13.09
45	7.56	1.46	1.42	15.65
quenched				
20	6.64	1.34	1.45	12.91

29	8.02	1.31	1.66	17.40
37	7.88	1.37	1.45	15.62
45	11.15	1.46	1.42	23.09

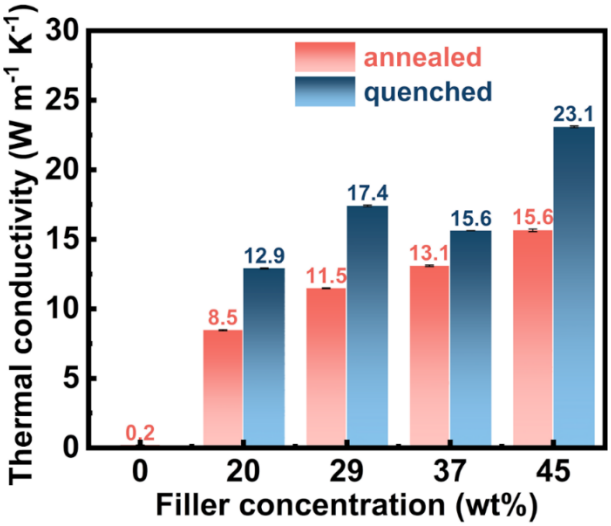

Figure 6.9. Increased thermal conductivity resulted from the larger CF loading. Annealed and quenched samples were tested and are compared in the same figure.

Another attractive phenomenon is that the thermal conductivity is further improved when the sample is hardened at -24 °C. After quenching from 80 to -24 °C, the thermal conductivity of E10A2C3, E10A2C3, E10A2C3 and E10A2C3 increased from 8.5, 11.5, 13.1 and 15.6 W m^{-1} K^{-1} to 12.9, 17.4, 15.6 and 23.1 W m^{-1} K^{-1}, respectively. One possible explanation is suggested. Then sample is quenched at -24 °C, the surface temperature of the hardened sample is expected to drop below the PEG crystallization temperature before the core temperature reaches a similar value. In this case, considering the wide thickness ratio of thin samples, the crystallization process can be considered as starting at the bottom and top and grow towards the center. With the growth of the crystal region, the anisotropic thermal conductive filler rotates vertically and tends to be stable. Conversely, if the sample is cooled to room temperature without

quenching, there is sufficient time to establish an approximately uniform temperature distribution in the sample. If the temperature is kept above freezing or crystallization and the sample cools slowly, the crystals may nucleate throughout the sample, impeding the rotation of CF.

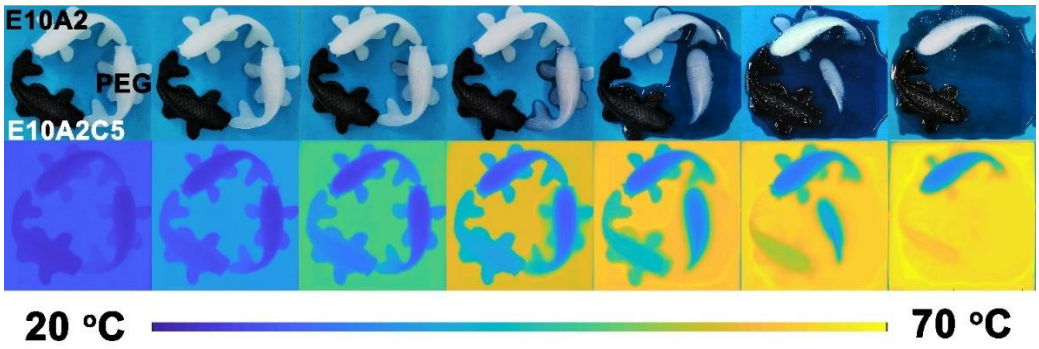

Figure 6.10. Photos and infrared images during eating of three samples made of PEG, E10A2 and E10A2C5.

To show the difference in thermal conductivity of the three materials, fish-shaped samples made of E10A2C5, E10A2 and PEG were placed on the heater. The thermal conductivity and shape stability of infrared images are shown in figure 6.10. As the temperature increases, the PEG fish will melt once the temperature exceeds the melting temperature. On the other hand, E10A2 and E10A2C5 showed shape stability and remained fish-shaped until the end of the test. At the same time, from the different temperatures of E10A2 and E10A2C5, CF is a feasible method to improve the thermal conductivity. Heat is transferred from the sample body in direct contact with the heater. Twenty minutes after beginning to heat, the temperature of E10A2C5 was basically the same as that of the heater, and the temperature of E10A2 was lower. Lower thermal conductivity and the ability of storing latent heat result in slower heat transfer.

When comprehensive compare the latent heat and thermal conductivity

of the composite with previous report, it is special. Previously, thermal conductive PCMs were studied to promote the respond speed of PCM. Researchers want to achieve PCMs responding to temperature fluctuation quickly so that the energy exchange can be finished more efficiently. Base on the requirement, most composites possessed high latent heats while the thermal conductivity were not promoted on a big scale. The maximum value of thermal conductivity was about 6 as table 6.2 shows. The highest thermal conductivity and latent heat in the previous works are only 5.9 W m^{-1} K^{-1} and 202.8 J g^{-1}, respectively. Compare with them, E10A2C10 and E10A2C7 is good at thermal conducting. They exhibit wonderful thermal conductivities which is about 3-4 folds of the best result reported before at the expense of latent heat. In table 6.2, the thermal conductive fillers, phase change materials used in the references, along with the thermal conductivity and latent heat they reached were listed to compare with E10A2C7 and E10A2C10.

Table 6.2. Thermal conductivity and latent heat of previous works and E10A2C10 and E10A2C7.

Thermal conductive fillers	Phase change materials	Thermal conductivity (W m^{-1} K^{-1})	Latent heat (J g^{-1})	Reference
RGO/GNP	1-octadecanol	5.92	202.8	[305]
GO	PEG	0.6	174.9	[319]
MXene	PEG	0.471	126.4	[320]
MWCNTs	paraffin	1.3	126.3	[321]
CNTs	PEG	0.5	85.9	[322]
GO	PEG	2.02	145.5	[323]
RGO/TiO2-x	paraffin	1.22	110	[307]

CF	PEG	15.6	85.38	E10A2C7
CF	PEG	23.1	62	E10A2C10

As we have done in previous chapters, SEM and micro-CT will be used to evaluate the alignment of fillers. From the SEM image of sample E10A2C10 who exhibits the best thermal conducting property, If the sample was annealed to room temperature after curing, the alignment of CFs was random. On the contrary, if then the sample was heated beyond the milting temperature, and quenched at -24 ^{o}C, the CFs would tend to align on the direction perpendicular to the surface. This structure transfer can explain the rise of thermal conductivity after quenching and verify our assumption about the alignment of CFs.

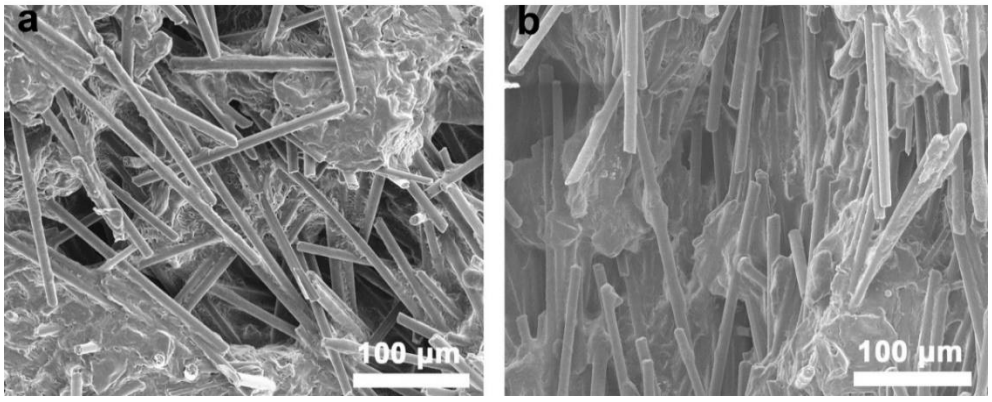

Figure 6.11. Morphology of E10A2C7-annealed and E10A2C7-quenched (a) SEM image of annealed sample E10A2C7-annealed. (e) SEM image of quenched sample E10A2C7-quenched.

Similar analysis on micro-CT result can be found in chapter 4. Similar schematic was given in figure 6.12(a). The probability versus degree summarized from micro-CT is plotted in figure 6.12(b). Here it worth to explain that the absolute probability value in the figure is related to the resolution of element angle. Since the integration of the probability over angle is 1, the bigger the element angle is, the lower the probability is. It

can also be understood from another perspective. When the element angle shrinks, the probability of a point fall in the element angle would go down. However, the resolution of angle has no influence on the analysis of alignment. The original micro CT figure of E10A2C10 before and after quenching were plotted in figure 6.12(c,d) respectively where different colors were mapped with φ, the angle between the through plane direction and the corresponding CFs. The hot color reveals a big φ while the cold color reveals small one.

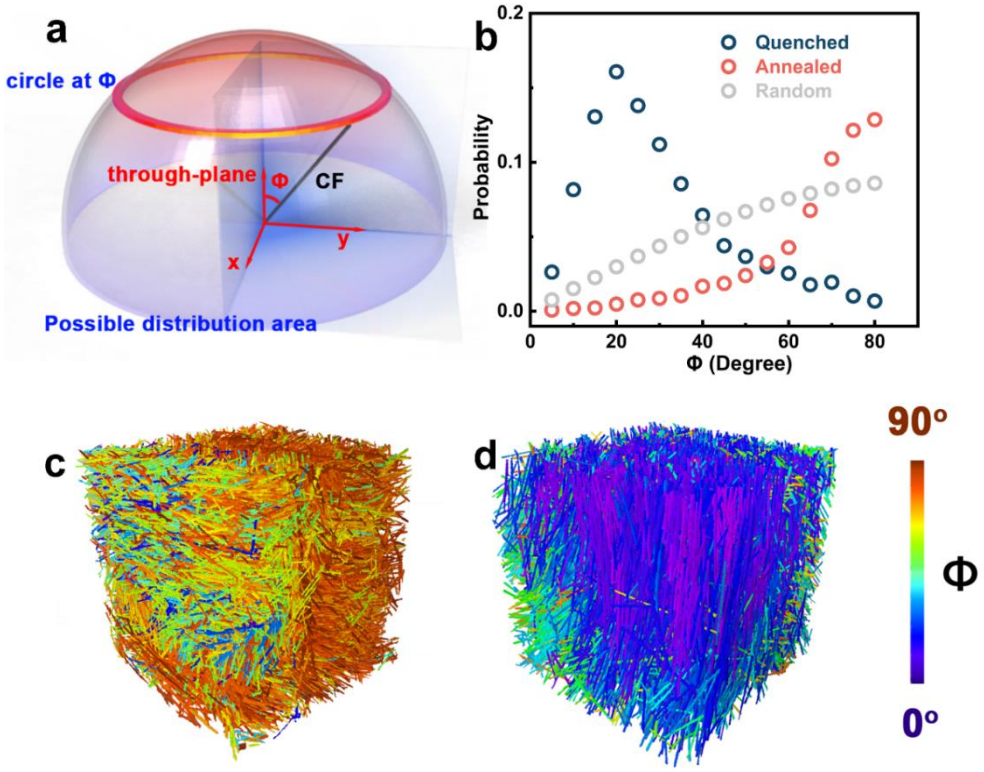

Figure 6.12. Alignment analysis of fillers in composites. (a) Schematic of Φ which was the angle between CF and through-plane direction. (b) Dispersion of CF in different Φ ranges. (c) Micro-CT of CF as filler in composites E10A2C7- annealed. (d) Micro-CT of CF as filler in composites E10A2C10-annealed.

6.5 Evaluation of mechanical property

Mechanical properties were evaluated in this subchapter. First, the stress-strain curves of representative samples were showed in figure 6.13. From the comparation between stress-strain curves, it can be seen that with the appearance of PAA and CF, the breaking elongation was immediately promoted. This is attributed to the PAA network which can effectively influence the crystal of PEG. As discussed, the PAA network can convert the spherical crystal of PEG into small pieces. Compressing the crystal size is a general method to promote the plasticity of material. This phenomenon is explained in polymer physics. Meanwhile, it can be clearly seen that with the rise of CF concentration, the material was enhanced.

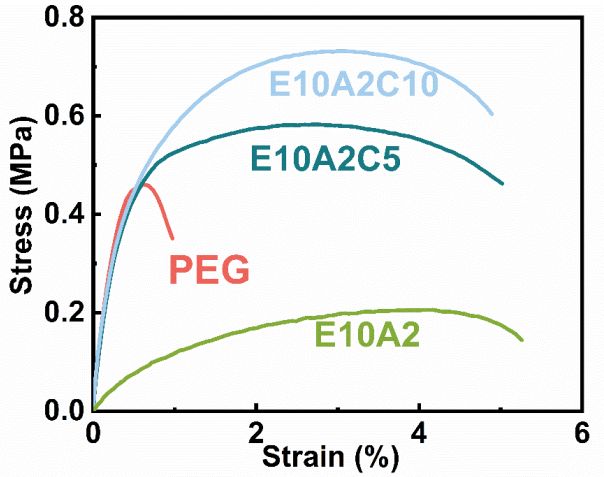

Figure 6.13. The stress-strain curve for the samples. (b) The photo of the custom-made equipment used in the test.

Table 6.3. The mechanical property of samples

	Young modulus (MPa)	elongation at break (%)	Tensile Strength (MPa)
PEG	1.13	0.97	0.46
E10A2	0.09	5.26	0.21
E10A2C5	0.97	5.02	0.58
E10A2C10	1.02	4.89	0.73

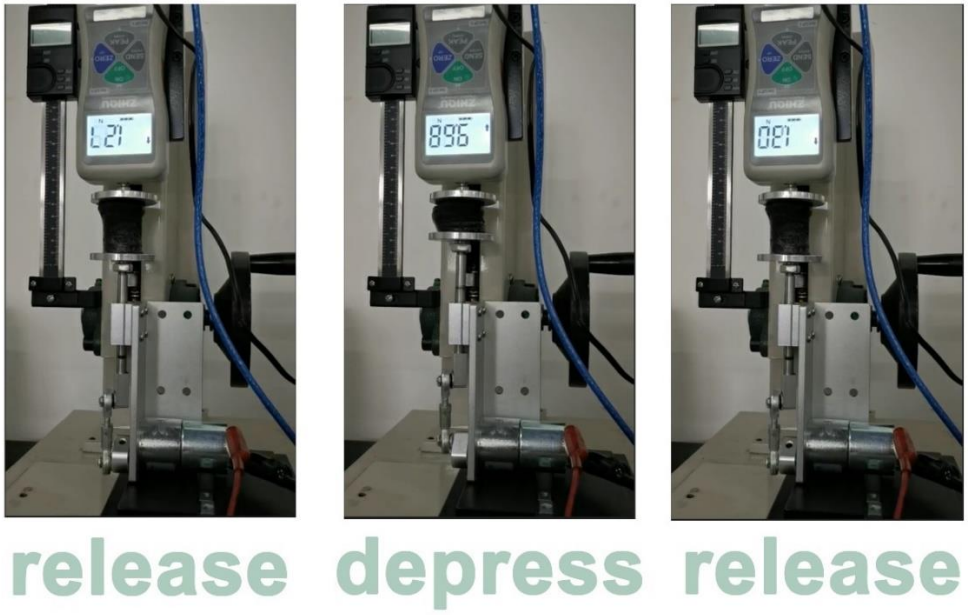

Figure 6.14. The photo of the custom-made equipment used in the test.

Mechanical properties at high temperature especially beyond the milting temperature is essential for PCM in application. It was evaluated using custom-made instruments whose photo was shown in figure 6.14. Combine pressure sensor and reciprocating device. The stroke displacement of the reciprocator is 16 mm, and the maximum distance between the sensor and reciprocator is 40 mm. The sample was made into a cylinder with a diameter of 30 mm and a height of 40 mm, and then mounted in the gap between the sensor and the reciprocator. During the experiment, a heat gun was used to keep the temperature of samples between 60-70 ^{o}C. Using a reciprocator, the sample is pressed down and released, as shown in figure 6.14. Pressure sensors recorded pressure data in 500 pressure cycles. E10A2 and E10A2C3 were evaluated in the experiment. Figure 6.15 shows the results. In 500 pressure cycles, both samples show good mechanical stability. The pressure detected during depressing and releasing barely dropped. By comparing the force data

of E10A2 and E10A2C3, it can be determined that the compression modulus above the melting point temperature increases when CF is added. To make the data clear, the curves in first and last 10 cycles compressing was magnified and shown in figure 6.15(b,c).

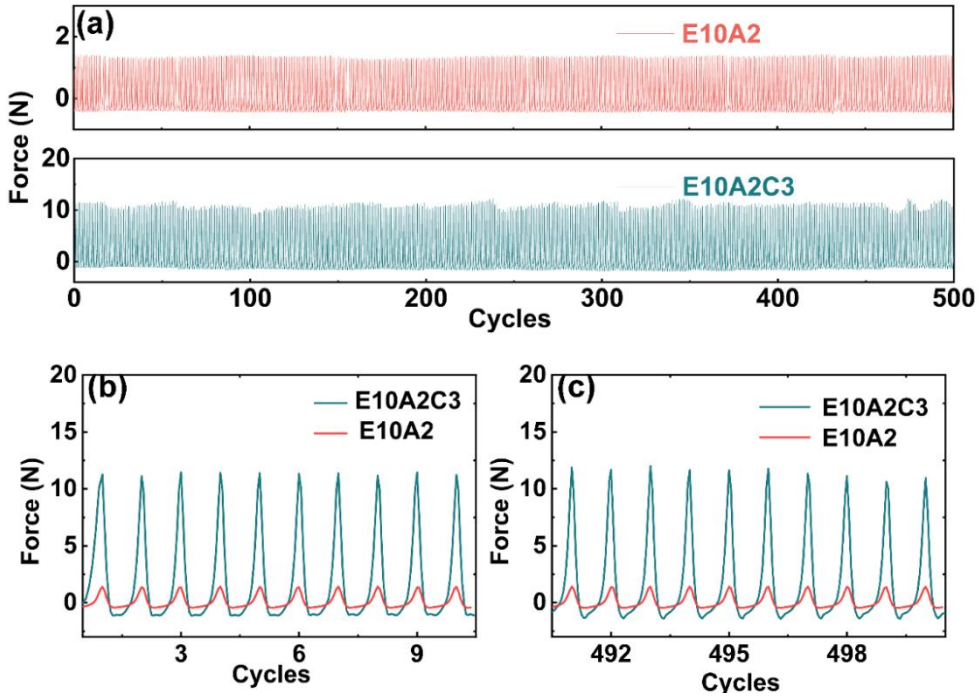

Figure 6.15. The force data obtained during 500 compression cycles. (a) the survey image of the force curve during 500 compressing cycles (b) The force data measured during the first ten compressing cycles. (e) The force data measured during the last ten compressing cycles.

To visualize the differences in thermal management ability of materials, PEG, E10A2 and E10A2C10 samples were molded into lion shapes and heated in 80 oC oven, and then compared with each other. The initial photo at t = 0 min is shown in figure 6.16. After heated 30 min, pure PEG molded lions cannot maintain their structure and the surface details disappeared. After two hours, only liquid PEG is left. E10A2 retains the outline of the lion, but because the sample is soft, the lion cannot stand on its own. The softness of E10A2 at high temperature is proved in the

compressing experiment. For E10A2C10, because CF strengthen the composite at high temperature, the lion can still maintain its shape at 80℃ during the whole experiment.

Figure 6.16. The molded lions made of PEG, E10A2 and E10A2C10 heated at 80 oC for different durations. The photos were taken at 0, 30 and 120 min, respectively.

The application of PCM is carried out. Place the E10A2 and E10A2C7 boards on the core of a dual-CPU server, replacing the standard radiator. The picture of the device is shown in figure 6.17. E10A2C7 is coated on core 1 and E10A2 is coated on core 2. Fluke infrared camera was used to monitor and record the temperature of the two cores during the power-on process (figure 6.17 (b)). The infrared images were shown in figure

6.17(c). As can be seen from the temperature of the infrared image, the temperature of nucleus 1 is lower than that of nucleus 2. During this process, the maximum temperatures of the first and second cores at 95 s are 66 and 73 ºC, respectively. The difference in temperature results from the difference in thermal conductivity of the two materials. When the temperature is around 60 ºC, the heat can be stored as latent heat, which inhibits the temperature rise of the two cores. Once the temperature exceeds the melting temperature, the temperature of core 2 rises rapidly in the absence of phase change materials. In figure 6.17(b), when the temperature exceeds the melting temperature of the sample, the temperature of core 1 rises more slowly than that of core 2, which is due to the filling of high thermal conductivity filler.

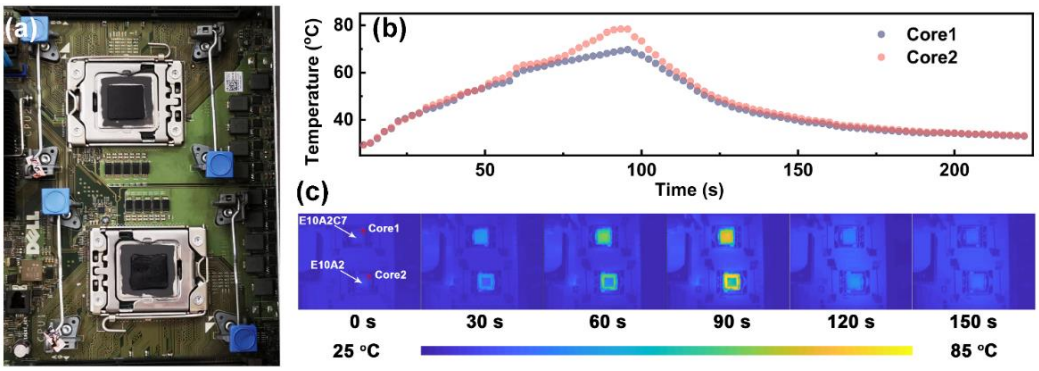

Figure 6.17. An application of PCM samples (a) The Server CPU cores with heat sinks replaced by E10A2C7 and E10A2. (b) Temperature of the cores during a power on process. (c) Infrared images of server cores following power on process.

6.6 Conclusion

In conclusion, a kind of composite material with good thermal conductivity, temperature stability and shape stability were prepared. The increase in CF load results in an increase in thermal conductivity. When CF loading is 10 g, the thermal conductivity of the composite is 23.1 W m^{-1} K^{-1} and

quenched at -24 ^{o}C. Under the same conditions, the latent heat of phase change matrix is 62.0 J g^{-1}. The sample proposed in this study has better thermal conductivity and comparable latent heat compared to the thermal PCM as reference material. In addition to their excellent thermal management properties, their mechanical properties, including shape stability, were also studied. The addition of PAA improves ductility at the expense of Young's modulus. The addition of CF can restore the modulus to the level of PEG sample while maintaining good ductility.

An exciting concept was developed in this work to use PCM instead of ice as template alignment filler, providing a practical route to simplify the process and introduce new features. SEM and Micro-CT results confirmed the arrangement of fillers. Due to the importance of anisotropic filler materials in composites, it is reasonable to expect that this method can be used to successfully customize the thermal and mechanical properties of composites in the future.

Chapter 7. Conclusion and Future Work

Milled carbon fiber is a general used filler for constructing thermal conducting composites. The focus of this thesis is on constructing CF thermal management composites with high thermal conductivity in a specific direction with the assistance of mechanical methods. Besides the high thermal conductivity, different mechanical properties were studied to adapt the composites to a different application.

7.1 Contributions of the thesis

The major contributions of this thesis are:

- Studied the morphology, the alignment of change of carbon fiber under pressure and stress.
- Constructing carbon fiber composites with high thermal conductivity along specific direction.
- Analyze the relationship between the alignment and thermal conductivity with finite element analysis.
- Constructing practical phase change composite with high thermal conductivity.

7.2 Investigation conclusion

7.2.1 Stress inducing CF orientation enhanced thermal conductivity of epoxy composite

The waste heat is now a hinder to the development of integrated

semiconductor devices because of its negative influence on performance, service life and stability of the electronic system. Lot solutions have been proposed based on novel thermal conductivity materials. In this study, carbon fibers used as fillers can extremely enhance the thermal conductivity of epoxy composites. Carbon fibers possess an intrinsic thermal conductivity reaching up to 900 W m^{-1} K^{-1} along the axial direction, while in the radial direction, that value dives to below 20 W m^{-1} K^{-1}. Because of the anisotropic thermal conductivity, the orientation of carbon fibers is supposed to facilitate the thermal conduction of composite.

High thermal conductivity epoxy resin composites were prepared by stress - induced orientation method. Compared with the existing one-dimensional filled composites, the thermal conductivity of s-CF/epoxy resin reaches 32.6W m^{-1} K^{-1} under the condition of 46% CF filling. A new record 14,650% increase in thermal conductivity was reported. The main reason for this high value is that the orientation of the carbon fibers along the through-plane direction and the direct connection network between the carbon fibers establish an effective thermal path. In addition, the influence of the orientation of carbon fibers on thermal conductivity was confirmed by finite analysis and micro-CT statistics. Because the stress orientation is compatible with the standard industrial process, this method has obvious advantages and great potential in the development of high thermal conductivity composites by constructing filler frames and has a wide application prospect.

It is worth pointing out that in this chapter, we set up a mathematical model preliminary to analyze the alignment of one-dimensional fillers by transferring the dispersion of filler to the dispersion of the end. The

propounded formula, especially the formula describing random dispersion of fillers, can be found throughout the thesis.

7.2.2 Synergistic effect of CF and graphite under stress constructing TIM with low thermal resistance

Thus far, we know that stress can help to align anisotropic filler and explain why the method may make more contributions to two-dimensional fillers. The method was applied to the alignment of graphite. By aligning graphite with the entire plane, TIM achieved a bulk thermal conductivity of 34 W m^{-1} K^{-1}, 18,607% higher than that of pure silicon. While this value is attractive, the thermal contact resistance is still too high to be used as TIM because its rough surface makes effective thermal coupling challenging. A 3D profilometer was introduced to prove the hypothesis that the gap between the graphite flakes caused the surface roughness. When CF is used to fill the void, the thermal resistance can be reduced at the expense of the thermal conductivity of the body, making the interface smooth. When graphite ratio CF = 1, the thermal resistance can be reduced to about 2.1 × 10^4 K m^2 W^{-1} under the action of 30 psi at 80 °C, but the thermal conductivity is mostly slightly reduced to 14.3 W m^{-1} K^{-1}. The resulting TIM sample has obvious advantages in applications requiring sufficient softness, proper compressibility and strong heat conduction.

Then the coupling agent was applied in the synthesis of the thermal management composite. With the assistance of a coupling agent, the thermal resistance of the TIM is suppressed to 1.8 × 10^4 K m^2 W^{-1} while the thermal conductivity is promoted to 19.1 W m^{-1} K^{-1}. The phenomenon was explained by the enhancement of interaction between thermal

conductive filler and matrix.

We analyzed the thermal conductivity using finite element analysis as in the previous chapters. Using a random number generator, we can generate the coordinate and rotation angle of random dispersed CFs in the composite. What should be carefully treated if one wants to use the method is pointed out. The first is to avoid the overlap of fillers. To avoid the overlap, the distance between segments should be calculated. If the value is smaller than the diameter, the CF can be retained. The second is the calculation of the thermal conductivity tensor. The default position of CF is along the z-axis, in which direction thermal conductivity is 900 W m^{-1} K^{-1}. With the rotation of filler, the best thermal conductive direction rotates to a new direction, which causes the change of thermal conductivity tensor in the universal coordinate system.

7.2.3 The achievement of metal-level thermal conductivity by aligning CFs with the help of stretching medium

A Lamian heuristic method for constructing metal grade heat-conducting CF composites is presented. Due to the orientation and bridging effect of the thermal conductivity filler, the thermal conductivity of the composites is 110 W m^{-1} K^{-1}, the density is 1.4 g cm^{-3}, and the density is 7.4 ppm K^{-1} CTE. The alignment filling here is achieved by mixing with a viscoelastic medium which is stretched over several cycles. Due to the stretching of the medium, the carbon fiber is arranged along the stretching direction so that the advantages of carbon fiber as a thermal conductivity material are better utilized. The collimation degree of the collimating mechanism was studied by means of SEM and micro-CT (Micro-CT), and the mathematical model of the collimating mechanism was established. Then,

the medium or slurry is graphitized and the carbon fibers are bridged to form a thermal conductivity network and enhance the heat exchange between the fibers. Notably, the resulting carbon structure has a significant effect on thermal conductivity, which was analyzed using molecular dynamics simulations. The structural transformation of carbon during graphitization was confirmed by TEM and Raman spectroscopy. The composites synthesized by this method have excellent thermal and mechanical properties and have broad application prospects in electronic packaging technology.

In this chapter, the mathematical model was proposed to describe the alignment of a one-dimensional filler during the stretching of the medium. Furthermore, based on the model, thermal conductivity change during the stretching can be analyzed. According to the model, before the strain goes beyond 10^3 %, the thermal conductivity increases sharply. And after the threshold value, thermal conductivity stabilizes at a specific value which may be related to the thermal conductivity of filler, interaction between filler and matrix and the special structure. This result matches the measurement result and so gets proved.

$$\frac{k_{stretch}}{k_{CF}} = c \cdot \cos[\arctan(\frac{\tan\theta_0}{\sqrt{1+\frac{Vt}{L}}})] \quad (7.1)$$

$$\theta_0 = 1 \quad (7.2)$$

At a smaller scale, to describe the influence of carbon structure transform, LAMMPS package was introduced to perform molecular dynamic analysis. According to the analysis, graphitization can substantially promote the thermal conductivity because of the transformation of the carbon structure.

7.2.4 Thermal management material with high thermal conductivity and phase change latent heat

A kind of composite material with good thermal conductivity, stable temperature and stable shape was prepared. The increased CF load increases the thermal conductivity. When CF loading is 10 g, the thermal conductivity of the composite is 23.1 W m^{-1} K^{-1} and quenched at -24 ^{o}C. Under the same conditions, the latent heat of the phase change matrix is 62.0 J g-1. Compared with thermal phase change materials as reference materials, the samples proposed in this study have better thermal conductivity and comparable latent heat. In addition to their excellent thermal management properties, their mechanical properties, including shape stability, were also studied. The addition of PAA increased ductility but decreased Young's modulus. The addition of CF can restore the modulus to the level of the PEG sample while maintaining good ductility.

Meanwhile, an exciting concept was developed to use PCM instead of ice as template alignment padding, providing a practical route to simplify the process and introduce new features. SEM and micro-CT results confirm the packing arrangement. Due to the importance of anisotropic filling materials in composites, it is expected that this method can be successfully used to customize the thermal and mechanical properties of composites.

7.3 Potential future work

With the development of electronic equipment, the requirement for thermal management material with higher thermal conductivity and specific mechanical properties will become more urgent. In conjunction with the increasing desire for a solution to waste heat in various

applications, there remain many challenges and opportunities for the future improvement in novel and functional thermal management composite with higher thermal conductivity. In all strategies, mechanical assisted alignment of fillers is proved a promising one. This project would benefit from the further studies:

There are some assumptions we made in the thesis need more direct evidence to support. For example, in chapter 3, it is said that the attachment of carbon fiber can enhance the thermal exchange between them. This assumption is common in this field, although it is short of experimental evidence. Limited by measurement method, we followed the assumption and deeply hope the following researcher can get more evidence. Another example is the form of thermal conductivity. The statement we made in chapter 2 said that the thermal conductivity should be expressed as a tensor, however limited by measurement method we focus on the through plane component which is a scalar. In the future, with the development of measurement, hope we can measure the thermal conductivity tensor and more details can be studied.

It is hard to study all parameters and influences in one thesis. There are some parameters may be optimized. For example, in chapter 6, we used PEG with 2000 molecular weight ignoring the influence of molecular weight on thermal conductivity. In the future, experiments can be done to investigate the relationship between thermal conductivity and the molecular weight. And in some chapters, we evaluated the mechanical properties using hardness, depress cycles. Besides them, stress-strain curve is a good choose which can give modulus, elongation at breaking and yield strength. In the future, hope we can get the curve to refine the

work.

Besides carbon fibers, there are some other thermal conductive fillers including carbon nanotube, boron nitride nanotube. Although, this thesis majorly focuses on the alignment of carbon fiber, the methods posted in the thesis maybe also applicable on these fillers. In the future, it worth to investigate the potential of these methods on aligning other 1D materials.

As introduced, the thermal conductivity of anisotropic thermal conductive filler should be expressed as a tensor. In our study, once the composited solidified, the thermal conductive tensor becomes constant. However, during the operation of the electronic system, the tasks shouldered by elements are flexible, which causes the position of the heat source during the process to fluctuate. To exploit the full potential of the thermal conductive fillers, a more intellective material which can rotate the fillers toward the heat source during the operation was supposed. Hopefully, the structure optimization of intellective material can be achieved without manual intervention. As a result, measured thermal conductivity may not change, but the usage of filler and heat transport will be more efficient.

Another possible development direction is combining the attitude adjustment of filler and molecular simultaneously. The mechanical method was proved effective in the alignment of polymer molecular chains in the past few years. And we have proved the feasibility of aligning fillers with a mechanical method. It is reasonable to believe that the alignment of carbon fibers and polymers chain can be achieved simultaneously. It is worth expecting the coupling effect of the two materials on thermal conduction.

As this study considered only the basic property of composites, the specific design and processing requirements in material substitution have to assess in more detailed feasibility studies. On specific electronic equipment, including details such as ageing properties in special environment (anti-oxygenation, Thermal ageing property, corrosion resistance, etc.), environmental-friendly performance (recyclability, toxicity, etc.), special limitation on the material (limited space, restrictions on mass, etc.) and processing performance (fluidity, etc.) should be considered for realistic application. In Chapter 6, we have tried to endow the composite with phase change function, although there are lot details can be polished to refine the work. For example, more samples should have been placed on the server CPU cores so that we can get more details in the comparation between samples. In the future, hope we will have chance to refine the works.

Considering applications of thermal management materials, not restricted to electronic equipment, future research could evaluate in more detail for wide applications of thermal management materials, such as aerospace, architecture and sporting industries. Vary strategies may be applied to adjusting composite structure to harvest diversiform functions and higher thermal conductivity so that the materials can adapt to the flexible application.

Appendix A

No_cross_lines_and_donot_cross_plane.m

```
A=[];%%The array of first end of CF
B=[];
C=[];
QX=[];;%%The array of second end of CF
QY=[];
QZ=[];
NX=[];%%The array of direction vector of CF
NY=[];
NZ=[];

AA=[];%%The array of Thermal conductivity tensor in universal
coordinate system
AB=[];
AC=[];
BB=[];
BC=[];
CC=[];

L=5;%%Length of CFs
SIZE=10;%Simulation box size
D=0.2;%%Diameter of CF
k=1;%%Counter
Tcx=10;
```

```
Tcy=10;
Tcz=900;

%% This part of code is to generate the coordinate and the
rotation angle of CFs. Meanwhile, the CFs are confirmed not
overlap.
for r=1:100000
    mark=1;
    a=rand*SIZE;
    b=rand*SIZE;
    c=rand*SIZE;
    nx=rand*2-1;
    ny=rand*2-1;
    nz=rand*2-1;
    q=line_turnaround_2(nx,ny,nz,L);
    if
((a+q(1)<SIZE)&&(a+q(1)>0))&&((b+q(2)<SIZE)&&(b+q(2)>0))&&(
(c+q(3)<SIZE)&&(c+q(3)>0)) &&((((q(2)+b<4.9)
&&(b<4.9))||((q(2)+b>5.1) && (b>5.1)))
||distance_between_point_line([a,b,c],[a+q(1),b+q(2),c+q(3)],[5,5,5
])>5.5)

        if length(A)==0
            A(k)=a;
            B(k)=b;
            C(k)=c;
            QX(k)=q(1);
            QY(k)=q(2);
```

```
        QZ(k)=q(3);
        NX(k)=nx;
        NY(k)=ny;
        NZ(k)=nz;


RESULT=turn_around_Tc(nx,ny,nz,Tcx,Tcy,Tcz);%%Calculate
the thermal conductivity tensor in universal coordinate system.
        AA(k)=RESULT(1);
        AB(k)=RESULT(2);
        AC(k)=RESULT(3);
        BB(k)=RESULT(4);
        BC(k)=RESULT(5);
        CC(k)=RESULT(6);

        continue
    end

    if length(A)~=0
        for i=1:length(A);
            Q1=[A(i),B(i),C(i)];
            Q2=[A(i)+QX(i),B(i)+QY(i),C(i)+QZ(i)];
            P1=[a,b,c];
            P2=[a+q(1),b+q(2),c+q(3)];
            d=distance_between_two_line(Q1,Q2,P1,P2);
            if d<D
                mark=0;
                break
```

```
            end
        end
        if mark==1
            k=k+1;
            A(k)=a;
            B(k)=b;
            C(k)=c;
            QX(k)=q(1);
            QY(k)=q(2);
            QZ(k)=q(3);
            NX(k)=nx;
            NY(k)=ny;
            NZ(k)=nz;


RESULT=turn_around_Tc(nx,ny,nz,Tcx,Tcy,Tcz); %%Calculate
the thermal conductivity tensor in universal coordinate system.
            AA(k)=RESULT(1);
            AB(k)=RESULT(2);
            AC(k)=RESULT(3);
            BB(k)=RESULT(4);
            BC(k)=RESULT(5);
            CC(k)=RESULT(6);


        end

    end
end
```

```
    if k==85
        break
    end
end
```

Turn_around_Tc.m

```
function RESULT=turn_around_Tc(x,y,z,Tcx,Tcy,Tcz)
CosA=zeros(3);
coordinate=[x*z,y,x;y*z,-x,y;-x*x-y*y,0,z];
abs_coordinate=[1,0,0;0,1,0;0,0,1];
for i=1:3
    for j=1:3

CosA(j,i)=dot(abs_coordinate(:,j),coordinate(:,i))/(norm(coordinate(
:,i))*norm(abs_coordinate(:,j)));
    end
end

M=[Tcx,0,0;0,Tcy,0;0,0,Tcz];
Tc=CosA*M*CosA.';
RESULT=[Tc(1,1),Tc(1,2),Tc(1,3),Tc(2,2),Tc(2,3),Tc(3,3)];
```

Distance_between_point_line

```
function d=distance_between_point_line(p1,p2,point)

d = norm(cross(p2-p1,point-p1))/norm(p2-p1)%%Distance
between point and line
k=-sum((p1-point).*(p2-p1))/sum((p2-p1).^2)
o=[k*(p2(1)-p1(1))+p1(1),k*(p2(2)-p1(2))+p1(2),k*(p2(3)-
p1(3))+p1(3)]%%pedal of point on the line
res=(o-p1)/(p2-p1)
if res<0
   d=sqrt(sum((p1-point).^2))
end
if res>1
   d=sqrt(sum((p2-point).^2))
end
end
```

distance_between_two_line

```
function d=distance_between_two_line(p1,p2,q1,q2)
s1=p2-p1;%%Direction vector
s2=q2-q1;
res1=((s1*s2')*((p1-q1)*s2')-(s2*s2')*((p1-
q1)*s1'))/((s1*s1')*(s2*s2')-(s1*s2')*(s1*s2')); %lamta1
res2=-((s1*s2')*((p1-q1)*s1')-(s1*s1')*((p1-
q1)*s2'))/((s1*s1')*(s2*s2')-(s1*s2')*(s1*s2')); %lamta2
if(res1<=1&&res1>=0&&res2<=1&&res2>=0)
   tmp1=p1+res1*s1;
```

```
    tmp2=q1+res2*s2;
    tmp=tmp1-tmp2;
    d=sqrt(tmp*tmp');
else
    res3=(q1-p1)*s1'/(s1*s1');
    if (res3>=0&&res3<=1)
        tmp=q1-(p1+res3*s1);
        d1=sqrt(tmp*tmp');
    else
        d1=sqrt(min((q1-p1)*(q1-p1)',(q1-p2)*(q1-p2)'));
    end
    res4=(q2-p1)*s1'/(s1*s1');
    if (res4>=0&&res4<=1)
        tmp=q2-(p1+res4*s1);
        d2=sqrt(tmp*tmp');
    else
        d2=sqrt(min((q2-p1)*(q2-p1)',(q2-p2)*(q2-p2)'));
    end

    res5=(p1-q1)*s2'/(s2*s2');
   if (res5>=0&&res5<=1)
        tmp=p1-(q1+res5*s2);
        d3=sqrt(tmp*tmp');
   else
        d3=sqrt(min((p1-q1)*(p1-q1)',(p1-q2)*(p1-q2)'));
   end

   res6=(p2-q1)*s2'/(s2*s2');
```

```
  if (res6>=0&&res6<=1)
     tmp=p2-(q1+res6*s2);
     d4=sqrt(tmp*tmp');
  else
     d4=sqrt(min((p2-q1)*(p2-q1)',(p2-q2)*(p2-q2)'));
  end

  d=min(min(d1,d2),min(d3,d4));
end
end
```

Appendix B

In.NEMD

```
units metal
dimension 3
boundary p p p
atom_style full


variable T1 equal 300
variable DT1 equal 0.0001
variable DT equal 0.001
variable POWER equal 3
read_data multy.data

pair_style airebo 3.0
pair_coeff * * /opt/data/sgxml1/LAMMPS/multy-NEMD-freeze-AIREBO-
3/CH.airebo C
comm_modify cutoff 14.70
neigh_modify one 10000
region F1 block 0 5 INF INF INF INF
region F2 block 95 100 INF INF INF INF
region C block 5 95 INF INF INF INF
group F11 region F1
group F22 region F2
group CC region C
```

```
velocity CC create ${T1 12345
fix NVT all nvt temp ${T1 ${T1 1
velocity F11 zero linear
velocity F22 zero linear

fix F111 F11 setforce 0.0 0.0 0.0
fix F222 F22 setforce 0.0 0.0 0.0

timestep ${DT1}
thermo_style custom step temp press
thermo 1000
run 250000

unfix NVT
fix NVE all nve

region SOURCE block 5 15 INF INF INF INF
region SINK block 85 95 INF INF INF INF

fix HEAT_IN CC ehex 1 ${POWER region SOURCE
fix HEAT_OUT CC ehex 1 -${POWER} region SINK

compute KE all ke/atom
variable KB equal 8.625e-5
variable TEMP atom c_KE/1.5/${KB

timestep ${DT1}
compute BLOCKS all chunk/atom bin/1d x lower 0.02 units reduced
```

```
dump 1 all xyz 5000 diamond.xyz
fix T_PROFILE all ave/chunk 10 1000 10000 BLOCKS v_TEMP file
temp.txt
run 5000000
```

Appendix C Publications

- M. Li, Z. Ali, X. Wei, L. Li, G. Song, X. Hou, H. Do, J. C. Greer, Z. Pan, C.-T. Lin, N. Jiang and J. Yu, *Compos. B. Eng.*, 2021, **208**, 108599.

- M. Li, L. Li, X. Hou, Y. Qin, G. Song, X. Wei, X. Kong, Z. Zhang, H. Do, J. C. Greer, F. Han, T. Cai, W. Dai, C.-T. Lin, N. Jiang and J. Yu, *Compos. Sci. Technol.*, 2021, **212**, 108883.

- M. Li, L. Li, Y. Qin, X. Wei, X. Kong, Z. Zhang, S. Xiong, H. Do, J. C. Greer, Z. Pan, T. Cai, W. Dai, C.-T. Lin, N. Jiang and J. Yu, *J. Mater. Chem.A*, 2022, **10**, 593-601.

- M. Li, L. Li, Y. Chen, Y. Qin, X. Wei, X. Kong , Z. Zhang, S. Xiong, H. Do, J. C. Greer, Z. Pan, X Shui, T. Cai, W. Dai, K. Nishimuraf, C. Lin, N. Jiang, J. Yu, *Compos Sci Technol,* 2022, **228**, 109677

- L. Li, Y. Qin, H. Wang, M. Li, G. Song, Y. Wu, X. Wei, Z. Ali, J. Yi, S. Song, C.-T. Lin, N. Jiang and J. Yu, *Compos. Commun.*, 2021, **23**, 100596.

Bibliography

1. Freeman, J.; Osterkamp, P.; Green, M.; Gibson, A.; Schiltgen, B., Challenges and opportunities for electric aircraft thermal management. *Aircraft Engineering and Aerospace Technology: An International Journal* **2014,** *86* (6), 519-524.

2. Roberts, R. A.; Decker, D. D., Control Architecture Study Focused on Energy Savings of an Aircraft Thermal Management System. *Journal of Dynamic Systems, Measurement, and Control* **2014,** *136* (4).

3. Doshi, R. J.; Ghodgaonkar, D., Adaptive Thermal Management Technique to Improve the Efficiency of SSPA for Geo-Synchronous Satellite. *J. Heat Transfer* **2018,** *140* (5).

4. Cao, Y.; Cao, D.; He, G.; Liu, L., Thermal alternation induced vibration analysis of spacecraft with lateral solar arrays in orbit. *Applied Mathematical Modelling* **2020,** *86*, 166-184.

5. Lee, H. S., Advanced Conductive Composite Materials for Spacecraft Application. *Advanced Materials Research* **2010,** *123-125*, 7-10.

6. Park, D.; Miyata, K.; Nagano, H., Thermal design and validation of radiation detector for the ChubuSat-2 micro-satellite with high-thermal-conductive graphite sheets. *Acta Astronautica* **2017,** *136*, 387-394.

7. Pang, L.; Li, S.; Liu, M.; A, R.; Li, A.; Meng, F., Influence of the Design Parameters of a Fuel Thermal Management System on Its Thermal Endurance. *Energies* **2018,** *11* (7).

8. Park, S.; Malikopoulos, A. A.; Kokkolaras, M.; Jung, D., Thermal management system modelling and component sizing for heavy duty series hybrid electric vehicles. *International Journal of Heavy Vehicle Systems* **2011,** *18* (3), 272-287.

9. Zhou, F.; Zhong, Y.; Zhang, P., Research on Thermal Management System for the Vehicle Application of Lithium-Ion Power Batteries. *Advanced Materials Research* **2012,** *347-353*, 984-988.

10. Kurmaev, R. K.; Struchkov, V. S.; Novak, V. V., Experience in the development of an effective thermal management system for the high-voltage battery of the vehicle. *IOP Conference Series: Materials Science and Engineering* **2020,** *819* (1), 012020.

11. Chung, Y.; Kim, M. S., Thermal analysis and pack level design of battery thermal management system with liquid cooling for electric vehicles. *Energy Convers. Manage.* **2019,** *196*, 105-116.

12. Xia, B.; Liu, Y.; Huang, R.; Yang, Y.; Lai, Y.; Zheng, W.; Wang, H.; Wang, W.; Wang, M., Thermal Analysis and Improvements of the Power Battery Pack with Liquid Cooling for Electric Vehicles. *Energies* **2019,** *12* (16).

13. McKeon, B. B.; Furukawa, J.; Fenstermacher, S., Advanced Lead–Acid Batteries and the Development of Grid-Scale Energy Storage Systems. *Proc. IEEE* **2014,** *102* (6), 951-963.

14. Keyser, M.; Pesaran, A.; Li, Q.; Santhanagopalan, S.; Smith, K.; Wood, E.; Ahmed, S.; Bloom, I.; Dufek, E.; Shirk, M.; Meintz, A.; Kreuzer, C.; Michelbacher, C.; Burnham, A.; Stephens, T.; Francfort, J.; Carlson, B.; Zhang, J.; Vijayagopal, R.; Hardy, K.; Dias, F.; Mohanpurkar, M.; Scoffield, D.; Jansen, A. N.; Tanim, T.; Markel, A., Enabling fast charging – Battery thermal considerations. *J. Power Sources* **2017,** *367*, 228-236.

15. Liu, J.; Li, H.; Li, W.; Shi, J.; Wang, H.; Chen, J., Thermal characteristics of power battery pack with liquid-based thermal management. *Appl. Therm. Eng.* **2020,** *164*, 114421.

16. Hansson, J.; Nilsson, T. M. J.; Ye, L.; Liu, J., Novel nanostructured thermal interface materials: a review. *Int. Mater. Rev.* **2018,** *63* (1), 22-45.

17. Hou, X.; Chen, Y.; Lv, L.; Dai, W.; Zhao, S.; Wang, Z.; Fu, L.; Lin, C.-T.; Jiang, N.; Yu, J., High-Thermal-Transport-Channel Construction within Flexible Composites via the Welding of Boron Nitride Nanosheets. *ACS Applied Nano Materials* **2019,** *2* (1), 360-368.

18. Zhang, Z. M.; Zhang, Z. M.; Luby, *Nano/microscale heat transfer*. Springer: 2007; Vol. 410.

19. Chen, G., *Nanoscale energy transport and conversion: a parallel treatment of electrons, molecules, phonons, and photons*. Oxford university press: 2005.

20. Ho, C. Y.; Powell, R. W.; Liley, P. E., Thermal Conductivity of the Elements. *J. Phys. Chem. Ref. Data* **1972,** *1* (2), 279-421.

21. Henry, A.; Chen, G.; Plimpton, S. J.; Thompson, A., 1D-to-3D transition of phonon heat conduction in polyethylene using molecular dynamics simulations. *Physical Review B* **2010,** *82* (14), 144308.

22. Hu, G.-J.; Cao, B.-Y.; Li, Y.-W., Thermal Conduction in a Single Polyethylene Chain Using Molecular Dynamics Simulations. *Chinese Physics Letters* **2014,** *31* (8), 086501.

23. Rossinsky, E.; Müller-Plathe, F., Anisotropy of the thermal conductivity in a crystalline polymer: Reverse nonequilibrium molecular dynamics simulation of the δ phase of syndiotactic polystyrene. *The Journal of Chemical Physics* **2009,** *130* (13), 134905.

24. Liu, J.; Yang, R., Tuning the thermal conductivity of polymers with mechanical strains. *Physical Review B* **2010,** *81* (17), 174122.

25. Kiessling, A.; Simavilla, D. N.; Vogiatzis, G. G.; Venerus, D. C., Thermal conductivity of amorphous polymers and its dependence on molecular weight. *Polymer* **2021,** *228*, 123881.

26. Matsubara, H.; Kikugawa, G.; Bessho, T.; Ohara, T., Evaluation of thermal conductivity and its structural dependence of a single nanodiamond using molecular dynamics simulation. *Diamond Relat. Mater.* **2020,** *102*, 107669.

27. Iwata, T.; Shintani, K., Reduction of the thermal conductivity of a graphene/hBN heterobilayer via interlayer sp3 bonds. *PCCP* **2018,** *20* (7), 5217-5226.

28. Varshney, V.; Patnaik, S. S.; Roy, A. K.; Froudakis, G.; Farmer, B. L., Modeling of Thermal Transport in Pillared-Graphene Architectures. *ACS Nano* **2010,** *4* (2), 1153-1161.

29. Sakhavand, N.; Shahsavari, R., Dimensional Crossover of Thermal Transport in Hybrid Boron Nitride Nanostructures. *ACS Applied Materials & Interfaces* **2015,** *7* (33),

18312-18319.

30. Callen, H. B.; Welton, T. A., Irreversibility and Generalized Noise. *Phys. Rev.* **1951,** *83* (1), 34-40.

31. Kubo, R., Statistical-Mechanical Theory of Irreversible Processes. I. General Theory and Simple Applications to Magnetic and Conduction Problems. *J. Phys. Soc. Jpn.* **1957,** *12* (6), 570-586.

32. Takahasi, H., Generalized Theory of Thermal Fluctuations. *J. Phys. Soc. Jpn.* **1952,** *7* (5), 439-446.

33. Nyquist, H., Thermal Agitation of Electric Charge in Conductors. *Phys. Rev.* **1928,** *32* (1), 110-113.

34. Reggiani, L.; Alfinito, E., Fluctuation Dissipation Theorem and Electrical Noise Revisited. *Fluctuation and Noise Letters* **2018,** *18* (01), 1930001.

35. Förster, H.; Büttiker, M., Fluctuation Relations Without Microreversibility in Nonlinear Transport. *Phys. Rev. Lett.* **2008,** *101* (13), 136805.

36. Akiba, M., 1/f dielectric polarization noise in silicon p-n junctions. *Appl. Phys. Lett.* **1997,** *71* (22), 3236-3238.

37. Hoel, A.; Vandamme, L. K. J.; Kish, L. B.; Olsson, E., Current and voltage noise in WO3 nanoparticle films. *J. Appl. Phys.* **2002,** *91* (8), 5221-5226.

38. Robert, D.; Nguyen, T.-H.; Gallet, F.; Wilhelm, C., In vivo determination of fluctuating forces during endosome trafficking using a combination of active and passive microrheology. *PloS one* **2010,** *5* (4), e10046.

39. McAndrew, C. P.; Tyson, C.; Zischkau, J.; Mehl, P.; Tuma, P. L.; Pegg, I. L.; Sarkar, A., Simple horizontal magnetic tweezers for micromanipulation of single DNA molecules and DNA—protein complexes. *BioTechniques* **2016,** *60* (1), 21-27.

40. Wilhelm, C., Out-of-Equilibrium Microrheology inside Living Cells. *Phys. Rev. Lett.* **2008,** *101* (2), 028101.

41. Markov, Y. A.; Markova, M. A., On the fluctuation–dissipation theorem for soft fermionic excitations in a hot QCD plasma. *Nucl. Phys. A* **2010,** *840* (1), 76-96.

42. Golden, K. I., Quadratic fluctuation-dissipation theorem for multilayer plasmas. *Physical Review E* **1999,** *59* (1), 228-233.

43. Lu, D.-X.; Golden, K. I., About the nonlinear fluctuation-dissipation theorem for plasmas in two and three dimensions. *Phys. Lett. A* **1983,** *97* (9), 391-394.

44. Kertész, J.; Kullmann, L.; Zawadowski, A. G.; Karádi, R.; Kaski, K., Correlations and response: absence of detailed balance on the stock market. *Physica A: Statistical Mechanics and its Applications* **2003,** *324* (1), 74-80.

45. Rosenow, B., FLUCTUATIONS AND MARKET FRICTION IN FINANCIAL TRADING. *International Journal of Modern Physics C* **2002,** *13* (03), 419-425.

46. 欧阳容百, 涨落耗散定理概述. *物理学进展* **1986,** *000* (003), 276.

47. 虞锦洪. 高导热聚合物基复合材料的制备与性能研究. 博士, 上海交通大学, 2012.

48. Zhou, L.; Yang, L., A method to calculate the effective thermal conductivity of spherical particle-laden composite. *IOP Conference Series: Materials Science and Engineering* **2019,** *493*, 012049.

49. Zhu, C.-Y.; Yang, W.-X.; Xu, H.-B.; Ding, B.; Gong, L.; Li, Z.-Y., A general effective thermal conductivity model for composites reinforced by non-contact spherical particles. *International Journal of Thermal Sciences* **2021,** *168*, 107088.

50. Sung, D. H.; Kim, M.; Park, Y.-B., Prediction of thermal conductivities of carbon-containing fiber-reinforced and multiscale hybrid composites. *Compos. B. Eng.* **2018,** *133*, 232-239.

51. Jena, D.; Das, A. K.; Mohapatra, R. C.; Das, S. K., Modelling and analysis of thermal conductivity of a hybrid polymer composite reinforced with particulate rice husk and particulate carbon fibre. *J. Therm. Anal. Calorim.* **2021**.

52. Fang, Y.; Li, L.-y.; Mawulé Dassekpo, J.-B.; Jang, S.-H., Heat transfer modelling of carbon nanotube reinforced composites. *Compos. B. Eng.* **2021,** *225*, 109280.

53. Zhou, L.; Sun, X.; Chen, M.; Zhu, Y.; Wu, H., Multiscale modeling and theoretical prediction for the thermal conductivity of porous plain-woven carbonized silica/phenolic composites. *Compos. Struct.* **2019,** *215*, 278-288.

54. Dan, D.; Zhang, H.; Tao, W.-Q., Effective structure of aerogels and decomposed contributions of its thermal conductivity. *Appl. Therm. Eng.* **2014,** *72* (1), 2-9.

55. Abbasov, H., The effective thermal conductivity of polymer composites filled with high conductive particles and the shell structure. *Polym. Compos.* **2022,** *n/a* (n/a).

56. Chauhan, D.; Singhvi, N.; Singh, R., Dependence of effective thermal conductivity of composite materials on the size of filler particles. *J. Reinf. Plast. Compos.* **2013,** *32* (18), 1323-1330.

57. Alam, F. E.; Dai, W.; Yang, M.; Du, S.; Li, X.; Yu, J.; Jiang, N.; Lin, C.-T., In situ formation of a cellular graphene framework in thermoplastic composites leading to superior thermal conductivity. *J. Mater. Chem.A* **2017,** *5* (13), 6164-6169.

58. Yoo, Y.; Lee, H. L.; Ha, S. M.; Jeon, B. K.; Won, J. C.; Lee, S.-G., Effect of graphite and carbon fiber contents on the morphology and properties of thermally conductive composites based on polyamide 6. *Polym. Int.* **2014,** *63* (1), 151-157.

59. Deng, S.; Zhu, Y.; Qi, X.; Yu, W.; Chen, F.; Fu, Q., Preparation of polyvinylidene fluoride/expanded graphite composites with enhanced thermal conductivity via ball milling treatment. *RSC Advances* **2016,** *6* (51), 45578-45584.

60. Wang, Z.-G.; Gong, F.; Yu, W.-C.; Huang, Y.-F.; Zhu, L.; Lei, J.; Xu, J.-Z.; Li, Z.-M., Synergetic enhancement of thermal conductivity by constructing hybrid conductive network in the segregated polymer composites. *Compos. Sci. Technol.* **2018,** *162*, 7-13.

61. Wei, X.; Zhang, T.; Luo, T., Chain conformation-dependent thermal conductivity of amorphous polymer blends: the impact of inter- and intra-chain interactions. *PCCP* **2016,** *18* (47), 32146-32154.

62. Bai, L.; Zhao, X.; Bao, R.-Y.; Liu, Z.-Y.; Yang, M.-B.; Yang, W., Effect of temperature, crystallinity and molecular chain orientation on the thermal conductivity of polymers: a case study of PLLA. *Journal of Materials Science* **2018,** *53* (14), 10543-10553.

63. Yoshihara, S.; Ezaki, T.; Nakamura, M.; Watanabe, J.; Matsumoto, K., Enhanced Thermal Conductivity of Thermoplastics by Lamellar Crystal Alignment of Polymer Matrices. *Macromol. Chem. Phys.* **2012,** *213* (21), 2213-2219.

64. Chen, A.; Wu, Y.; Zhou, S.; Xu, W.; Jiang, W.; Lv, Y.; Guo, W.; Chi, K.; Sun, Q.; Fu, T.; Xie, T.; Zhu, Y.; Liang, X.-g., High thermal conductivity polymer chains with reactive groups: a step towards true application. *Materials Advances* **2020,** *1* (6), 1996-2002.

65. Pal, S.; Balasubramanian, G.; Puri, I. K., Modifying thermal transport in electrically conducting polymers: Effects of stretching and combining polymer chains. *The Journal of Chemical Physics* **2012,** *136* (4), 044901.

66. Koda, T.; Toyoshima, T.; Komatsu, T.; Takezawa, Y.; Nishioka, A.; Miyata, K., Ordering simulation of high thermal conductivity epoxy resins. *Polym. J.* **2013,** *45* (4), 444-448.

67. Shen, S.; Henry, A.; Tong, J.; Zheng, R.; Chen, G., Polyethylene nanofibres with very high thermal conductivities. *Nature Nanotechnology* **2010,** *5* (4), 251-255.

68. Dai, J.; Wang, Q.; Li, W.; Wei, Z.; Xu, G., Properties of well aligned SWNT modified poly (methyl methacrylate) nanocomposites. *Mater. Lett.* **2007,** *61* (1), 27-29.

69. Hansen, D.; Bernier, G. A., Thermal conductivity of polyethylene: The effects of crystal size, density and orientation on the thermal conductivity. *Polymer Engineering & Science* **1972,** *12* (3), 204-208.

70. Chen, H.; Ginzburg, V. V.; Yang, J.; Yang, Y.; Liu, W.; Huang, Y.; Du, L.; Chen, B., Thermal conductivity of polymer-based composites: Fundamentals and applications. *Prog. Polym. Sci.* **2016,** *59*, 41-85.

71. Mehra, N.; Mu, L.; Ji, T.; Yang, X.; Kong, J.; Gu, J.; Zhu, J., Thermal transport in polymeric materials and across composite interfaces. *Applied Materials Today* **2018,** *12*, 92-130.

72. Kikugawa, G.; Desai, T. G.; Keblinski, P.; Ohara, T., Effect of crosslink formation on heat conduction in amorphous polymers. *J. Appl. Phys.* **2013,** *114* (3), 034302.

73. Xiong, X.; Yang, M.; Liu, C.; Li, X.; Tang, D., Thermal conductivity of cross-linked polyethylene from molecular dynamics simulation. *J. Appl. Phys.* **2017,** *122* (3), 035104.

74. Kim, G.-H.; Lee, D.; Shanker, A.; Shao, L.; Kwon, M. S.; Gidley, D.; Kim, J.; Pipe, K. P., High thermal conductivity in amorphous polymer blends by engineered interchain

interactions. *Nature Materials* **2015,** *14* (3), 295-300.

75. Rashidi, V.; Coyle, E. J.; Sebeck, K.; Kieffer, J.; Pipe, K. P., Thermal Conductance in Cross-linked Polymers: Effects of Non-Bonding Interactions. *The Journal of Physical Chemistry B* **2017,** *121* (17), 4600-4609.

76. Zhang, Y.; Zhang, X.; Yang, L.; Zhang, Q.; Fitzgerald, M. L.; Ueda, A.; Chen, Y.; Mu, R.; Li, D.; Bellan, L. M., Thermal transport in electrospun vinyl polymer nanofibers: effects of molecular weight and side groups. *Soft Matter* **2018,** *14* (47), 9534-9541.

77. Guo, Z.; Lee, D.; Liu, Y.; Sun, F.; Sliwinski, A.; Gao, H.; Burns, P. C.; Huang, L.; Luo, T., Tuning the thermal conductivity of solar cell polymers through side chain engineering. *PCCP* **2014,** *16* (17), 7764-7771.

78. Wang, M.; Wang, J.; Yang, H.; Lin, B.-P.; Chen, E.-Q.; Keller, P.; Zhang, X.-Q.; Sun, Y., Homeotropically-aligned main-chain and side-on liquid crystalline elastomer films with high anisotropic thermal conductivities. *Chem. Commun.* **2016,** *52* (23), 4313-4316.

79. Kanari, K.; Ozawa, T., Thermal Conductivity of Epoxy Resins Cured with Aliphatic Amines. *Polym. J.* **1973,** *4* (4), 372-378.

80. Tonpheng, B.; Yu, J.; Andersson, O., Effects of cross-links, pressure and temperature on the thermal properties and glass transition behaviour of polybutadiene. *PCCP* **2011,** *13* (33), 15047-15054.

81. Lv, G.; Jensen, E.; Shan, N.; Evans, C. M.; Cahill, D. G., Effect of Aromatic/Aliphatic Structure and Cross-Linking Density on the Thermal Conductivity of Epoxy Resins. *ACS Applied Polymer Materials* **2021,** *3* (3), 1555-1562.

82. Guo, Y.; Zhou, Y.; Xu, Y., Engineering polymers with metal-like thermal conductivity—Present status and future perspectives. *Polymer* **2021,** *233*, 124168.

83. Barclay, G. G.; Ober, C. K.; Papathomas, K. I.; Wang, D. W., Liquid crystalline epoxy thermosets based on dihydroxymethylstilbene: Synthesis and characterization. *J. Polym. Sci., Part A: Polym. Chem.* **1992,** *30* (9), 1831-1843.

84. Hammerschmidt, A.; Geibel, K.; Strohmer, F., In situ photopolymerized, oriented liquid-crystalline diacrylates with high thermal conductivities. *Adv. Mater.* **1993,** *5* (2),

107-109.

85. Akatsuka, M.; Takezawa, Y., Study of high thermal conductive epoxy resins containing controlled high-order structures. *J. Appl. Polym. Sci.* **2003,** *89* (9), 2464-2467.

86. Kato, T.; Nakamura, T.; Agari, Y.; Ochi, M., Thermal conductivity of homogeneous alignment networks formed with mono- and bi-functional polymerizable liquid crystals. *J. Appl. Polym. Sci.* **2007,** *104* (5), 3453-3458.

87. Fukushima, K.; Takahashi, H.; Takezawa, Y.; Kawahira, T.; Itoh, M.; Kanai, J., High Thermal Conductive Resin Composites with Controlled Nanostructures for Electric Devices. *IEEJ Transactions on Fundamentals and Materials* **2006,** *126* (11), 1167-1172.

88. Kim, D.-G.; Kim, Y. H.; Shin, T. J.; Cha, E. J.; Kim, D. S.; Kim, B. G.; Yoo, Y.; Kim, Y. S.; Yi, M. H.; Won, J. C., Highly anisotropic thermal conductivity of discotic nematic liquid crystalline films with homeotropic alignment. *Chem. Commun.* **2017,** *53* (58), 8227-8230.

89. Yang, Y., Thermal Conductivity. In *Physical Properties of Polymers Handbook*, Mark, J. E., Ed. Springer New York: New York, NY, 2007; pp 155-163.

90. Harada, M.; Hamaura, N.; Ochi, M.; Agari, Y., Thermal conductivity of liquid crystalline epoxy/BN filler composites having ordered network structure. *Compos. B. Eng.* **2013,** *55*, 306-313.

91. Islam, A. M.; Lim, H.; You, N.-H.; Ahn, S.; Goh, M.; Hahn, J. R.; Yeo, H.; Jang, S. G., Enhanced Thermal Conductivity of Liquid Crystalline Epoxy Resin using Controlled Linear Polymerization. *ACS Macro Letters* **2018,** *7* (10), 1180-1185.

92. Yang, X.; Zhu, J.; Yang, D.; Zhang, J.; Guo, Y.; Zhong, X.; Kong, J.; Gu, J., High-efficiency improvement of thermal conductivities for epoxy composites from synthesized liquid crystal epoxy followed by doping BN fillers. *Compos. B. Eng.* **2020,** *185*, 107784.

93. Park, M.; Kang, D.-G.; Ko, H.; Rim, M.; Tran, D. T.; Park, S.; Kang, M.; Kim, T.-W.; Kim, N.; Jeong, K.-U., Molecular engineering of a porphyrin-based hierarchical superstructure: planarity control of a discotic metallomesogen for high thermal conductivity. *Materials Horizons* **2020,** *7* (10), 2635-2642.

94. Tanaka, S.; Takezawa, Y.; Kanie, K.; Muramatsu, A., Homeotropically Aligned Monodomain-like Smectic-A Structure in Liquid Crystalline Epoxy Films: Analysis of the Local Ordering Structure by Microbeam Small-Angle X-ray Scattering. *ACS Omega* **2020,** *5* (33), 20792-20799.

95. Tang, N.; Tanaka, S.; Takezawa, Y.; Kanie, K., Highly anisotropic thermal conductivity of mesogenic epoxy resin film through orientation control. *J. Appl. Polym. Sci.* **2021,** *138* (47), 51396.

96. Shin, J.; Kang, M.; Tsai, T.; Leal, C.; Braun, P. V.; Cahill, D. G., Thermally Functional Liquid Crystal Networks by Magnetic Field Driven Molecular Orientation. *ACS Macro Letters* **2016,** *5* (8), 955-960.

97. Harada, M.; Ochi, M.; Tobita, M.; Kimura, T.; Ishigaki, T.; Shimoyama, N.; Aoki, H., Thermal-conductivity properties of liquid-crystalline epoxy resin cured under a magnetic field. *J. Polym. Sci., Part B: Polym. Phys.* **2003,** *41* (14), 1739-1743.

98. Kang, D.-G.; Ko, H.; Koo, J.; Lim, S.-I.; Kim, J. S.; Yu, Y.-T.; Lee, C.-R.; Kim, N.; Jeong, K.-U., Anisotropic Thermal Interface Materials: Directional Heat Transfer in Uniaxially Oriented Liquid Crystal Networks. *ACS Applied Materials & Interfaces* **2018,** *10* (41), 35557-35562.

99. Ruan, K.; Zhong, X.; Shi, X.; Dang, J.; Gu, J., Liquid crystal epoxy resins with high intrinsic thermal conductivities and their composites: A mini-review. *Materials Today Physics* **2021,** *20*, 100456.

100. Yamazaki, S.; Tokita, M., A Correlation between Thermal Diffusivity and Long Period in Thermotropic Liquid Crystalline Polyesters. *Macromolecules* **2019,** *52* (24), 9781-9785.

101. Ge, S.-J.; Zhao, T.-P.; Wang, M.; Deng, L.-L.; Lin, B.-P.; Zhang, X.-Q.; Sun, Y.; Yang, H.; Chen, E.-Q., A homeotropic main-chain tolane-type liquid crystal elastomer film exhibiting high anisotropic thermal conductivity. *Soft Matter* **2017,** *13* (32), 5463-5468.

102. Li, Y.; Li, C.; Zhang, L.; Zhou, W., Effect of microscopic-ordered structures on intrinsic thermal conductivity of liquid-crystalline polysiloxane. *Journal of Materials*

Science: Materials in Electronics **2019,** *30* (9), 8329-8338.

103. Kang, D.-G.; Park, M.; Ko, H.; Rim, M.; Park, S.; Tran, D. T.; Yoo, M.-J.; Kim, N.; Jeong, K.-U., Thermal Energy Harvest and Reutilization by the Combination of Thermal Conducting Reactive Mesogens and Heat-Storage Mesogens. *ACS Applied Materials & Interfaces* **2021,** *13* (11), 13637-13647.

104. Liu, Y.; Chen, J.; Zhang, Y.; Gao, S.; Lu, Z.; Xue, Q., Highly thermal conductive benzoxazine-epoxy interpenetrating polymer networks containing liquid crystalline structures. *J. Polym. Sci., Part B: Polym. Phys.* **2017,** *55* (24), 1813-1821.

105. Xiao, M.; Du, B. X., Review of high thermal conductivity polymer dielectrics for electrical insulation. *High Voltage* **2016,** *1* (1), 34-42.

106. Xu, X.; Chen, J.; Zhou, J.; Li, B., Thermal Conductivity of Polymers and Their Nanocomposites. *Adv. Mater.* **2018,** *30* (17), 1705544.

107. Zhang, R.-C.; Huang, Z.; Sun, D.; Ji, D.; Zhong, M.; Zang, D.; Xu, J.-Z.; Wan, Y.; Lu, A., New insights into thermal conductivity of uniaxially stretched high density polyethylene films. *Polymer* **2018,** *154*, 42-47.

108. Henry, A.; Chen, G., High Thermal Conductivity of Single Polyethylene Chains Using Molecular Dynamics Simulations. *Phys. Rev. Lett.* **2008,** *101* (23), 235502.

109. Shulumba, N.; Hellman, O.; Minnich, A. J., Lattice Thermal Conductivity of Polyethylene Molecular Crystals from First-Principles Including Nuclear Quantum Effects. *Phys. Rev. Lett.* **2017,** *119* (18), 185901.

110. Wang, Z.; Carter Jeffrey, A.; Lagutchev, A.; Koh Yee, K.; Seong, N.-H.; Cahill David, G.; Dlott Dana, D., Ultrafast Flash Thermal Conductance of Molecular Chains. *Science* **2007,** *317* (5839), 787-790.

111. Wang, M.; Lin, S., Ballistic Thermal Transport in Carbyne and Cumulene with Micron-Scale Spectral Acoustic Phonon Mean Free Path. *Scientific Reports* **2015,** *5* (1), 18122.

112. Choy, C. L., Thermal conductivity of polymers. *Polymer* **1977,** *18* (10), 984-1004.

113. Choy, C. L.; Wong, Y. W.; Yang, G. W.; Kanamoto, T., Elastic modulus and thermal

conductivity of ultradrawn polyethylene. *J. Polym. Sci., Part B: Polym. Phys.* **1999,** *37* (23), 3359-3367.

114. Choy, C. L.; Chen, F. C.; Luk, W. H., Thermal conductivity of oriented crystalline polymers. *Journal of Polymer Science: Polymer Physics Edition* **1980,** *18* (6), 1187-1207.

115. Fujishiro, H.; Ikebe, M.; Kashima, T.; Yamanaka, A., Thermal Conductivity and Diffusivity of High-Strength Polymer Fibers. *Jpn. J. Appl. Phys.* **1997,** *36* (Part 1, No. 9A), 5633-5637.

116. Ma, J.; Zhang, Q.; Zhang, Y.; Zhou, L.; Yang, J.; Ni, Z., A rapid and simple method to draw polyethylene nanofibers with enhanced thermal conductivity. *Appl. Phys. Lett.* **2016,** *109* (3), 033101.

117. Wang, X.; Ho, V.; Segalman, R. A.; Cahill, D. G., Thermal Conductivity of High-Modulus Polymer Fibers. *Macromolecules* **2013,** *46* (12), 4937-4943.

118. Canetta, C.; Guo, S.; Narayanaswamy, A., Measuring thermal conductivity of polystyrene nanowires using the dual-cantilever technique. *Rev. Sci. Instrum.* **2014,** *85* (10), 104901.

119. Zhu, B.; Liu, J.; Wang, T.; Han, M.; Valloppilly, S.; Xu, S.; Wang, X., Novel Polyethylene Fibers of Very High Thermal Conductivity Enabled by Amorphous Restructuring. *ACS Omega* **2017,** *2* (7), 3931-3944.

120. 王子君, 周., 睢雪珍, 董丽娜, 张溟涛, 金属/聚合物导热复合材料研究进展. *化学推进剂与高分子材料* **2015,** *13* (02), 28-33.

121. 寇雨佳; 周文英; 龚莹; 蔡会武; 吴红菊, 聚合物/导热金属复合材料的研究进展. *中国塑料* **2018,** *32* (03), 6-11.

122. Ochirkhuyag, N.; Matsuda, R.; Song, Z.; Nakamura, F.; Endo, T.; Ota, H., Liquid metal-based nanocomposite materials: fabrication technology and applications. *Nanoscale* **2021,** *13* (4), 2113-2135.

123. Wang, H.; Xing, W.; Chen, S.; Song, C.; Dickey, M. D.; Deng, T., Liquid Metal Composites with Enhanced Thermal Conductivity and Stability Using Molecular Thermal Linker. *Adv. Mater.* **2021,** *33* (43), 2103104.

124. Yao, B.; Xu, X.; Li, H.; Han, Z.; Hao, J.; Yang, G.; Xie, Z.; Chen, Y.; Liu, W.; Wang, Q.; Wang, H., Soft liquid-metal/elastomer foam with compression-adjustable thermal conductivity and electromagnetic interference shielding. *Chem. Eng. J.* **2021,** *410*, 128288.

125. Zhou, L.-y.; Ye, J.-h.; Fu, J.-z.; Gao, Q.; He, Y., 4D Printing of High-Performance Thermal-Responsive Liquid Metal Elastomers Driven by Embedded Microliquid Chambers. *ACS Applied Materials & Interfaces* **2020,** *12* (10), 12068-12074.

126. Uppal, A.; Ralphs, M.; Kong, W.; Hart, M.; Rykaczewski, K.; Wang, R. Y., Pressure-Activated Thermal Transport via Oxide Shell Rupture in Liquid Metal Capsule Beds. *ACS Applied Materials & Interfaces* **2020,** *12* (2), 2625-2633.

127. Huang, K.; Qiu, W.; Ou, M.; Liu, X.; Liao, Z.; Chu, S., An anti-leakage liquid metal thermal interface material. *RSC Advances* **2020,** *10* (32), 18824-18829.

128. Sun, J.; Zhuang, J.; Jiang, H.; Huang, Y.; Zheng, X.; Liu, Y.; Wu, D., Thermal dissipation performance of metal-polymer composite heat exchanger with V-shape microgrooves: A numerical and experimental study. *Appl. Therm. Eng.* **2017,** *121*, 492-500.

129. Zhuang, J.; Huang, C.; Zhou, G.; Liu, Z.; Xu, H.; Wu, D.; Fan, Y.; Zhang, Y., Influence of factors on heat dissipation performance of composite metal–polymer heat exchanger with rectangular microstructure. *Appl. Therm. Eng.* **2016,** *102*, 1473-1480.

130. Zhuang, J.; Sun, J.; Wu, D.; Liu, Y.; Patil, R. R.; Pan, D.; Guo, Z., Multi-factor analysis on thermal conductive property of metal-polymer composite microstructure heat exchanger. *Advanced Composites and Hybrid Materials* **2021,** *4* (1), 27-35.

131. Lindsay, L.; Broido, D. A.; Reinecke, T. L., First-Principles Determination of Ultrahigh Thermal Conductivity of Boron Arsenide: A Competitor for Diamond? *Phys. Rev. Lett.* **2013,** *111* (2), 025901.

132. Yoo, M. J.; Seo, D. S.; Kim, S. H.; Lee, W. S.; Seong, T.-G.; Kweon, S.-H.; Jeong, B.-J.; Jeong, Y. H.; Nahm, S., Electric field assembled anisotropic alumina composite for thermal dissipation applications. *J. Compos. Mater.* **2012,** *48* (2), 201-208.

133. Cheng, J. P.; Liu, T.; Zhang, J.; Wang, B. B.; Ying, J.; Liu, F.; Zhang, X. B., Influence of phase and morphology on thermal conductivity of alumina particle/silicone rubber composites. *Appl. Phys. A* **2014,** *117* (4), 1985-1992.

134. Hojo, F.; Kagawa, H.; Takezawa, Y., Synthesis of a polymer composite with networked α-alumina fiber and evaluation of its thermal conductivity. *J. Ceram. Soc. Jpn.* **2011,** *119* (1391), 601-604.

135. Chen, Y.; Hou, X.; Liao, M.; Dai, W.; Wang, Z.; Yan, C.; Li, H.; Lin, C.-T.; Jiang, N.; Yu, J., Constructing a “pea-pod-like” alumina-graphene binary architecture for enhancing thermal conductivity of epoxy composite. *Chem. Eng. J.* **2020,** *381*, 122690.

136. Partridge, G., Inorganic materials V. Ceramic materials possessing high thermal conductivity. *Adv. Mater.* **1992,** *4* (1), 51-54.

137. Xu, Y.; Yang, C.; Li, J.; Mao, X.; Zhang, H.; Hu, S.; Wang, S., Development of AlN/Epoxy Composites with Enhanced Thermal Conductivity. *Materials* **2017,** *10* (12).

138. Zhou, Y.; Wang, H.; Wang, L.; Yu, K.; Lin, Z.; He, L.; Bai, Y., Fabrication and characterization of aluminum nitride polymer matrix composites with high thermal conductivity and low dielectric constant for electronic packaging. *Materials Science and Engineering: B* **2012,** *177* (11), 892-896.

139. Nagai, Y.; Lai, G.-C., Thermal Conductivity of Epoxy Resin Filled with Particulate Aluminum Nitride Powder. *J. Ceram. Soc. Jpn.* **1997,** *105* (1219), 197-200.

140. Tang, S.; Cao, Z., Structural and electronic properties of the fully hydrogenated boron nitride sheets and nanoribbons: Insight from first-principles calculations. *Chem. Phys. Lett.* **2010,** *488* (1), 67-72.

141. Zhou, W.; Qi, S.; An, Q.; Zhao, H.; Liu, N., Thermal conductivity of boron nitride reinforced polyethylene composites. *Mater. Res. Bull.* **2007,** *42* (10), 1863-1873.

142. Wang, M.; Jiao, Z.; Chen, Y.; Hou, X.; Fu, L.; Wu, Y.; Li, S.; Jiang, N.; Yu, J., Enhanced thermal conductivity of poly(vinylidene fluoride)/boron nitride nanosheet composites at low filler content. *Composites Part A: Applied Science and Manufacturing* **2018,** *109*, 321-329.

143. Perevislov, S. N., Structure, Properties, and Applications of Graphite-Like Hexagonal Boron Nitride. *Refract. Ind. Ceram* **2019,** *60* (3), 291-295.

144. Lee, H. L.; Kwon, O. H.; Ha, S. M.; Kim, B. G.; Kim, Y. S.; Won, J. C.; Kim, J.; Choi, J. H.; Yoo, Y., Thermal conductivity improvement of surface-enhanced polyetherimide (PEI) composites using polyimide-coated h-BN particles. *PCCP* **2014,** *16* (37), 20041-20046.

145. Kusunose, T.; Uno, Y.; Tanaka, Y.; Sekino, T., Isotropic enhancement of the thermal conductivity of polymer composites by dispersion of equiaxed polyhedral boron nitride fillers. *Compos. Sci. Technol.* **2021,** *208*, 108770.

146. Zhang, X.; Zhang, H.; Li, D.; Xu, H.; Huang, Y.; Liu, Y.; Wu, D.; Sun, J., Highly thermally conductive and electrically insulating polydimethylsiloxane composites prepared by ultrasonic-assisted forced infiltration for thermal management applications. *Compos. B. Eng.* **2021,** *224*, 109207.

147. Lim, G.; Bok, G.; Kim, Y.-S.; Kim, Y., Fabrication of h-BN Filled Epoxy-Based Thermally Conductive Adhesive Tapes Containing Cyclic Carbonate-Terminated Oligomers. *Electronic Materials Letters* **2021**.

148. Guo, L.; Zhang, Z.; Li, M.; Kang, R.; Chen, Y.; Song, G.; Han, S.-T.; Lin, C.-T.; Jiang, N.; Yu, J., Extremely high thermal conductivity of carbon fiber/epoxy with synergistic effect of MXenes by freeze-drying. *Compos. Commun.* **2020,** *19*, 134-141.

149. Wang, M.; Zhang, T.; Mao, D.; Yao, Y.; Zeng, X.; Ren, L.; Cai, Q.; Mateti, S.; Li, L. H.; Zeng, X.; Du, G.; Sun, R.; Chen, Y.; Xu, J.-B.; Wong, C.-P., Highly Compressive Boron Nitride Nanotube Aerogels Reinforced with Reduced Graphene Oxide. *ACS Nano* **2019,** *13* (7), 7402-7409.

150. Xia, J.; Qin, Y.; Wei, X.; Li, L.; Li, M.; Kong, X.; Xiong, S.; Cai, T.; Dai, W.; Lin, C.-T.; Jiang, N.; Fang, S.; Yi, J.; Yu, J., Enhanced Thermal Conductivity of Polymer Composite by Adding Fishbone-like Silicon Carbide. *Nanomaterials* **2021,** *11* (11).

151. Shen, D.; Zhan, Z.; Liu, Z.; Cao, Y.; Zhou, L.; Liu, Y.; Dai, W.; Nishimura, K.; Li, C.; Lin, C.-T.; Jiang, N.; Yu, J., Enhanced thermal conductivity of epoxy composites filled

with silicon carbide nanowires. *Scientific Reports* **2017,** *7* (1), 2606.

152. Yao, Y.; Zhu, X.; Zeng, X.; Sun, R.; Xu, J.-B.; Wong, C.-P., Vertically Aligned and Interconnected SiC Nanowire Networks Leading to Significantly Enhanced Thermal Conductivity of Polymer Composites. *ACS Applied Materials & Interfaces* **2018,** *10* (11), 9669-9678.

153. Chen, J.-P.; Wang, Z.-F.; Yi, Z.-L.; Xie, L.-J.; Liu, Z.; Zhang, S.-C.; Chen, C.-M., SiC whiskers nucleated on rGO and its potential role in thermal conductivity and electronic insulation. *Chem. Eng. J.* **2021,** *423*, 130181.

154. Bai, G.; Jiang, W.; Chen, L., Effect of Interfacial Thermal Resistance on Effective Thermal Conductivity of MoSi₂/SiC Composites. *MATERIALS TRANSACTIONS* **2006,** *47* (4), 1247-1249.

155. Qin, Y.; Wang, B.; Hou, X.; Li, L.; Guan, C.; Pan, Z.; Li, M.; Du, Y.; Lu, Y.; Wei, X.; Xiong, S.; Song, G.; Xue, C.; Dai, W.; Lin, C.-T.; Yi, J.; Jiang, N.; Yu, J., Constructing Tanghulu-like Diamond@Silicon carbide nanowires for enhanced thermal conductivity of polymer composite. *Compos. Commun.* **2022,** *29*, 101008.

156. Amirthan, G.; Udaya kumar, A.; Balasubramanian, M., Thermal conductivity studies on Si/SiC ceramic composites. *Ceram. Int.* **2011,** *37* (1), 423-426.

157. Dai, W.; Ma, T.; Yan, Q.; Gao, J.; Tan, X.; Lv, L.; Hou, H.; Wei, Q.; Yu, J.; Wu, J.; Yao, Y.; Du, S.; Sun, R.; Jiang, N.; Wang, Y.; Kong, J.; Wong, C.; Maruyama, S.; Lin, C.-T., Metal-Level Thermally Conductive yet Soft Graphene Thermal Interface Materials. *ACS Nano* **2019,** *13* (10), 11561-11571.

158. Wang, Y.; Zhang, Y.; Zhang, Z.; Li, T.; Jiang, J.; Zhang, X.; Liu, T.; Qiao, J.; Huang, J.; Dong, W., Pistachio-Inspired Bulk Graphene Oxide-Based Materials with Shapeability and Recyclability. *ACS Nano* **2022,** *16* (2), 3394-3403.

159. Chen, Y.; Hou, X.; Kang, R.; Liang, Y.; Guo, L.; Dai, W.; Nishimura, K.; Lin, C.-T.; Jiang, N.; Yu, J., Highly flexible biodegradable cellulose nanofiber/graphene heat-spreader films with improved mechanical properties and enhanced thermal conductivity. *J. Mater. Chem. C* **2018,** *6* (46), 12739-12745.

160. Liu, Z.; Chen, Y.; Li, Y.; Dai, W.; Yan, Q.; Alam, F. E.; Du, S.; Wang, Z.; Nishimura, K.; Jiang, N.; Lin, C.-T.; Yu, J., Graphene foam-embedded epoxy composites with significant thermal conductivity enhancement. *Nanoscale* **2019,** *11* (38), 17600-17606.

161. Ali, Z.; Kong, X.; Li, M.; Hou, X.; Li, L.; Qin, Y.; Song, G.; Wei, X.; Zhao, S.; Cai, T.; Dai, W.; Lin, C.-T.; Jiang, N.; Yu, J., Ultrahigh Thermal Conductivity of Epoxy Composites with Hybrid Carbon Fiber and Graphene Filler. *Fibers and Polymers* **2021**.

162. Vorobyeva, E. A.; Evseev, A. P.; Petrov, V. L.; Shemukhin, A. A.; Chechenin, N. G., The conductivity in Composite Materials Based on Oriented Carbon Nanotubes. *Moscow University Physics Bulletin* **2021,** *76* (1), 29-35.

163. Dong, Z.-j.; Sun, B.; Zhu, H.; Yuan, G.-m.; Li, B.-l.; Guo, J.-g.; Li, X.-k.; Cong, Y.; Zhang, J., A review of aligned carbon nanotube arrays and carbon/carbon composites: fabrication, thermal conduction properties and applications in thermal management. *New Carbon Materials* **2021,** *36* (5), 873-892.

164. Wang, K.; Zhang, W.; Phelan, R.; Morris, M. A.; Holmes, J. D., Direct Fabrication of Well-Aligned Free-Standing Mesoporous Carbon Nanofiber Arrays on Silicon Substrates. *J. Am. Chem. Soc.* **2007,** *129* (44), 13388-13389.

165. Lu, A.-H.; Hao, G.-P.; Sun, Q.; Zhang, X.-Q.; Li, W.-C., Chemical Synthesis of Carbon Materials With Intriguing Nanostructure and Morphology. *Macromol. Chem. Phys.* **2012,** *213* (10-11), 1107-1131.

166. Cao, Q.; He, F.; Li, Y.; He, Z.; Fan, J.; Wang, R.; Hu, W.; Zhang, K.; Yang, W., Graphene-carbon nanotube hybrid aerogel/polyethylene glycol phase change composite for thermal management. *Fullerenes, Nanotubes and Carbon Nanostructures* **2020,** *28* (8), 656-662.

167. Ata, S.; Subramaniam, C.; Nishizawa, A.; Yamada, T.; Hata, K., Highly Thermally Conductive Yet Flexible Composite of Carbon Fiber, Carbon Nanotube, and Rubber Obtained by Decreasing the Thermal Resistivity at the Interface between Carbon Fiber and Carbon Nanotube *Adv. Eng. Mater.* **2017,** *19* (2), 1600596.

168. Kim, Y. A.; Kamio, S.; Tajiri, T.; Hayashi, T.; Song, S. M.; Endo, M.; Terrones, M.;

Dresselhaus, M. S., Enhanced thermal conductivity of carbon fiber/phenolic resin composites by the introduction of carbon nanotubes. *Appl. Phys. Lett.* **2007,** *90* (9), 093125.

169. Li, L.; Qin, Y.; Wang, H.; Li, M.; Song, G.; Wu, Y.; Wei, X.; Ali, Z.; Yi, J.; Song, S.; Lin, C.-T.; Jiang, N.; Yu, J., Improving thermal conductivity of poly(vinyl alcohol) composites by using functionalized nanodiamond. *Compos. Commun.* **2021,** *23*, 100596.

170. Wang, X.; He, X.; Xu, Z.; Qu, X., Preparation of W-Plated Diamond and Improvement of Thermal Conductivity of Diamond-WC-Cu Composite. *Metals* **2021,** *11* (3).

171. Yang, L.; Sun, L.; Bai, W.; Li, L., Thermal conductivity of Cu-Ti/diamond composites via spark plasma sintering. *Diamond Relat. Mater.* **2019,** *94*, 37-42.

172. Zeng, C.; Shen, J.; Gong, M.; Chen, H., Enhanced thermal conductivity in TiC/diamond or Cr3C2/diamond particles modified Bi-In-Sn compounds. *Journal of Materials Science: Materials in Electronics* **2021,** *32* (10), 13205-13219.

173. Wu, X.; Li, L.; Zhang, W.; Song, M.; Yang, W.; Peng, K., Effect of surface roughening on the interfacial thermal conductance of diamond/copper composites. *Diamond Relat. Mater.* **2019,** *98*, 107467.

174. Giri, A.; Evans, A. M.; Rahman, M. A.; McGaughey, A. J. H.; Hopkins, P. E., Highly Negative Poisson's Ratio in Thermally Conductive Covalent Organic Frameworks. *ACS Nano* **2022,** *16* (2), 2843-2851.

175. Zhang, Y.; Lei, C.; Wu, K.; Fu, Q., Fully Organic Bulk Polymer with Metallic Thermal Conductivity and Tunable Thermal Pathways. *Advanced Science* **2021,** *8* (14), 2004821.

176. Kundalwal, S. I.; Suresh Kumar, R.; Ray, M. C., Effective thermal conductivities of a novel fuzzy carbon fiber heat exchanger containing wavy carbon nanotubes. *Int. J. Heat Mass Transfer* **2014,** *72*, 440-451.

177. Zhang, H.; Zhang, X.; Li, D.; Yang, X.; Wu, D.; Sun, J., Thermal conductivity enhancement via conductive network conversion from "sand-like" to "stone-like" in the

polydimethylsiloxane composites. *Compos. Commun.* **2020,** *22*, 100509.

178. Li, X.; Ye, X.; Gong, N.; Yang, W.; Li, M.; Wang, X.; Yang, C., Enhanced thermal properties of polyamide 6, 6 composite/aluminum hybrid via injection joining strategy. *International Communications in Heat and Mass Transfer* **2020,** *116*, 104696.

179. Zhao, G.; Liu, H.-Y.; Du, X.; Zhou, H.; Pan, Z.; Mai, Y.-W.; Jia, Y.-Y.; Yan, W., Flame synthesis of carbon nanotubes on glass fibre fabrics and their enhancement in electrical and thermal properties of glass fibre/epoxy composites. *Compos. B. Eng.* **2020,** *198*, 108249.

180. Lim, G.; Bok, G.; Park, S.-D.; Kim, Y., Thermally conductive hexagonal boron nitride/spherical aluminum oxide hybrid composites fabricated with epoxyorganosiloxane. *Ceram. Int.* **2022,** *48* (1), 1408-1414.

181. Zhou, Y.; Wang, L.; Zhang, H.; Bai, Y.; Niu, Y.; Wang, H., Enhanced high thermal conductivity and low permittivity of polyimide based composites by core-shell Ag@SiO2 nanoparticle fillers. *Appl. Phys. Lett.* **2012,** *101* (1), 012903.

182. 周健; 陈志健; 周仕龙; 王国军, 导热 PE-LD 复合材料的制备与性能研究. *工程塑料应用* **2014,** *42* (11), 117-121.

183. 刘立柱, 赵., 翁凌, 杨旭, 赫兢, 高导热云母胶制备工艺研究. *功能材料* **2012,** *43* (03), 331-333.

184. Kim, S. H.; Bazin, N.; Shaw, J. I.; Yoo, J.-H.; Worsley, M. A.; Satcher, J. H.; Sain, J. D.; Kuntz, J. D.; Kucheyev, S. O.; Baumann, T. F.; Hamza, A. V., Synthesis of Nanostructured/Macroscopic Low-Density Copper Foams Based on Metal-Coated Polymer Core–Shell Particles. *ACS Applied Materials & Interfaces* **2016,** *8* (50), 34706-34714.

185. Lee, S. H.; Yu, S.; Shahzad, F.; Hong, J.; Noh, S. J.; Kim, W. N.; Hong, S. M.; Koo, C. M., Low percolation 3D Cu and Ag shell network composites for EMI shielding and thermal conduction. *Compos. Sci. Technol.* **2019,** *182*, 107778.

186. Huang, J.; Yang, W.; Zhu, J.; Fu, L.; Li, D.; Zhou, L., Silver nanoparticles decorated 3D reduced graphene oxides as hybrid filler for enhancing thermal conductivity of

polystyrene composites. *Composites Part A: Applied Science and Manufacturing* **2019,** *123*, 79-85.

187. Liu, B.; Li, Y.; Fei, T.; Han, S.; Xia, C.; Shan, Z.; Jiang, J., Highly thermally conductive polystyrene/polypropylene/boron nitride composites with 3D segregated structure prepared by solution-mixing and hot-pressing method. *Chem. Eng. J.* **2020,** *385*, 123829.

188. Shao, G.; Hanaor, D. A. H.; Shen, X.; Gurlo, A., Freeze Casting: From Low-Dimensional Building Blocks to Aligned Porous Structures—A Review of Novel Materials, Methods, and Applications. *Adv. Mater.* **2020,** *32* (17), 1907176.

189. Chau, M.; Kopera, B. A. F.; Machado, V. R.; Tehrani, S. M.; Winnik, M. A.; Kumacheva, E.; Retsch, M., Reversible transition between isotropic and anisotropic thermal transport in elastic polyurethane foams. *Materials Horizons* **2017,** *4* (2), 236-241.

190. Hou, X.; Chen, Y.; Dai, W.; Wang, Z.; Li, H.; Lin, C.; Nishimura, K.; Jiang, N.; Yu, J., Highly thermal conductive polymer composites via constructing micro-phragmites communis structured carbon fibers. *Chem. Eng. J.* **2019,** *375*, 121921.

191. Ma, J.; Shang, T.; Ren, L.; Yao, Y.; Zhang, T.; Xie, J.; Zhang, B.; Zeng, X.; Sun, R.; Xu, J.-B.; Wong, C.-P., Through-plane assembly of carbon fibers into 3D skeleton achieving enhanced thermal conductivity of a thermal interface material. *Chem. Eng. J.* **2020,** *380*, 122550.

192. Tong, Z.; Zhang, B.; Yu, H.; Yan, X.; Xu, H.; Li, X.; Ji, H., Si3N4 Nanofibrous Aerogel with In Situ Growth of SiOx Coating and Nanowires for Oil/Water Separation and Thermal Insulation. *ACS Applied Materials & Interfaces* **2021,** *13* (19), 22765-22773.

193. Shen, Z.; Feng, J., Achieving vertically aligned SiC microwires networks in a uniform cold environment for polymer composites with high through-plane thermal conductivity enhancement. *Compos. Sci. Technol.* **2019,** *170*, 135-140.

194. Liu, T.; Zhang, R.; Chen, M.; Liu, Y.; Xie, Z.; Tang, S.; Yuan, Y.; Wang, N., Vertically Aligned Polyamidoxime/Graphene Oxide Hybrid Sheets' Membrane for Ultrafast and

Selective Extraction of Uranium from Seawater. *Adv. Funct. Mater.* **2021,** *n/a* (n/a), 2111049.

195. Wei, Z.; Xie, W.; Ge, B.; Zhang, Z.; Yang, W.; Xia, H.; Wang, B.; Jin, H.; Gao, N.; Shi, Z., Enhanced thermal conductivity of epoxy composites by constructing aluminum nitride honeycomb reinforcements. *Compos. Sci. Technol.* **2020,** *199*, 108304.

196. Bai, H.; Chen, Y.; Delattre, B.; Tomsia Antoni, P.; Ritchie Robert, O., Bioinspired large-scale aligned porous materials assembled with dual temperature gradients. *Science Advances 1* (11), e1500849.

197. Yang, J.; Chan, K.-Y.; Venkatesan, H.; Kim, E.; Adegun, M. H.; Lee, J.-H.; Shen, X.; Kim, J. K., Superinsulating BNNS/PVA Composite Aerogels with High Solar Reflectance for Energy-Efficient Buildings. *Nano-Micro Letters* **2022,** *14* (1), 54.

198. Yang, J.; Yang, W.; Chen, W.; Tao, X., An elegant coupling: Freeze-casting and versatile polymer composites. *Prog. Polym. Sci.* **2020,** *109*, 101289.

199. Tang, L.-S.; Zhou, Y.-C.; Zhou, L.; Yang, J.; Bai, L.; Bao, R.-Y.; Liu, Z.-Y.; Yang, M.-B.; Yang, W., Double-layered and shape-stabilized phase change materials with enhanced thermal conduction and reversible thermochromism for solar thermoelectric power generation. *Chem. Eng. J.* **2022,** *430*, 132773.

200. Wang, C.; Chen, X.; Wang, B.; Huang, M.; Wang, B.; Jiang, Y.; Ruoff, R. S., Freeze-Casting Produces a Graphene Oxide Aerogel with a Radial and Centrosymmetric Structure. *ACS Nano* **2018,** *12* (6), 5816-5825.

201. Han, J.; Du, G.; Gao, W.; Bai, H., An Anisotropically High Thermal Conductive Boron Nitride/Epoxy Composite Based on Nacre-Mimetic 3D Network. *Adv. Funct. Mater.* **2019,** *29* (13), 1900412.

202. Zhao, N.; Yang, M.; Zhao, Q.; Gao, W.; Xie, T.; Bai, H., Superstretchable Nacre-Mimetic Graphene/Poly(vinyl alcohol) Composite Film Based on Interfacial Architectural Engineering. *ACS Nano* **2017,** *11* (5), 4777-4784.

203. Kong, X.; Li, L.; Li, M.; Xia, J.; Wang, Y.; Wei, X.; Xiong, S.; Gong, P.; Pan, Z.; Wu, X.; Cai, T.; Nishimura, K.; Lin, C.-T.; Jiang, N.; Yu, J., Two-Dimensional Hexagonal

Boron Nitride Nanosheets as Lateral Heat Spreader With High Thermal Conductivity. *Frontiers in Materials* **2022,** *8*.

204. Kim, Y.; Kim, J., 3D Interconnected Boron Nitride Networks in Epoxy Composites via Coalescence Behavior of SAC305 Solder Alloy as a Bridging Material for Enhanced Thermal Conductivity. *Polymers* **2020,** *12* (9).

205. An, L.; Gu, R.; Zhong, B.; Wang, J.; Zhang, J.; Yu, Y., Quasi-Isotropically Thermal Conductive, Highly Transparent, Insulating and Super-Flexible Polymer Films Achieved by Cross Linked 2D Hexagonal Boron Nitride Nanosheets. *Small* **2021,** *17* (46), 2101409.

206. Zhang, R.-C.; Huang, Z.; Huang, Z.; Zhong, M.; Zang, D.; Lu, A.; Lin, Y.; Millar, B.; Garet, G.; Turner, J.; Menary, G.; Ji, D.; Song, L.; Zhang, Q.; Zhang, J.; Sun, D., Uniaxially stretched polyethylene/boron nitride nanocomposite films with metal-like thermal conductivity. *Compos. Sci. Technol.* **2020,** *196*, 108154.

207. Ōtani, S., On the carbon fiber from the molten pyrolysis products. *Carbon* **1965,** *3* (1), 31-38.

208. Brooks, J. D.; Taylor, G. H., The formation of graphitizing carbons from the liquid phase. *Carbon* **1965,** *3* (2), 185-193.

209. Gallego, N. C.; Edie, D. D., Structure–property relationships for high thermal conductivity carbon fibers. *Composites Part A: Applied Science and Manufacturing* **2001,** *32* (8), 1031-1038.

210. Ōtani, S., Mechanism of the carbonization of MP carbon fiber at the low temperature range. *Carbon* **1967,** *5* (3), 219-225.

211. Ōtani, S.; Yamada, K.; Koitabashi, T.; Yokoyama, A., On the raw materials of MP carbon fiber. *Carbon* **1966,** *4* (3), 425-432.

212. Otani, S.; Yokoyama, A., Characteristic Chemical Constitution of Pitch Materials Suitable for the MP Carbon Fiber. *Bull. Chem. Soc. Jpn.* **1969,** *42* (5), 1417-1424.

213. Mochida, I.; Inaba, T.; Korai, Y.; Takeshita, K., Carbonization properties of carbonaceous substances oxidized by air blowing—II: Acid-catalyzed modification of

oxidized residual oil for better anisotropic development. *Carbon* **1983,** *21* (6), 553-558.

214. Mochida, I.; Inaba, T.; Korai, Y.; Fujitsu, H.; Takeshita, K., Carbonization properties of carbonaceous substances oxidized by air blowing—I: Carbonization behaviors and chemical structure of residual oils oxidized by air blowing. *Carbon* **1983,** *21* (6), 543-552.

215. Minus, M.; Kumar, S., The processing, properties, and structure of carbon fibers. *JOM* **2005,** *57* (2), 52-58.

216. Bright, A. A.; Singer, L. S., The electronic and structural characteristics of carbon fibers from mesophase pitch. *Carbon* **1979,** *17* (1), 59-69.

217. 周溪华, 沥青基碳纤维的研制与开发. *合成纤维工业* **1993,** *16* (02), 36-42.

218. Chand, S., Review Carbon fibers for composites. *Journal of Materials Science* **2000,** *35* (6), 1303-1313.

219. Frank, E.; Hermanutz, F.; Buchmeiser, M. R., Carbon Fibers: Precursors, Manufacturing, and Properties. *Macromolecular Materials and Engineering* **2012,** *297* (6), 493-501.

220. Pilling, M. W.; Yates, B.; Black, M. A.; Tattersall, P., The thermal conductivity of carbon fibre-reinforced composites. *Journal of Materials Science* **1979,** *14* (6), 1326-1338.

221. Nysten, B.; Piraux, L.; Issi, J. P., Thermal conductivity of pitch-derived fibres. *J. Phys. D: Appl. Phys.* **1985,** *18* (7), 1307-1310.

222. Kiuchi, N.; Ozawa, K.; Komami, T.; Katoh, O.; Arai, Y.; Watanabe, T.; Iwai, S., Pitch-based carbon fiber with high thermal conductivity for new advanced thermal design. In *MATERIALS-THE STAR AT CENTER STAGE*, 1998; Vol. 30, pp 68-77.

223. Gallego, N. C., *Transport properties of ribbon-shaped carbon fibers: property-structure relationship*. Clemson University: 2000.

224. 宋怀河, 马. A. 宁. A., 高导热炭纤维的研究进展. *北京化工大学学报(自然科学版)* **2014,** *41* (01), 1-13.

225. 王婷婷, 顾., 王绍凯, 李敏, 方泽农, 张佐光, 碳纤维轴向导热性能表征及其影响因素.

北京航空航天大学学报 **2017,** *43* (09), 1931-1938.

226. Qiu, L.; Zou, H.; Zhu, N.; Feng, Y.; Zhang, X.; Zhang, X., Iodine nanoparticle-enhancing electrical and thermal transport for carbon nanotube fibers. *Appl. Therm. Eng.* **2018,** *141*, 913-920.

227. Liu, J.; Qu, W.; Xie, Y.; Zhu, B.; Wang, T.; Bai, X.; Wang, X., Thermal conductivity and annealing effect on structure of lignin-based microscale carbon fibers. *Carbon* **2017,** *121*, 35-47.

228. 寇爱静. 电流诱导的热退火效应对碳材料导热性能影响的实验研究. 硕士, 青岛理工大学, 2019.

229. Mayhew, E.; Prakash, V., Thermal conductivity of individual carbon nanofibers. *Carbon* **2013,** *62*, 493-500.

230. Xu, Z.; Chen, Y.; Li, W.; Li, J.; Yu, H.; Liu, L.; Wu, G.; Yang, T.; Luo, L., Preparation of boron nitride nanosheet-coated carbon fibres and their enhanced antioxidant and microwave-absorbing properties. *RSC Advances* **2018,** *8* (32), 17944-17949.

231. Bi, D.; Sverbil, P. P.; Voinov, Y. P.; Wu, M., Raman Scattering Enhancement Based on High-Pressure High-Temperature Diamonds†. *Journal of Russian Laser Research* **2021,** *42* (6), 671-676.

232. Mavridou, K.; Arvanitidis, J.; Pavlidou, E.; Ves, S.; Katsikini, M., Raman spectroscopy as an evaluation tool of the wear of graphite lubricants in brake pads. *Lubr. Sci.* **2021,** *33* (5), 279-289.

233. Malard, L. M.; Pimenta, M. A.; Dresselhaus, G.; Dresselhaus, M. S., Raman spectroscopy in graphene. *Phys. Rep.* **2009,** *473* (5), 51-87.

234. Agari, Y.; Ueda, A.; Nagai, S., Thermal conductivity of a polyethylene filled with disoriented short‐cut carbon fibers. *J. Appl. Polym. Sci.* **1991,** *43* (6), 1117-1124.

235. Chen, J.; Wang, K.; Zhao, Y., Enhanced interfacial interactions of carbon fiber reinforced PEEK composites by regulating PEI and graphene oxide complex sizing at the interface. *Compos. Sci. Technol.* **2018,** *154*, 175-186.

236. Dong, S.; Gauvin, R., Application of dynamic mechanical analysis for the study of

the interfacial region in carbon fiber/epoxy composite materials. *Polym. Compos.* **1993,** *14* (5), 414-420.

237. Ziegel, K. D., Role of the interface in mechanical energy dissipation of composites. *J. Colloid Interface Sci.* **1969,** *29* (1), 72-80.

238. Ziegel, K.; Romanov, A., Modulus reinforcement in elastomer composites. I. Inorganic fillers. *J. Appl. Polym. Sci.* **1973,** *17* (4), 1119-1131.

239. Xia, C.; Garcia, A. C.; Shi, S. Q.; Qiu, Y.; Warner, N.; Wu, Y.; Cai, L.; Rizvi, H. R.; D? Souza, N. A.; Nie, X., Hybrid boron nitride-natural fiber composites for enhanced thermal conductivity. *Scientific reports* **2016,** *6*, 34726.

240. Wang, Z.; Liu, J.; Cheng, Y.; Chen, S.; Yang, M.; Huang, J.; Wang, H.; Wu, G.; Wu, H., Alignment of boron nitride nanofibers in epoxy composite films for thermal conductivity and dielectric breakdown strength improvement. *Nanomaterials* **2018,** *8* (4), 242.

241. Kusunose, T.; Yagi, T.; Firoz, S. H.; Sekino, T., Fabrication of epoxy/silicon nitride nanowire composites and evaluation of their thermal conductivity. *J. Mater. Chem.A* **2013,** *1* (10), 3440-3445.

242. Kim, S. H.; Heo, Y.-J.; Park, M.; Min, B.-G.; Rhee, K. Y.; Park, S.-J., Effect of hydrophilic graphite flake on thermal conductivity and fracture toughness of basalt fibers/epoxy composites. *Compos. B. Eng.* **2018,** *153*, 9-16.

243. Yuan, L.; Ma, B.; Zhu, Q.; Zhang, X.; Zhang, H.; Yu, J., Preparation and properties of mullite-bonded porous fibrous mullite ceramics by an epoxy resin gel-casting process. *Ceram. Int.* **2017,** *43* (7), 5478-5483.

244. Rajadurai, A., Thermo-mechanical characterization of siliconized E-glass fiber/hematite particles reinforced epoxy resin hybrid composite. *Appl. Surf. Sci.* **2016,** *384*, 99-106.

245. Zheng, L.-F.; Wang, L.-N.; Wang, Z.-Z.; Wang, L., Effects of γ-Ray Irradiation on the Fatigue Strength, Thermal Conductivities and Thermal Stabilities of the Glass Fibres/Epoxy Resins Composites. *Acta Metallurgica Sinica (English Letters)* **2018,** *31*

(1), 105-112.

246. Choi, J. H.; Song, H. J.; Jung, J.; Yu, J. W.; You, N. H.; Goh, M., Effect of crosslink density on thermal conductivity of epoxy/carbon nanotube nanocomposites. *J. Appl. Polym. Sci.* **2017,** *134* (4).

247. Chen, J.; Yan, L.; Song, W.; Xu, D., Thermal and electrical properties of carbon nanotube-based epoxy composite materials. *Materials Research Express* **2018,** *5* (6), 065051.

248. Liu, Z.; Li, H.; Gu, J.; Wang, D.; Qu, C., Performances of an epoxy-amine network after introducing the MWCNTs: rheology, thermal and electrical conductivity, mechanical properties. *J. Adhes. Sci. Technol.* **2019,** *33* (4), 382-394.

249. Brown, M.; Jagannadham, K., Thermal Conductivity of MWNT-Epoxy Composites by Transient Thermoreflectance. *J. Electron. Mater.* **2015,** *44* (8), 2624-2630.

250. Hong, W.-T.; Tai, N.-H., Investigations on the thermal conductivity of composites reinforced with carbon nanotubes. *Diamond Relat. Mater.* **2008,** *17* (7-10), 1577-1581.

251. Liao, G.; You, Q.; Xia, H.; Wang, D., Preparation and properties of novel epoxy composites containing electrospun PA6/F-MWNTs fibers. *Polymer Engineering & Science* **2016,** *56* (11), 1259-1266.

252. Huang, H.; Liu, C.; Wu, Y.; Fan, S., Aligned carbon nanotube composite films for thermal management. *Adv. Mater.* **2005,** *17* (13), 1652-1656.

253. Uetani, K.; Ata, S.; Tomonoh, S.; Yamada, T.; Yumura, M.; Hata, K., Elastomeric Thermal Interface Materials with High Through-Plane Thermal Conductivity from Carbon Fiber Fillers Vertically Aligned by Electrostatic Flocking. *Adv. Mater.* **2014,** *26* (33), 5857-5862.

254. Ren, L.; Zhou, X.; Xue, J.; Song, Z.; Li, B.; Liu, Q.; Zhao, C., Thermal Metamaterials with Site-Specific Thermal Properties Fabricated by 3D Magnetic Printing. *Adv. Mater. Technol.* **2019**, 1900296.

255. Fang, Z.; Li, M.; Wang, S.; Gu, Y.; Li, Y.; Zhang, Z., Through-thickness thermal conductivity enhancement of carbon fiber composite laminate by filler network. *Int. J.*

Heat Mass Transfer **2019,** *137*, 1103-1111.

256. Noh, Y. J.; Kim, S. Y., Synergistic improvement of thermal conductivity in polymer composites filled with pitch based carbon fiber and graphene nanoplatelets. *Polym. Test.* **2015,** *45*, 132-138.

257. Wei, J.; Liao, M.; Ma, A.; Chen, Y.; Duan, Z.; Hou, X.; Li, M.; Jiang, N.; Yu, J., Enhanced thermal conductivity of polydimethylsiloxane composites with carbon fiber. *Compos. Commun.* **2020,** *17*, 141-146.

258. Xu, J.; Munari, A.; Dalton, E.; Mathewson, A.; Razeeb, K. M., Silver nanowire array-polymer composite as thermal interface material. *J. Appl. Phys.* **2009,** *106* (12), 124310.

259. Li, Z.; Zhang, L.; Qi, R.; Xie, F.; Qi, S., Improvement of the thermal transport performance of a poly (vinylidene fluoride) composite film including silver nanowire. *Journal of Applied Polymer Science* **2016,** *133* (25).

260. Balachander, N.; Seshadri, I.; Mehta, R. J.; Schadler, L. S.; Borca-Tasciuc, T.; Keblinski, P.; Ramanath, G., Nanowire-filled polymer composites with ultrahigh thermal conductivity. *Appl. Phys. Lett.* **2013,** *102* (9), 093117.

261. Seshadri, I.; Esquenazi, G. L.; Borca-Tasciuc, T.; Keblinski, P.; Ramanath, G., Multifold Increases in thermal conductivity of polymer nanocomposites through microwave welding of metal nanowire fillers. *Adv. Mater. Interfaces* **2015,** *2* (15), 1500186.

262. Wang, S.; Cheng, Y.; Wang, R.; Sun, J.; Gao, L., Highly thermal conductive copper nanowire composites with ultralow loading: toward applications as thermal interface materials. *ACS applied materials & interfaces* **2014,** *6* (9), 6481-6486.

263. Jang, I.; Shin, K.-H.; Yang, I.; Kim, H.; Kim, J.; Kim, W.-H.; Jeon, S.-W.; Kim, J.-P., Enhancement of thermal conductivity of BN/epoxy composite through surface modification with silane coupling agents. *Colloids and Surfaces A: Physicochemical and Engineering Aspects* **2017,** *518*, 64-72.

264. Kim, K.; Ju, H.; Kim, J., Surface modification of BN/Fe3O4 hybrid particle to enhance interfacial affinity for high thermal conductive material. *Polymer* **2016,** *91*, 74-

80.

265. Cui, S.; Wu, W.; Liu, C.; Wang, Y.; Chen, Q.; Liu, X., Modification of the three-dimensional graphene aerogel self-assembled network using a titanate coupling agent and its thermal conductivity mechanism with epoxy composites. *Nanoscale* **2021,** *13* (43), 18247-18255.

266. Tanaka, K.; Ogata, S.; Kobayashi, R.; Tamura, T.; Kitsunezuka, M.; Shinma, A., Enhanced heat transfer through filler-polymer interface by surface-coupling agent in heat-dissipation material: A non-equilibrium molecular dynamics study. *J. Appl. Phys.* **2013,** *114* (19), 193512.

267. Li, K.; Liu, Q.; Cheng, H.; Hu, M.; Zhang, S., Classification and carbon structural transformation from anthracite to natural coaly graphite by XRD, Raman spectroscopy, and HRTEM. *Spectrochimica Acta Part A: Molecular and Biomolecular Spectroscopy* **2021,** *249*, 119286.

268. Li, K.; Rimmer, S. M.; Liu, Q., Geochemical and petrographic analysis of graphitized coals from Central Hunan, China. *International Journal of Coal Geology* **2018,** *195*, 267-279.

269. Hopkins, P. E.; Phinney, L. M.; Serrano, J. R.; Beechem, T. E., Effects of surface roughness and oxide layer on the thermal boundary conductance at aluminum/silicon interfaces. *Physical Review B* **2010,** *82* (8), 085307.

270. Chiu, C.-P.; Maveety, J. G.; Tran, Q. A., Characterization of solder interfaces using laser flash metrology. *Microelectronics Reliability* **2002,** *42* (1), 93-100.

271. Zhang, C.; Shi, Z.; Li, A.; Zhang, Y. F., RGO-Coated Polyurethane Foam/Segmented Polyurethane Composites as Solid–Solid Phase Change Thermal Interface Material. *Polymers* **2020,** *12* (12), 3004.

272. Cho, D.; Choi, Y.; Park, J. K.; Lee, J.; Yoon, B. I.; Lim, Y. S., Thermal conductivity and thermal expansion behavior of pseudo-unidirectional and 2-directional quasi-carbon fiber/phenolic composites. *Fibers and Polymers* **2004,** *5* (1), 31-38.

273. Ali, Z.; Kong, X.; Li, M.; Hou, X.; Li, L.; Qin, Y.; Song, G.; Wei, X.; Zhao, S.; Cai, T.;

Dai, W.; Lin, C.-T.; Jiang, N.; Yu, J., Ultrahigh Thermal Conductivity of Epoxy Composites with Hybrid Carbon Fiber and Graphene Filler. *Fibers and Polymers* **2021**, 1-8.

274. Li, M.; Ali, Z.; Wei, X.; Li, L.; Song, G.; Hou, X.; Do, H.; Greer, J. C.; Pan, Z.; Lin, C.-T.; Jiang, N.; Yu, J., Stress induced carbon fiber orientation for enhanced thermal conductivity of epoxy composites. *Compos. B. Eng.* **2021,** *208*, 108599.

275. Li, M.; Li, L.; Hou, X.; Qin, Y.; Song, G.; Wei, X.; Kong, X.; Zhang, Z.; Do, H.; Greer, J. C.; Han, F.; Cai, T.; Dai, W.; Lin, C.-T.; Jiang, N.; Yu, J., Synergistic effect of carbon fiber and graphite on reducing thermal resistance of thermal interface materials. *Compos. Sci. Technol.* **2021,** *212*, 108883.

276. Fukai, J.; Kanou, M.; Kodama, Y.; Miyatake, O., Thermal conductivity enhancement of energy storage media using carbon fibers. *Energy Convers. Manage.* **2000,** *41* (14), 1543-1556.

277. Liu, T.; Li, J.; Wang, X.; Deng, Z.; Yu, X.; Lu, A.; Yu, F.; He, J., Preparation and properties of thermal conductive polyamide 66 composites. *J. Thermoplast. Compos. Mater.* **2013,** *28* (1), 32-45.

278. Krause, B.; Rzeczkowski, P.; Pötschke, P., Thermal Conductivity and Electrical Resistivity of Melt-Mixed Polypropylene Composites Containing Mixtures of Carbon-Based Fillers. *Polymers* **2019,** *11* (6), 1073.

279. Bard, S.; Schönl, F.; Demleitner, M.; Altstädt, V., Influence of Fiber Volume Content on Thermal Conductivity in Transverse and Fiber Direction of Carbon Fiber-Reinforced Epoxy Laminates. *Materials* **2019,** *12* (7), 1084.

280. Gharagozloo-Hubmann, K.; Boden, A.; Czempiel, G. J. F.; Firkowska, I.; Reich, S., Filler geometry and interface resistance of carbon nanofibres: Key parameters in thermally conductive polymer composites. *Appl. Phys. Lett.* **2013,** *102* (21), 213103.

281. Huang, X.; Iizuka, T.; Jiang, P.; Ohki, Y.; Tanaka, T., Role of Interface on the Thermal Conductivity of Highly Filled Dielectric Epoxy/AlN Composites. *J PHYS CHEM C* **2012,** *116* (25), 13629-13639.

282. Yu, A.; Ramesh, P.; Sun, X.; Bekyarova, E.; Itkis, M. E.; Haddon, R. C., Enhanced Thermal Conductivity in a Hybrid Graphite Nanoplatelet – Carbon Nanotube Filler for Epoxy Composites. *Adv. Mater.* **2008,** *20* (24), 4740-4744.

283. Gadiou, R.; Didion, A.; Saadallah, S.-E.; Couzi, M.; Rouzaud, J.-N.; Delhaes, P.; Vix-Guterl, C., Graphitization of carbons synthesized in a confined geometry. *Carbon* **2006,** *44* (15), 3348-3352.

284. Jin, X.; He, R.; Dai, S., Electrochemical Graphitization: An Efficient Conversion of Amorphous Carbons to Nanostructured Graphites. *Chemistry – A European Journal* **2017,** *23* (48), 11455-11459.

285. Xiao, P.; Li, D.; Gong, Y.; Zhang, S.; Mo, G.; Li, Z., Simple carbon fiber graphitization device for in-situ measurement of small angle X-ray scattering (SAXS). *Instrumentation Science & Technology* **2021,** *49* (1), 21-31.

286. Zhao, J. G.; Li, F. Y.; Jin, C. Q., Graphitization of activated carbon under high pressures and high temperatures. *Solid State Commun.* **2009,** *149* (19), 818-821.

287. Walker, I. R., *Reliability in Scientific Research: Improving the Dependability of Measurements, Calculations, Equipment, and Software*. Cambridge University Press: 2011.

288. Subramaniam, C.; Yasuda, Y.; Takeya, S.; Ata, S.; Nishizawa, A.; Futaba, D.; Yamada, T.; Hata, K., Carbon nanotube-copper exhibiting metal-like thermal conductivity and silicon-like thermal expansion for efficient cooling of electronics. *Nanoscale* **2014,** *6* (5), 2669-2674.

289. Abdalla, M.; Dean, D.; Theodore, M.; Fielding, J.; Nyairo, E.; Price, G., Magnetically processed carbon nanotube/epoxy nanocomposites: Morphology, thermal, and mechanical properties. *Polymer* **2010,** *51* (7), 1614-1620.

290. Ma, Z. H.; Huang, J. L.; Gu, Y. J.; Jin, B.; Chen, G. Y., Thermal Conductivity and Thermal Expansion Properties of AlN/EP Composite. *Advanced Materials Research* **2012,** *482-484*, 1410-1413.

291. Shimazaki, Y.; Miyazaki, Y.; Takezawa, Y.; Nogi, M.; Abe, K.; Ifuku, S.; Yano, H.,

Excellent Thermal Conductivity of Transparent Cellulose Nanofiber/Epoxy Resin Nanocomposites. *Biomacromolecules* **2007,** *8* (9), 2976-2978.

292. Yung, K. C.; Zhu, B. L.; Yue, T. M.; Xie, C. S., Preparation and properties of hollow glass microsphere-filled epoxy-matrix composites. *Compos. Sci. Technol.* **2009,** *69* (2), 260-264.

293. Wong, C. P.; Bollampally, R. S., Thermal conductivity, elastic modulus, and coefficient of thermal expansion of polymer composites filled with ceramic particles for electronic packaging. *J. Appl. Polym. Sci.* **1999,** *74* (14), 3396-3403.

294. Lee, G.-W.; Park, M.; Kim, J.; Lee, J. I.; Yoon, H. G., Enhanced thermal conductivity of polymer composites filled with hybrid filler. *Composites Part A: Applied Science and Manufacturing* **2006,** *37* (5), 727-734.

295. Anjana, P. S.; Uma, S.; Philip, J.; Sebastian, M. T., Thermal properties of low loss PTFE-CeO2 dielectric ceramic composites for microwave substrate applications. *J. Appl. Polym. Sci.* **2010,** *118* (2), 751-758.

296. Joven, R.; Minaie, B., Thermal properties of autoclave and out-of-autoclave carbon fiber-epoxy composites with different fiber weave configurations. *J. Compos. Mater.* **2018,** *52* (29), 4075-4085.

297. Chen, J.; Xiong, X.; Xiao, P.; Zhang, H.-B., The catalytic effect of boric acid on polyacrylonitrile-based carbon fibers and the thermal conductivity of carbon/carbon composites produced from them. *Carbon* **2010,** *48* (8), 2341-2346.

298. Wang, X.; Lu, C.; Rao, W., Liquid metal-based thermal interface materials with a high thermal conductivity for electronic cooling and bioheat-transfer applications. *Appl. Therm. Eng.* **2021,** *192*, 116937.

299. Yan, Q.; Liu, C.; Zhang, J., Experimental study on thermal conductivity of composite phase change material of fatty acid and paraffin. *Materials Research Express* **2019,** *6* (6), 065507.

300. Choi, J.; Dun, C.; Forsythe, C.; Gordon, M. P.; Urban, J. J., Lightweight wearable thermoelectric cooler with rationally designed flexible heatsink consisting of phase-

change material/graphite/silicone elastomer. *J. Mater. Chem.A* **2021,** *9* (28), 15696-15703.

301. Huang, J.; Wu, B.; Lyu, S.; Li, T.; Han, H.; Li, D.; Wang, J.-K.; Zhang, J.; Lu, X.; Sun, D., Improving the thermal energy storage capability of diatom-based biomass/polyethylene glycol composites phase change materials by artificial culture methods. *Sol. Energy Mater. Sol. Cells* **2021,** *219*, 110797.

302. Liu, Q.; Jiang, L.; Zhao, Y.; Wang, Y.; Lei, J., Preparation and characterization of a novel form-stable phase change material for thermal energy storage. *J. Therm. Anal. Calorim.* **2021,** *143* (4), 2945-2952.

303. Wu, B.; Lyu, S.; Han, H.; Li, T.; Sun, H.; Wang, J.-K.; Li, D.; Lei, F.; Huang, J.; Sun, D., Biomass-based shape-stabilized phase change materials from artificially cultured ship-shaped diatom frustules with high enthalpy for thermal energy storage. *Compos. B. Eng.* **2021,** *205*, 108500.

304. Yang, J.; Tang, L.-S.; Bai, L.; Bao, R.-Y.; Liu, Z.-Y.; Xie, B.-H.; Yang, M.-B.; Yang, W., High-performance composite phase change materials for energy conversion based on macroscopically three-dimensional structural materials. *Materials Horizons* **2019,** *6* (2), 250-273.

305. Yang, J.; Li, X.; Han, S.; Zhang, Y.; Min, P.; Koratkar, N.; Yu, Z.-Z., Air-dried, high-density graphene hybrid aerogels for phase change composites with exceptional thermal conductivity and shape stability. *J. Mater. Chem.A* **2016,** *4* (46), 18067-18074.

306. Ye, S.; Zhang, Q.; Hu, D.; Feng, J., Core–shell-like structured graphene aerogel encapsulating paraffin: shape-stable phase change material for thermal energy storage. *J. Mater. Chem.A* **2015,** *3* (7), 4018-4025.

307. Xi, S.; Wang, M.; Wang, L.; Xie, H.; Yu, W., 3D reduced graphene oxide aerogel supported TiO2-x for shape-stable phase change composites with high photothermal efficiency and thermal conductivity. *Sol. Energy Mater. Sol. Cells* **2021,** *226*, 111068.

308. Li, H.; Meng, N.; Lyu, W.; Cheng, Z.; Chen, S.; Zhang, W.; Liao, Y., Solvothermal synthesis of porphyrin-ferrocenyl conjugated microporous polymer nanospheres for

shape-stable phase change materials with improved latent heat and cyclability. *J. Colloid Interface Sci.* **2021,** *595*, 178-186.

309. Tumirah, K.; Hussein, M.; Zulkarnain, Z.; Rafeadah, R., Nano-encapsulated organic phase change material based on copolymer nanocomposites for thermal energy storage. *Energy* **2014,** *66*, 881-890.

310. Umair, M. M.; Zhang, Y.; Iqbal, K.; Zhang, S.; Tang, B., Novel strategies and supporting materials applied to shape-stabilize organic phase change materials for thermal energy storage–A review. *Applied Energy* **2019,** *235*, 846-873.

311. Gao, H.; Wang, J.; Chen, X.; Wang, G.; Huang, X.; Li, A.; Dong, W., Nanoconfinement effects on thermal properties of nanoporous shape-stabilized composite PCMs: A review. *Nano Energy* **2018,** *53*, 769-797.

312. Sun, K.; Kou, Y.; Dong, H.; Ye, S.; Zhao, D.; Liu, J.; Shi, Q., The design of phase change materials with carbon aerogel composites for multi-responsive thermal energy capture and storage. *J. Mater. Chem.A* **2021,** *9* (2), 1213-1220.

313. Sarkar, S. D.; Uddin, M. M.; Roy, C. K.; Hossen, M. J.; Sujan, M. I.; Azam, M. S., Mechanically tough and highly stretchable poly(acrylic acid) hydrogel cross-linked by 2D graphene oxide. *RSC Advances* **2020,** *10* (18), 10949-10958.

314. Johnson, E. R.; Keinan, S.; Mori-Sánchez, P.; Contreras-García, J.; Cohen, A. J.; Yang, W., Revealing Noncovalent Interactions. *J. Am. Chem. Soc.* **2010,** *132* (18), 6498-6506.

315. Lu, T.; Chen, F., Multiwfn: A multifunctional wavefunction analyzer. *J. Comput. Chem.* **2012,** *33* (5), 580-592.

316. Frisch, M. J.; Trucks, G. W.; Schlegel, H. B.; Scuseria, G. E.; Robb, M. A.; Cheeseman, J. R.; Scalmani, G.; Barone, V.; Petersson, G. A.; Nakatsuji, H.; Li, X.; Caricato, M.; Marenich, A. V.; Bloino, J.; Janesko, B. G.; Gomperts, R.; Mennucci, B.; Hratchian, H. P.; Ortiz, J. V.; Izmaylov, A. F.; Sonnenberg, J. L.; Williams-Young, D.; Ding, F.; Lipparini, F.; Egidi, F.; Goings, J.; Peng, B.; Petrone, A.; Henderson, T.; Ranasinghe, D.; Zakrzewski, V. G.; Gao, J.; Rega, N.; Zheng, G.; Liang, W.; Hada, M.; Ehara, M.;

Toyota, K.; Fukuda, R.; Hasegawa, J.; Ishida, M.; Nakajima, T.; Honda, Y.; Kitao, O.; Nakai, H.; Vreven, T.; Throssell, K.; Montgomery Jr., J. A.; Peralta, J. E.; Ogliaro, F.; Bearpark, M. J.; Heyd, J. J.; Brothers, E. N.; Kudin, K. N.; Staroverov, V. N.; Keith, T. A.; Kobayashi, R.; Normand, J.; Raghavachari, K.; Rendell, A. P.; Burant, J. C.; Iyengar, S. S.; Tomasi, J.; Cossi, M.; Millam, J. M.; Klene, M.; Adamo, C.; Cammi, R.; Ochterski, J. W.; Martin, R. L.; Morokuma, K.; Farkas, O.; Foresman, J. B.; Fox, D. J. *Gaussian 16 Rev. A.03*, Wallingford, CT, 2016.

317. Humphrey, W.; Dalke, A.; Schulten, K., VMD: Visual molecular dynamics. *Journal of Molecular Graphics* **1996,** *14* (1), 33-38.

318. Xu, Y.; Kraemer, D.; Song, B.; Jiang, Z.; Zhou, J.; Loomis, J.; Wang, J.; Li, M.; Ghasemi, H.; Huang, X.; Li, X.; Chen, G., Nanostructured polymer films with metal-like thermal conductivity. *Nature Communications* **2019,** *10* (1), 1771.

319. Tu, J.; Li, H.; Zhang, J.; Hu, D.; Cai, Z.; Yin, X.; Dong, L.; Huang, L.; Xiong, C.; Jiang, M., Latent heat and thermal conductivity enhancements in polyethylene glycol/polyethylene glycol-grafted graphene oxide composites. *Advanced Composites and Hybrid Materials* **2019,** *2* (3), 471-480.

320. Du, X.; Qiu, J.; Deng, S.; Du, Z.; Cheng, X.; Wang, H., Ti3C2Tx@PDA-Integrated Polyurethane Phase Change Composites with Superior Solar-Thermal Conversion Efficiency and Improved Thermal Conductivity. *ACS Sustainable Chemistry & Engineering* **2020,** *8* (14), 5799-5806.

321. Ma, J.; Ma, T.; Duan, W.; Wang, W.; Cheng, J.; Zhang, J., Superhydrophobic, multi-responsive and flexible bottlebrush-network-based form-stable phase change materials for thermal energy storage and sprayable coatings. *J. Mater. Chem.A* **2020,** *8* (42), 22315-22326.

322. Shi, J.; Aftab, W.; Liang, Z.; Yuan, K.; Maqbool, M.; Jiang, H.; Xiong, F.; Qin, M.; Gao, S.; Zou, R., Tuning the flexibility and thermal storage capacity of solid–solid phase change materials towards wearable applications. *J. Mater. Chem.A* **2020,** *8* (38), 20133-20140.

323. Wei, X.; Jin, X.-z.; Zhang, N.; Qi, X.-d.; Yang, J.-h.; Zhou, Z.-w.; Wang, Y., Constructing cellulose nanocrystal/graphene nanoplatelet networks in phase change materials toward intelligent thermal management. *Carbohydr. Polym.* **2021,** *253*, 117290.